HIGH RESOLUTION IMAGING AND IMAGE ANALYSIS IN POROUS MEDIA

A THESIS SUBMITTED TO
THE GRADUATE SCHOOL OF NATURAL AND APPLIED SCIENCES
OF
MIDDLE EAST TECHNICAL UNIVERSITY

BY

ÖZGE HANDE YALÇIN

IN PARTIAL FULFILLMENT OF THE REQUIREMENTS
FOR
THE DEGREE OF MASTER OF SCIENCE
IN
CHEMICAL ENGINEERING

SEPTEMBER 2019

Approval of the thesis:

HIGH RESOLUTION IMAGING AND IMAGE ANALYSIS IN POROUS MEDIA

submitted by **ÖZGE HANDE YALÇIN** in partial fulfillment of the requirements for the degree of **Master of Science in Chemical Engineering Department, Middle East Technical University** by,

Prof. Dr. Halil Kalıpçılar
Dean, Graduate School of **Natural and Applied Sciences** _____

Prof. Dr. Pınar Çalık
Head of Department, **Chemical Engineering** _____

Assist. Prof. Dr. Harun Koku
Supervisor, **Chemical Engineering, METU** _____

... ...
Co-Supervisor, **...** _____

Examining Committee Members:

Prof. Dr. Pınar Çalık
Chemical Engineering, METU _____

Assist. Prof. Dr. Harun Koku
Chemical Engineering, METU _____

Prof. Dr. Demet Çetin
Mathematics and Science Education, Gazi University _____

Assoc. Prof. Dr. Çerağ Dilek Hacıhabiboğlu
Chemical Engineering, METU _____

Assist. Prof. Dr. İnci Ayrancı Tansık
Chemical Engineering, METU _____

Date: 02.09.2019

I hereby declare that all information in this document has been obtained and presented in accordance with academic rules and ethical conduct. I also declare that, as required by these rules and conduct, I have fully cited and referenced all material and results that are not original to this work.

Name, Surname: Özge Hande Yalçın

Signature:

ABSTRACT

HIGH RESOLUTION IMAGING AND IMAGE ANALYSIS IN POROUS MEDIA

Yalçın, Özge Hande
Master of Science, Chemical Engineering
Supervisor: Assist. Prof. Dr. Harun Koku

September 2019, 156 pages

Flow and mass transfer in porous media are intimately coupled to their microstructure. Advances in computational capabilities have brought about the possibility of modeling these materials by employing the high-resolution 3D topography in flow and mass transfer simulations. This work investigates and analyzes the microstructure and adsorbate localization behavior of porous media. Specifically, high- resolution microscopy techniques were implemented to obtain morphology information for porous media. Gigacap Q-650M and HALO^{TM} were chosen as adsorbents and α-lactalbumin was used as staining protein. Microstructures of Gigacap Q-650M and HALO^{TM} were imaged by using Scanning Electron Microscopy (SEM). The crosslinking structure of Gigacap Q-650M was observed, and the core-shell structure of HALO^{TM} particle was also investigated by using SEM. Gigacap Q-650M with and without adsorbed protein were characterized by Transmission Electron Microscopy (TEM). Contrast in the protein-loaded adsorbent was much better than the sample without adsorbed protein. In TEM images, protein localization on the adsorbent was investigated. It can be surmised that the protein on Gigacap Q-650M remains confined to polymethyl methacrylate (PMMA) base and aldehyde fixation itself results in extensive cross-linking of proteins (and presumably functional groups), thus

potentially resulting in the contiguous solid-phase observed. Characterizations of Gigacap Q-650M and HALO^{TM} were also done by using Focus Ion Beam (FIB). HALO^{TM} particle structure composed of core and the shell part was investigated and 2-D images of HALO^{TM} were used to construct 3-D topography of it by using FIB whereas FIB images of Gigacap Q-650M could not be used to form 3-D structure because of the low resolution of images.

Keywords: Imaging techniques, Ion exchange chromatography, Protein adsorption, Core-shell particles, Polymer modified stationary phase

ÖZ

GÖZENEKLİ YAPILARIN YÜKSEK ÇÖZÜNÜRLÜKLE GÖRÜNTÜLENMESİ VE GÖRÜNTÜANALİZİ

Yalçın, Özge Hande
Yüksek Lisans, Kimya Mühendisliği
Tez Danışmanı: Dr. Öğr. Üyesi Harun Koku

Eylül 2019, 156 sayfa

Gözenekli yapılardaki akışkan ve kütle transferi bu malzemelerin mikroyapıları ile derinlemesine bağlantılıdır. Bilgisayar destekli programlarının avantajları, akışkan ve kütle transfer simulasyonlarında bu malzemelerin yüksek çözünürlüklü 3D topografyalarının kullanılarak modellenmesine olanak sağlamasıdır. Bu çalışma gözenekli ortamların adsorbat yerleşim davranışlarını ve mikroyapılarını analiz eder ve inceler. Spesifik olarak porlu ortamların morfoloji bilgisini elde etmek için yüksek çözünürlüklü mikroskopik teknikler uygulanmıştır. Adsorban olarak Gigacap Q-650M ve HALO^{TM} seçilmiştir ve lekeleme proteini olarak α-lactalbumin kullanılmıştır. Gigacap Q-650M ve HALO^{TM} mikroyapıları Taramalı Electron Mikroskopu (SEM) kullanılarak görüntülenmiştir. SEM kullanılarak Gigacap Q-650M çapraz bağlı yapısı gözlemlenmiştir. HALO^{TM} parçacıklarının çekirdek-kabuk yapısı da ayrıca SEM kullanılarak incelenmiştir. Transmisyon Elektron Mikroskobu (TEM) kullanılarak yüzeyinde protein tutunan ve tutunmamış Gigacap Q-650M karakterize edilmiştir. Protein yüklenmiş adsorbanın kontrastı protein yüklenmemiş örneğe göre çok daha iyi olduğu gözlemlenmiştir. TEM görüntülerinde adsorban üzerindeki protein yerleşimi net olarak görülmüştür. Gigacap Q-650M üzerinde bulunan proteinlerin polimetil metakrilat (PMMA) bazı içerisinde hapsolmuş şekilde

bulunması ve aldehit ile sabitlenmesi proteinlerin çok fazla çapraz bağ oluşturmasını sağlar (muhtemelen fonksiyonel gruplar ile) ve bu durum bitişik katı fazın gözlemlenmesine olanak sağlar. Gigacap Q-650M and HALO^{TM} karakterizasyonları Odaklanmış İyon Işını (FIB) kullanılarak da yapılmıştır. Çekirdek ve kabuk kısımlarından oluşan HALO^{TM} parçacıkları gözlemlenmiştir ve 2 boyutlu görüntüleri elde edilmiş olup 3D topografya oluşturmak için kullanılmıştır. Ancak, Gigacap Q-650M FIB görüntüleri düşük çözünürlükte olduğu için 3D yapı elde etmek için kullanılamamıştır.

Anahtar Kelimeler: Görüntüleme teknikleri, İyon değişim kromatografisi, Protein adsorpsiyonu, Çekirdek-kabuk parçacıkları, Polimer modifiye edilmiş sabit faz,

To my Family

ACKNOWLEDGEMENTS

I have many people to thank for this work. Firstly, I gave thanks to my advisor Asst. Prof. Dr. Harun Koku. I have learned much. His knowledge and vision inspire me throughout my research. I am grateful to him for his endless patience and guide me. Without his support, I would not succeed.

It was the challenge for me to run both academic and vocational careers. Herein, I would like to thank Mr. Semavi Yorgancılar, CEO of YORGLASS, Mrs. Gülfem Yorgancılar Perçin, HR Director, and Serkan Süzgen, Plant Manager, to provide me the chance to go after my goals. I would not forget my ex-Product Development Manager, Mr. Çağrı Cint and ex-Quality Manager, Mr. Alparslan Eker. They had a great deal of trouble to motivate me and thanks for supporting me on this journey.

The most importantly, I would like to thank my parents for their supports. Always they were with me to encourage even if when I was pessimistic. From the beginning to the end my beloved husband, Tolga has been always with me. He has stood my all caprice, and thanks for never leaving my hands.

TABLE OF CONTENTS

LIST OF TABLES

TABLES

LIST OF FIGURES

FIGURES

LIST OF ABBREVIATIONS

ABBREVIATIONS

Au: Gold

CPD: Critical Point Drier

BSA: Bovine Serum Albumin

DDSA: Dodecenyl Succinic Anhydride

FIB: Focused Ion Beam

HETP: Height equivalent theoretical plate

L_c:Colum Length

N: Plate Number

NMA: Methyl-5-Norbornene-2, 3-Dicarboxylic Anhydride

OsO_4: Osmium tetroxide

PBS: Phosphate Buffer Solution

Pd: Palladium

pI: Isoelectric point

pKa: Association constant

SEM: Scanning Electron Microscopy

TEM: Transmission Electron Microscopy

U_s: Superfical velocity

Uv-Vis: Ultraviolet-Visible

ΔP: The pressure drop

μ: Mobile phase linear velocity

κ: Permeability

σ^2 : Variance

CHAPTER 1

INTRODUCTION

Recovery and purification of biosynthetic products are important to get high yield products. Compared to conventional chemical synthesis, an extremely high level of purity from complex mixtures may be desired for medical applications. Moreover, mild operation conditions are required since the targeted products are labile. The various processes to purify these products are composed of cascade unit operation processes called downstream processing. For instance, about 50-70 % of total manufacturing cost is related to the cost of downstream processing due to the complex methods employed (Ottens, Wesselingh, and van der Wielen 2006) As a result of this, innovations and optimizations of downstream processing are crucial.

There are many purification methods in downstream processing. Chromatography is one of the most common purification methods used since it has very high specificity, very good reproducibility, a wide range of options for separations and it requires mild operation conditions (Kaphingst, Persky, and Lachance 2010). In large scale purification of proteins, ion exchange chromatography is a very significant method. Chromatography typically involves an adsorbent, called the stationary phase and the mobile phase which is a solution composed of the solute mixture within a solvent. Chromatographic separations are based on selectivity which means that as the solute mixture is moved by solvent (mobile phase) through the stationary phase, each component in the solute mixture interacts with the stationary phase, and the extent of retention of each component is determined by its interaction strength. There are many interaction types between components and the stationary phase for separation such as charge, affinity, and size. These properties are used in different types of chromatography. Ion exchange chromatography is extensively used in the separation of charged molecules based on proteins, amino acids, peptides that contain positively

and negatively charged chemical groups (Weiß 2016). The separation of components can be described using a pulse injection as an illustrative case example: After injection, the sample band is separated into individual analyte bands. In Figure 1.1, at time zero, the sample is injected and begins to form a band. After a while, individual dyes are in separated bands at different speed. This is because the affinity differences, for example, the purple dye in the figure has greater speed than others since it has a lower affinity to the stationary phase. On the other hand, the red dye has a higher affinity to the stationary phase, which is why it has lower speed and is the most retained compound in the mixture.

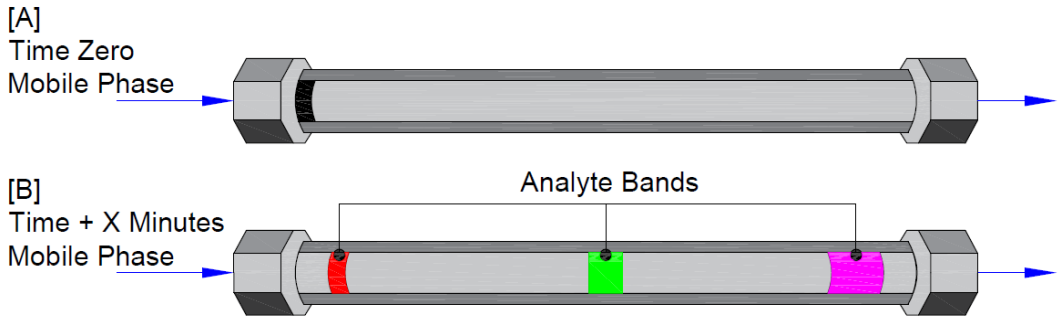

Figure 1.1. Separation of analyte using chromatography

Since each dye band moves at a different speed, it is possible to separate the mixture chromatographically. The separated band from the column goes to the appropriate detector which sends electrical signals to the computer, and the data are visualized as peaks.

The efficiency of a separation is measured by the spread or variance (σ^2) of peaks. Figure 1.2 shows the peaks of the components of a hypothetical mixture of A and B. Well separated peaks are proof of good separation. Figure 1.2.a shows an example of good separation, whereas a case where overlapping of peaks and mixing of the fractions are observed can be seen in Figure 1.2.b.

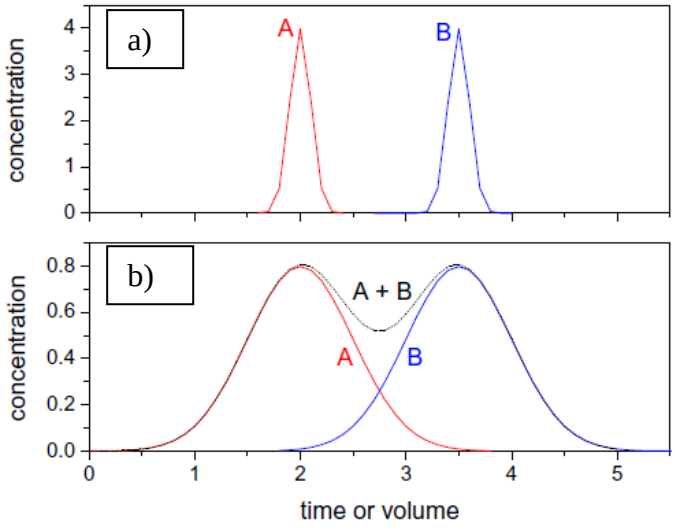

Figure 1.2. Separation of two components which are A and B. Successful resolution (a) and peak overlapping (b)(Koku 2011)

As efficiency of separation increases, variance will decrease, and in ideal chromatography it is zero. However, in real separation systems variance depends on the kinetics of flow and mass transfer phenomena namely axial diffusion, velocity profile effects, diffusion from bulk to film, diffusion through the film, diffusion through pores and surface diffusion. Regarding mass transfer, several factors increase band broadening. The first step of the separation process is molecular transport to the boundary layer of the particle by convection or diffusion (Seidel-Morgenstern, Schulte, and Epping 2013). The second step is diffusive transport of solute through the film layer called film diffusion. The third step is the transport of solute molecules toward the adsorption centers inside the pore system of the adsorbent particles (Seidel-Morgenstern, Schulte, and Epping 2013). If mass transport takes place by surface diffusion, a solute molecule is adsorbed and transported deeper into the pore system by movement along the pore surface. Pore diffusion is driven by restricted Fickian diffusion of the solute molecules within the free pore volume (Seidel-Morgenstern, Schulte, and Epping 2013). During the transport process, the solute molecules are outside the attraction forces of the adsorbent surface. All of these steps can be represented by a total variance. Height of an equivalent theoretical plate (HETP) is

well-recognized in chromatography and it can be used to quantify mass transfer effects and to capture deviations from ideal behavior within packed beds (Equation 1.1):

$$HETP = \frac{Lc}{N} \qquad (1.1)$$

Where;

Lc: Column length

N: Plate number

The van Deemter Curve (Figure 1.3) shows the dependence of σ^2 on system parameters like fluid velocity, particle diameter.

Each constant parameter in equation 1.2 (A, B, and C) corresponds to an aspect of band broadening (Fok and Cheah 1987). Specifically, parameter A corresponds to eddy diffusion, B to axial diffusion, and C to mass transfer inside and in the close vicinity of the adsorbent. The mobile phase linear velocity through the chromatographic system is shown as μ (Fok and Cheah 1987).

$$HETP = A + \frac{B}{\mu} + C \cdot \mu \qquad (1.2)$$

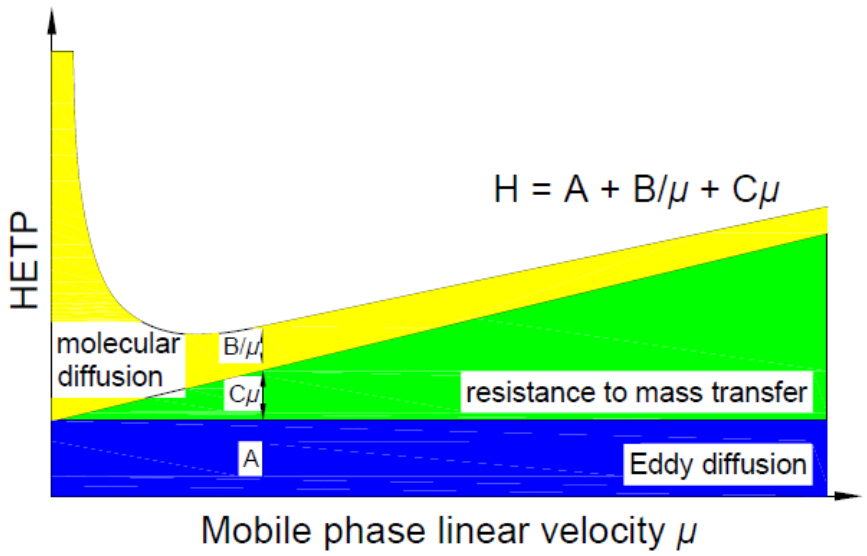

Figure 1.3. Van deemter curve considering physical, kinetic, and thermodynamic properties of a separation.

Eddy diffusion results packing imperfections as well as adsorbents with extensive particle size distributions. The mean particle diameter is proportional to the absolute height of the eddy diffusion (A term) (Seidel-Morgenstern, Schulte, and Epping 2013). Therefore, the plate height can be decreased by using smaller particles.

B term is related only in preparative systems with large adsorbent particles operated at meager flow rates. The diffusion coefficient of solute affects the longitudinal diffusion. Diffusion coefficient can be affected by changing the mobile phase composition. To achieve higher diffusion coefficients, low-viscosity solvents should be chosen, which will, besides, result in lower column pressure drops (Seidel-Morgenstern, Schulte, and Epping 2013).

At higher flow velocities, the effect of mass transfer resistance increases. The slope of the C term belongs to the nature of the packing material. The lower the contribution of the C term can be provided by using the more optimized an adsorbent in terms of pore accessibility and minimal diffusion path lengths (Seidel-Morgenstern, Schulte, and Epping 2013).

In industrial scale, proteins, polypeptides and for larger molecules adsorbent particle diameter can be about 50-100 μm, and μ is about 100-500 cm/h (Carta, Ubiera, and Pabst 2005). In this case, mass transfer kinetics dominate the separation efficiency. To enhance resolution, high temperatures may be applied to improve the diffusivity of the analyte (Thompson, Brown, and Carr 2001). However, extreme operating conditions, such as elevated temperatures are not feasible due to the fragile nature of biological analytes. Therefore, research is done to increase adsorbent material performance at mild operation conditions.

To improve separation performance, different types of adsorbents are used. For instance, to increase separation with low back pressure, porous monoliths with interconnected pores have been used (Thompson, Brown, and Carr 2001). However, reproducing the pore structures of the columns, including porous monoliths, is difficult (Thompson, Brown, and Carr 2001). By using non-porous materials, band broadening could be decreased by using a short diffusion path because separation occurs on the particle surface (Thompson, Brown, and Carr 2001). However, capacity and resolution is limited because of the low retention, selectivity, and surface area (Fornstedt, Forssén, and Westerlund 2015). Core-shell silica particles are also used for effective separation with fast flow rate and low back pressure (Guiochon and Gritti 2011). Recently, tentacle type of adsorbent materials in which linear polyacrylamide chains were grafted onto commercially on hand support matrices have been used in chromatographic separation. Tentacle structure makes easier access to solute molecules by functional groups (Bowes et al. 2009). With the help of a tentacle type of materials, static binding capacity is increased (Bowes et al. 2009).

Even if stationary phases are improved to increase efficiency of separation, still the mass transfer kinetics dominate the separation efficiency as mentioned. To investigate flow and mass transfer behavior of these novel stationary phases theoretically, intensive analysis of the velocity distribution and dispersion is required. There are many studies examining flow and dispersion behaviors of stationary phases to

estimate their convective transport and to understand the logic of improved permeability and efficiency. To illustrate, for silica particles Darcy equation,

$$\frac{\Delta P}{L} = \frac{\mu u_s}{\kappa} \qquad (1.2)$$

where;

ΔP: The pressure drop

L: The column length

μ: Dynamic viscosity

u_s: Superficial velocity

κ: Permeability

$\frac{\Delta P}{L}$ was found the linear function of the superficial velocity of the mobile phase. The relationship between velocity and pressure drop was found experimentally (Jungbauer 2005). While Darcy equation (equation 1.2) is sufficient to represent pressure drop behavior, sometimes studies to relate permeabilities to structural parameters such as porosity or an estimated equivalent particle size have not yielded successful results (Koku 2011). Furthermore, the efficiency of separation of novel stationary phases may be dominated by convection, which means that dispersion is highly controlled by velocity distribution. Therefore in-depth analyses on the geometry of stationary phases are highly essential to investigate the mass transport. However, these materials have very complex structures, and their dispersion behavior cannot be explained by the continuum description. Thus, while modeling, mesoscopic methods such as the lattice-Boltzmann simulation for flow, and random walk algorithms for mass transfer can be used, in which complex geometries can be represented precisely on the pore scale (Koku 2011).

The pore-scale modeling techniques for a given application are highly related with governing equations, assumptions for the pore-scale flow and transport equations, as

well as the length-scales of the (computational) domain (Xiong, Baychev, and Jivkov 2016). To construct a pore network model, topology and geometry of pores are needed. That is why, by using imaging techniques, obtaining 2-D structures of the real samples are highly essential to reconstruct 3-D images accurately by using statistical methods or simulations. It depends on reliable methods of high-resolution imaging and image analysis.

Accordingly, the present research was focused on obtaining and comparing 2-D (and with one particular technique, 3-D) images, and high-resolution imaging techniques to investigate and analyze the microstructure, and adsorbate localization behavior of various porous media.

Specifically, high-resolution microscopy techniques were implemented to obtain morphology information for porous media. Several studies exist about microstructure analyses of polymer-modified adsorbent materials, such as Gigacap S-650M (Koku 2011) and Sepharose XL (Bowes et al. 2009). Thus, Gigacap Q-650M as a polymer-modified adsorbent was chosen as a case study to verify applied sample preparation methods for imaging. Several large-scale simulation studies have examined the microscopic details of solute transport through a packed bed of porous or core-shell particles (Wagner et al. 2017). These simulations are based on model particles such as core-shell that computationally formed (Schure et al. 2017). However, imaged based simulations over the core-shell particles such as HALO™ have not been studied yet. HALO particles having a core-shell structure was also studied to analyses the microstructure of it. Besides, these studies may enable to simulate transport kinetics of these adsorbents by using image-based methods.

Chapter 2 gives information about ion exchange and its principles. Types of stationary phases used in chromatography separation are also described in chapter 2. Lastly, previous literature related to imaging techniques of separation phases is summarized.

Chapter 3 provides physical and chemical information about the case study adsorbents Gigacap Q-650M and HALO^{TM} particles, and staining proteins which used for getting

contrast images. This chapter also mentions about sample preparation methods and imaging techniques for electron microscopy.

Results and discussion are presented in Chapter 4. TEM, SEM, and FIB results as imaging analyses are given for both stationary phases. Both stationary phase structures were compared with each other, and applied imaging methods were discussed. Finally, recommendations and conclusions are presented.

CHAPTER 2

LITERATURE SURVEY

2.1. Stationary Phases in Chromatography

For chromatographic separations, many adsorbent resin have been improved. Most commonly, silica and polymer are two basic resin materials for chromatographic separation. The selection of adsorbents varies according to resin physical properties. They provide high surface areas for adsorption, such as 100 to 1500 m^2 /g (Harrison et al. 2003). Additionally, the path length is also an essential parameter for diffusion. It is defined as the radius of the resin, which is the maximum length a molecule will diffuse to gain access to the internal surface area of the resin (Harrison et al. 2003). Therefore, the internal surface area and the diameter of the adsorbent are important for resin performance.

There are many types of chromatography modes, such as ion exchange, reverse-phase, hydrophobic interaction, affinity size-exclusion. According to separation principles of chromatography, different types of resins are used. For example, ion- exchange resins are used as adsorbent in ion exchange chromatography, or derivatized polymer resins, with phenyl, butyl are used in hydrophobic-interaction chromatography.

As mentioned above, there are many different types of matrix materials. Characteristic of the matrix affects chromatographic properties such as efficiency and capacity. In the upcoming section, structures of stationary phases will be detailed.

2.1.1. Porous Stationary Phases in Chromatography

Chromatographic stationary phases can be classified according to their structures such as non-porous, superficially porous or totally porous. Recently, chromatographic analyses have been improved by using small stationary phase particles having

diameters approximately 1.5μm or less (Mellors and Jorgenson 2004). In monodispersed batches, these particles could be produced easily, and they have high mechanical strength to resist high pressures (Mellors and Jorgenson 2004). On the particle surface separation occurs. Because of the relatively short diffusion path, faster mass transfer occurs. However, due to the lack of surface area, there is limited capacity. For instance, 1 μm silica particles having a porous diameter of 10 nm have a surface area approximately 300 m^2/g, whereas, 1μm non-porous silica particles have 2.7 m^2/g (Mellors and Jorgenson 2004). This increased surface area is the primary reason why porous stationary phases are preferred.

Besides the advantages of separation, porous stationary phases also have disadvantages. Transport in porous media is complicated because of the disordered pore structure. Pores tend to have irregular surfaces, and some of the pores have dead ends (Xiong, Baychev, and Jivkov 2016). Transport action and flow are affected considerably. Selectivity and efficiency (optimum resolution) can be obtained by decreasing non-specific binding with the surface, improving the accessibility of adsorption sites, enhancing the specificity, and decreasing the effect of diffusion within the chromatographic bed. Because of the complexity of pore structure, many approaches have been studied on the transport process through porous media in the past (Xiong, Baychev, and Jivkov 2016). By using non-porous small particles, mass transfer may be enhanced. Pore diffusion is often rate-limited in porous materials. Figure 2.1 shows the structure of sphere stationary phases.

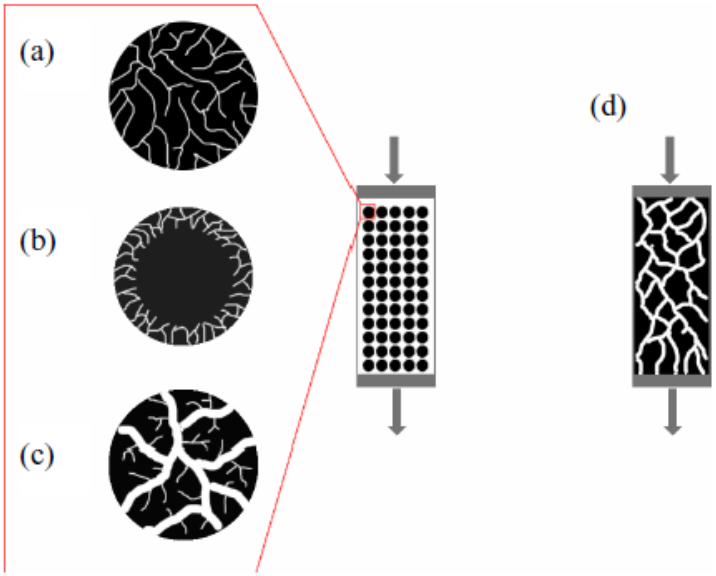

Figure 2.1. Stationary phases having different configurations of pore (white) and solid (black). (a) A traditional porous particle, (b) a core-shell particle, (c) a perfusive particle, (d) a monolithic adsorbent structural representation of spherical stationary phases (Koku 2011)

To increase flow velocity, continuous macroporous media having quite large internal channels have been developed (Leonard 1997). Binding capacity is the maximum amount of protein bound to a chromatography resin at given solvent and protein concentration conditions. It should be kept in mind that larger pore size may cause lower binding capacity. That's why alternatives were generated to improve pore mass transfer without decreasing the binding capacity too much by using gigaporous particles such as perfusive materials which composed of continuous pipe and pore matrix composites in which convection dominates on diffusional transport (Leonard 1997).

Separation performance increases by using enhanced adsorbent types. Thus, to reduce average diffusive distance by increasing the contribution of bulk flow to whole transport, modified pore-solid structure of adsorbents are produced. Because of the flexible polymer chains in the porous matrix, movement is easier. That is why mass transfer resistance within the stationary phase decreases while capacity is kept high.

Core-shell particles shown in Figure 2.1.b are also quite popular for ion exchanger. In the upcoming section, it will be described in detail.

2.1.2. Core – Shell Stationary Phases in Ion Chromatography

Fast separation requires high operating pressure. High flow rate can be achieved by operating at high pressure. However, the combination of both high inlet pressure and high flow rate generates local heat, and it results in changing the temperature of the column. That's why operating at high pressure is limited. To obtain high-performance separation, monodispersed particles having small diameters were started to be used to decrease local heating(Hayes et al. 2014). Higher pressures can be used than originally anticipated. However, using small particles increase backpressure. Separation performance may be doubled by decreasing the diameter of the particle by half. However, at the same time, this will quadruple the back pressure (Unger, Skudas, and Schulte 2008). Recently, core-shell particles which have solid core and porous shell have been investigated. Core-shell particles are also known as fused-core or superficially porous particles. These particles provide fast separation with low pressure for small and large molecules. The solid core results in a larger particle, and therefore a lower operating pressure whereas the porous shell provides high surface area for better separation. Contribution of C term in Van Deemter Equation is reduced because of the short diffusion path due to the fast mass transfer (van Deemter, Zuiderweg, and Klinkenberg 1956).

There are many core-shell particles commercially available such as HALO (Advanced Materials Technology), Poroshell (Agilent), Cortecs (Waters), Kinetex (Phenomenex) and Accucore (Thermo Fisher Scientific). The core and the shell can consist of different materials or the same materials. Different representations are shown in Figure 2.2.

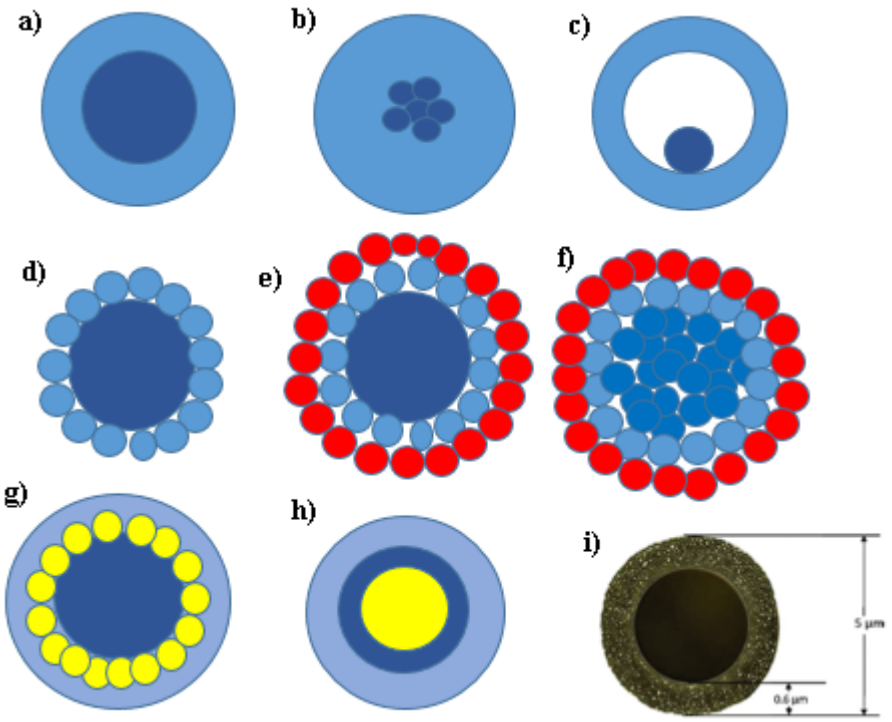

Figure 2.2 Different types of core-shell particles adapted from (Hayes et al. 2014)

The core can be a single sphere (Figure 2.2.a) or composed of small spheres (Figure 2.2.b). Figure 2.2.c shows a hollow shell with a sphere inside. The core may be surrounded by small spheres (Figure 2.2.d-e), or there may be aggregated core spheres (Figure 2.2.f). More complex structures can be utilized, such as small spheres placed into the shell (Figure 2.2.g) or multiple shells (Figure 2.2.h). Generally, the core and shell particles used in chromatography are composed of the same material, silica, but with a solid core and a porous shell (Figure 2.2.i). According to chromatographic applications, the shell thickness, porosity, and the core particle size are chosen.

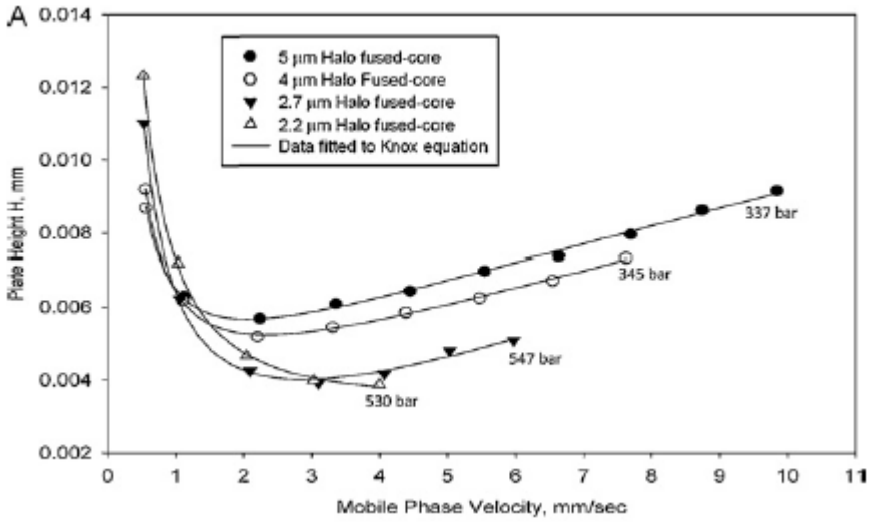

Figure 2.3. Changing of plate height vs. mobile phase velocity according to core diameter of HALO (DeStefano et al. 2012).

DeStefano et al. 2012, investigated the effect of HALO diameter on plate height, as shown in Figure 2.3. HALO particle range size was changing from 2.2 to 5 µ with the same shell thickness. They have verified that smaller particle size results in reducing the plate height, which is a measure of the peak dispersion on chromatography column that reflects the column performance. While using HALO having a diameter of 2.2 µm, the minimum plate height was not reached because of pressure limitations since HALO particles were limited to 600 bar (DeStefano et al. 2012).

2.1.3. Polymer-Modified Stationary Phases in Ion Chromatography

Polymer-modified particles as stationary phase are produced with proper porosity, and are stable over a wide range of pH. These particles can be formed from polysaccharides including cellulose, agarose, cross-linked dextran, etc. These materials also have available hydroxyl groups for activation and derivatization (Leonard 1997).

Commercially, first ion exchangers were based on dextran, which is Sephadex, it was followed by agarose-based ion exchangers such as Sepharose CL-6B, and crosslinked cellulose (DEAE Sephacel) (Amersham 1991). These ion-exchange matrices

combined spherical form and high porosity to develop flow properties and to enhance capacity for macromolecules. Later improvements have allowed the macroporosity to be increased by the extremely cross-linked agarose based media like Sepharose High Performance, Sepharose Fast Flow (Amersham 1991). These media provided good capacity, fast separation, and high resolution in ion-exchange chromatography. Several cation and anion exchangers are having the same matrix but different ligands.

There are different types of polymer-modified media shown in Figure 2.4

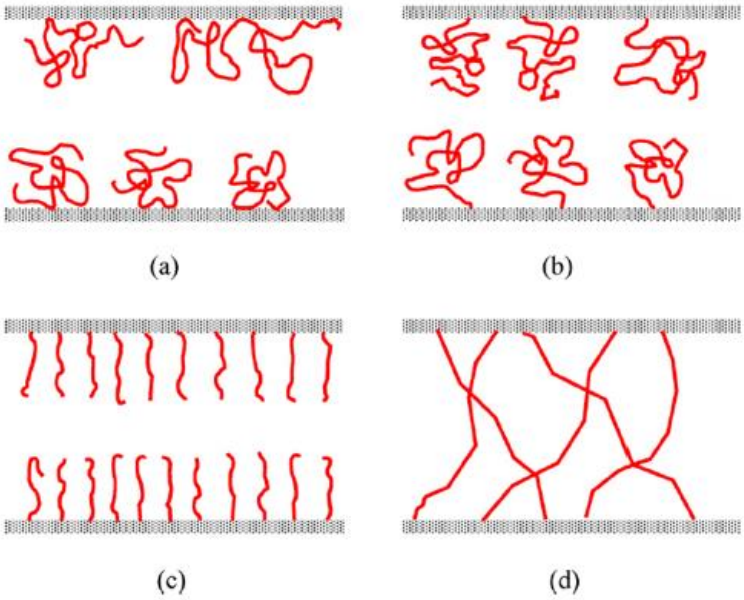

Figure 2.4. Different structure of polymer derivatives in pores of base matrix (Lenhoff 2011)

Figure 2.4.a shows covalently attached polymer having multi-point attachment per chain; grafted polymer having a single point of attachment per chain is demonstrated by Figure 2.4.b; Figure 2.4.c reflects polymer brush where grafted polymer chains are too short to form an ordinary coil, and Figure 2.4.d shows "gel-in-a-shell" hydrogel. Sepharose XL and Capto resins are examples of covalently attached polymer shown in Figure 2.4.a. UNOsphere and HyperD™ groups are some of the 'gel in a shell'

media. Table 2.1 shows that several suppliers provide the same matrix with different particle diameters.

Table 2.1. *Cation exchangers proper for protein separation* (Jungbauer and Hahn 2009)

Name of Stationary Phase	**Supplier**	**Base Matrix**	**Mean Particle Diameter (µm)**	**Mass transport mechanism**	**Typical application and features**
SP Sepharose Fast Flow	GE Healthcare	Cross-linked agarose	90	Pore diffusion	Preparative protein capture
Capto S	GE Healthcare	Highly cross-linked agarose with flexible dextran surface extender	90	Unknown Mechanism(Accelerated Transport)	Preparative protein capture; salt tolerant, very high capacity
Toyopearl SP-650M	Tosoh Bioscience	Polymethacrylate	65	Pore diffusion	Preparative protein capture
GigaCap S	Tosoh Bioscience	Polymethacrylate with flexible polymeric surface extender	65	Unknown mechanisms (accelerated transport)	Preparative protein capture; salt tolerant; very high capacity
Gigacap Q	Tosoh Bioscience	Polymethacrylate with flexible polymeric surface extender	75	Unknown mechanisms (accelerated transport	Preparative protein capture; salt tolerant; very high capacity

Functional groups in ion exchangers are very important. The types of groups specify the type and strength of ion exchanger. The presence and nature of functional groups affect the capacity of the ion exchanger. Some of these are shown in Table 2.2.

Table 2.2. *Functional groups used in polymer modified ion exchanger* (Amersham 1991)

Anion exchangers	Functional group
Diethylaminoethyl (DEAE)	$-O-CH_2-CH_2-N^+H(CH_2CH_3)_2$
Quaternary aminoethyl (QAE)	$-O-CH_2-CH_2-N^+(C_2H_5)_2-CH_2-CHOH-CH_3$
Quaternary ammonium (Q)	$-O-CH_2-CHOH-CH_2-O-CH_2-CHOH-CH_2-N^+(CH_3)_3$
Cation exchangers	**Functional group**
Carboxymethyl (CM)	$-O-CH_2-COO^-$
Sulphopropyl (SP)	$-O-CH_2-CHOH-CH_2-O-CH_2-CH_2-CH_2SO_3^-$
Methyl sulphonate (S)	$-O-CH_2-CHOH-CH_2-O-CH_2-CHOH-CH_2SO_3^-$

Bowes et al. 2009, worked with the strong cation exchangers SP Sepharose Fast Flow and the dextran-modified resins SP Sepharose XL and Capto S obtained from GE Healthcare (Bowes et al. 2009). They aimed to characterize the protein adsorption on the traditional SP Sepharose Fast Flow, Capto S and the dextran-modified resins SP Sepharose XL.

There are several types of stationary phases according to chromatographic applications, as mentioned in previous sections. In this research, anion exchanger (Gigacap Q-650M) having a quaternary ammonium functional group has been used to investigate structure. Additionally, several modes are being used in chromatographic separation. However, in this study, it is focused on one case study, which is the microstructure of the Gigacap Q-650M anion exchanger extensively. Therefore it is useful to review some of the basic principles of ion-exchange chromatography.

2.2. Ion Exchange Chromatography and Principles

Ion exchange chromatography is generally used to separate charged proteins, peptides, amino acids or nucleotides. Amino acids which form the backbone of proteins have both positively and negatively charged chemical groups. The isoelectric point (pI) is highly important (Brooks 1986). The isoelectric point of a peptide is the pH at which its net charge is zero (Brooks 1986). Depending on the pH level of environment, proteins may have positive, negative, or zero net charge.

The pI value can be calculated based on the primary sequence of the molecule. The choice of buffer pH then determines the net charge of the protein of interest. In a buffer with a pH greater than the pI of the protein of interest, the protein will carry a net negative charge; consequently, a positively charged anion exchange resin should be chosen to capture this protein.

In a buffer with a pH lower than the pI of the protein of interest, the protein will carry a positive net charge; thus, a negatively-charged cation exchange resin should be chosen. Figure 2.5 shows protein charge concerning pH value of buffer.

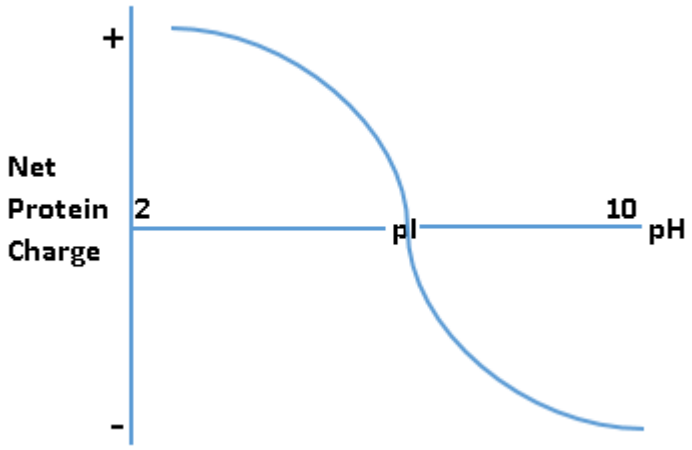

Figure 2.5. Protein net charge depends on pH level

Most ion-exchange separations consist of five main stages as shown in Figure 2.6 (Amersham 1991).

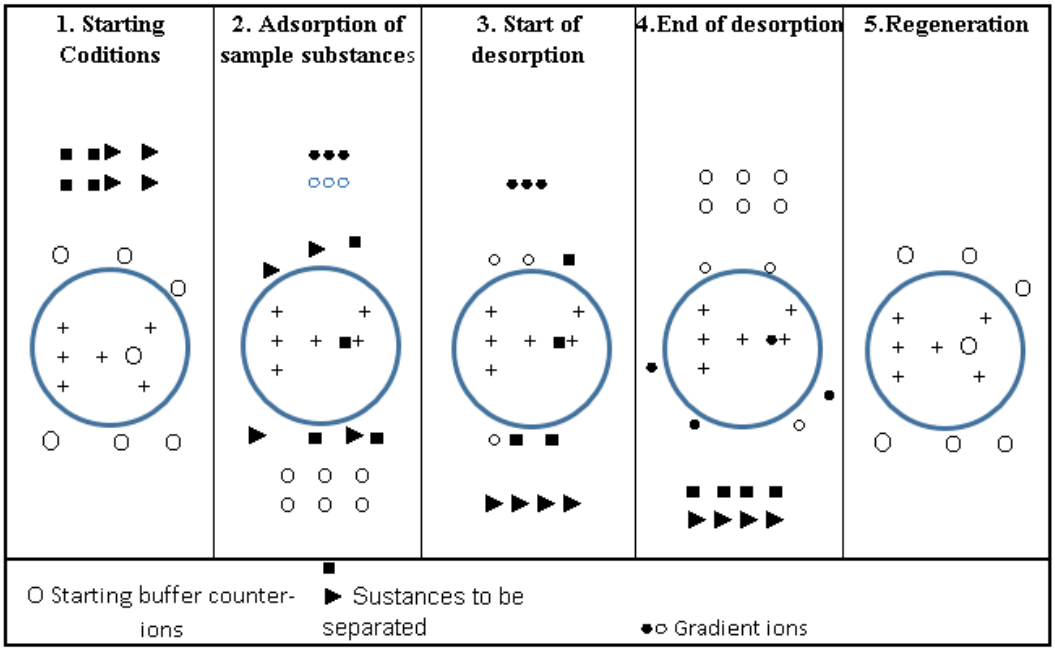

Figure 2.6. The principle of ion exchange chromatography

Figure 2.6 shows the ion exchange chromatography principle. Equilibration is the first stage in terms of pH and ionic strength allowing the binding of desired solute molecules. The exchanger has the exchangeable counter-ions.

Sample adsorption is the second stage. In this stage, solute molecules that carry charge displace counter-ions and bind reversibly. Unbounded substances can be eliminated from the exchanger by washing with starting buffer.

In the third stage, by changing to elution conditions not preferable for ionic bonding of solute molecules, substances are removed from the column. This can be done typically by increasing the ionic strength of the eluting buffer or changing its pH.

Removing of substances from the column which have not been eluted and re-equilibration at the starting conditions are the fourth and fifth stages.

There are positively and negatively charged ion exchangers. Positively charged ion exchangers have negatively charged counter ions which are mobile and available for exchange. These are called anion exchangers. In contrast, negatively charged ion exchangers have positively charged mobile counter ions which can exchange with

other cations, and these are called cation exchangers. Figure 2.7 illustrates the principles of cation exchangers.

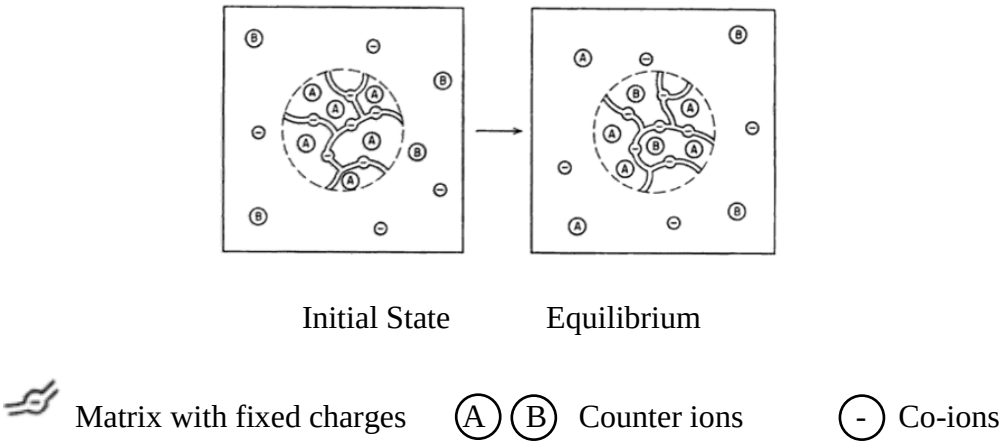

Figure 2.7 Cation exchanger containing counter ions A is placed in a solution containing counter ions B (left). The counter ions are redistributed by diffusion until equilibrium is attained (right) (Helfferich 1995)

There are many alternatives for matrix materials such as synthetic resins, polysaccharides, or organic compounds. Chromatographic properties such as efficiency, capacity, recovery, mechanical strength, chemical stability, or flow are affected by characteristics of the matrix (Amersham 1991).

Ion exchangers consist of a base matrix generally in the form of porous beads to increase the surface area for adsorption (Jungbauer and Hahn 2009). Positively or negatively charged stationary ligands are on this base matrix. To increase adsorption capacity, charged polymer can be grafted onto the matrix instead of using small charged ligands (Jungbauer and Hahn 2009).

Depending on protein net charge, anion or cation exchangers are used for separation of proteins. In a buffer solution pH is greater than pI, protein is negatively charged; therefore, anion exchange resin is chosen to adsorb the proteins. If the buffer solution pH is lower than the pI, protein is positively charged, and cation exchange resin is used to capture the proteins.

2.3. Imaging Modes in Electron Microscopy Techniques

In this study, TEM, SEM, and FIB imaging techniques were used to obtain 2-D and 3-D structural information of stationary phases. There are several differences between TEM, SEM, and FIB techniques. In general, it is possible to obtain higher resolution images using TEM compared to SEM. Additionally, for TEM imaging thin section samples are needed (under 100nm), but for SEM imaging this is not needed. The TEM technique provides 2-D images, whereas the secondary-electron (SE) mode of SEM can provide information on topography. Backscatter electron mode (BSE) of SEM can provide two-dimensional projection images. FIB is used to obtain genuine 3-D topography thanks to its property of capturing 2-D serial-section images. The imaging technique of FIB is done by using SEM, which is called FIB-SEM imaging. While gallium ions are directed on the surface of the specimen, an electron beam (from the inbuilt SEM) is used to form 2-D images.

Imaging formation principles of TEM and SEM are illustrated in Figure 2.8.

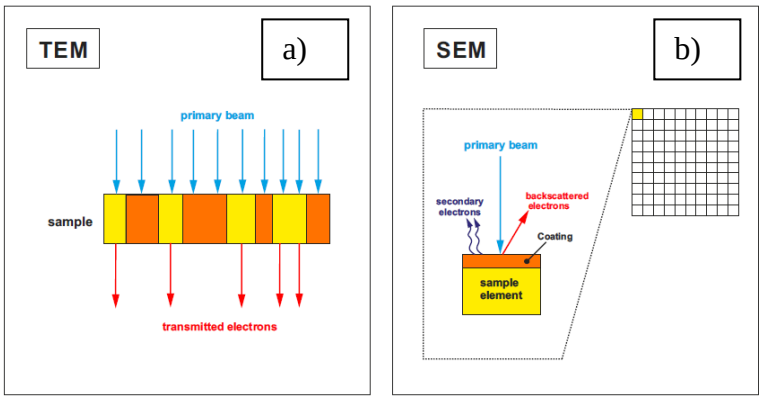

Figure 2.8. TEM and SEM electron microscopy principle

As illustrated in Figure 2.8.a, images can be obtained by the help of a beam composed of high-energy electrons. In TEM, Images can be formed due to the various degrees of transmittance of electrons over the sample. The dark region shows the scattered electron beam over the surface of the specimen, whereas the areas where the electron beam passes through from the surface of the specimen called electron-transparent

region seems as bright. Light and dark phases occur because of the density or atomic number differences of material. The more scattered electron beams may face obstacles because of the heavier elements (Koku 2011). For resins, the variability of atomic numbers along the surface is not enough to get contrast or to specify the structure of the sample by scattering or transmitting of electron beam (Egerton 2006). Therefore, artificial contrast is implemented to investigate the structure of the specimen by staining using heavy-metals (Koku 2011). Generally, en-bloc staining method is used to obtain contrast by using lead citrate, and uranyl acetate. Detailed methods will be described in section 3.3.

SEM imaging is another mode of electron microscopy. There are two common types of modes of SEM imaging. Davison and Germer (1927) experimented with SEM imaging and they have seen that traveled primary beam can be reflected (backscattered) from the bulk specimen (Egerton 2006). The primary beam which supplies energy to the atomic electrons which are present in a solid can be released as a secondary electron(SE) (Egerton 2006). Electrons are emitted with a range of energies and it makes hard to focus them into an image by electron lenses (Egerton 2006). Nevertheless, alternative mode is implemented for image formation which uses different principles. By using an electron probe having a small diameter which is scanned over the specimen, making use of the fact that electrostatic or magnetic fields, performed at accurate angles to the beam, can be operated to change its direction, primary electrons are focused into it. The rectangular region of the specimen called as raster (Figure 2.8.b) can be covered by scanning synchronously in two perpendicular directions. By the help of it, an image of a square region can be obtained by pick up secondary electrons from each point on the sample. Images formed by using the SE mode are highly dependent on structural or geometry properties of sample, i.e., alignment and form of surface elements (Koku 2011) That is why obtained contrast using the SE mode is mainly because of the topography of the specimen. Contrarily, in BSE mode, an image is obtained by the electron beams which is reflected back from the sample. Structure and the atomic composition of the

specimen highly affect the backscattered electrons amount. That is why one can conclude that bright regions are formed because of the dense materials which cause a large amount of backscatter, whereas, dark regions are displayed because of the low-dense areas in BSE mode.

If the sample to be imaged is electrically non-conducting, while imaging by SE-and BSE based SEM, the sample may be destroyed because of the charging caused by the primary beam. For this reason, coating by conductive layer such as gold-palladium over the surface may be necessary in SE mode. However, If BSE mode is used, the primary beam can be dissipated by coating and identify the structure may not be easy. Thus, coating having low atomic numbers such as carbon should be used when needed (Krinsley, D. H., Pye, K., Boggs, S., and Tovey 1998).

Specimen thickness is one of the important factors to obtain a good resolution for TEM imaging mode. To eliminate this obstacle, a combination of an imaging and precision manipulation tool allows stripping the material with gallium beam and imaging the milled section faces by scanning with the electron beam (Rigort and Plitzko 2015) This approach is called as FIB/SEM tomography. FIB-SEM mode of electron microscopy has the advantage of imaging a wide range of volume of samples (Hagita, Higuchi, and Jinnai 2018). Figure 2.9 shows the SEM and the FIB directions roughly concerning one another. The ion beam works over the z-direction which means that the ion beam cuts the sample perpendicularly over the surface of the specimen. Meanwhile, the cross-sectional surface of the specimen is imaged by SEM (Hagita, Higuchi, and Jinnai 2018). Beam current and the voltage are important operating parameters for FIB. Generally, beam energy is around 10-30 keV, and beam currents can be changed from 1pA to 10nA (Rigort and Plitzko 2015). If needed, 2-D images formed by SEM can be used to construct 3-D images with the help of simulation tools such as ImageJ.

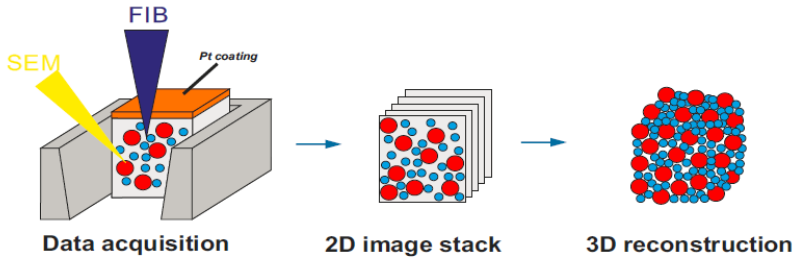

Figure 2.9. 3-D reconstruction principle using FIB-SEM.

Large specimen thickness can cause lower resolution. That is why it is useful to work with stained samples while imaging by FIB.

Extraction of the specimen occurs by the impact of high energy Ga+ ions. However, it may cause some damage to the specimen. The transfer of thermal energy to the specimen causing local heating and placing of Ga+ ions into a superficial layer of the specimen are two damage mechanisms, and these mechanisms highly depend on increasing in voltage, ion current and the angle of incidence (Rigort and Plitzko 2015). To decrease milling damages over the sample, platinum deposition may be performed on the specimens.

Summary of imaging methods and modes are given in Table 2.3. However, resolution highly depends on the working parameter of microscopy, atomic number of specimen, and the structure of the specimen. That is why accurate resolution degree cannot be specified.

Table 2.3. *Imaging methods and the principles*

Method	2D/3D	Principle	Resolution (Koku 2011)	Comments
TEM	2D	Electron transmission	0.2- 0.3 nm	For imaging, thin and conducted surface needed
SEM-SE	2D	Releasing of secondary electron	10-20 nm for insulators	Coating by conductive layer is needed
SEM-BSE	2D	Backscattered electron	10 nm for gold	Low atomic number coating is needed
FIB	3D	Milling with gallium beam and imaging by scanning electron beam	<15 nm	Only platinum deposition is needed

2.4. Investigation of Chromatographic Stationary Phases by using Electron Microscopy Techniques

Different types of ion exchangers have been investigated to understand the chromatographic performance in past studies. Mostly, previous studies having the SEM, TEM and FIB imaging techniques were analyzed. Additionally, 3-D reconstruction from the 2-D images were reviewed.

To get an idea of internal pore properties in microporous chromatographic media, electron tomography using Atomic Force Microscopy (AFM) and TEM was applied by Yao et al. (Yao et al. 2006). Their studies mainly include imaging techniques and the 3-D reconstruction using 2-D images. They used three cation exchangers which are Toyopearl SP-550 C and SP-650 C (Tosoh Biosep, Montgomeryville, PA) and CM Sepharose FF (GE Healthcare, Piscataway, NJ). Toyopearl SPs have sulfonated propyl functional groups on a methacrylate copolymeric base matrix. Whereas, Sepharose FF is composed of cross-linked agarose matrix derivative with weak carboxylate groups. To get high resolution in Electron Microscopy, lysozyme solution

was used to let the protein molecules bind to the adsorbent. The same method is used in this thesis to increase the contrast under Electron Microscopy, but instead of lysozyme, α-lactalbumin was used. Since, the proteins which are adsorbed by the stationary phase can improve the electron density of the pore region. To obtain some information on the extent of artifacts by sample preparation in EM, TEM, and AFM technique were used.

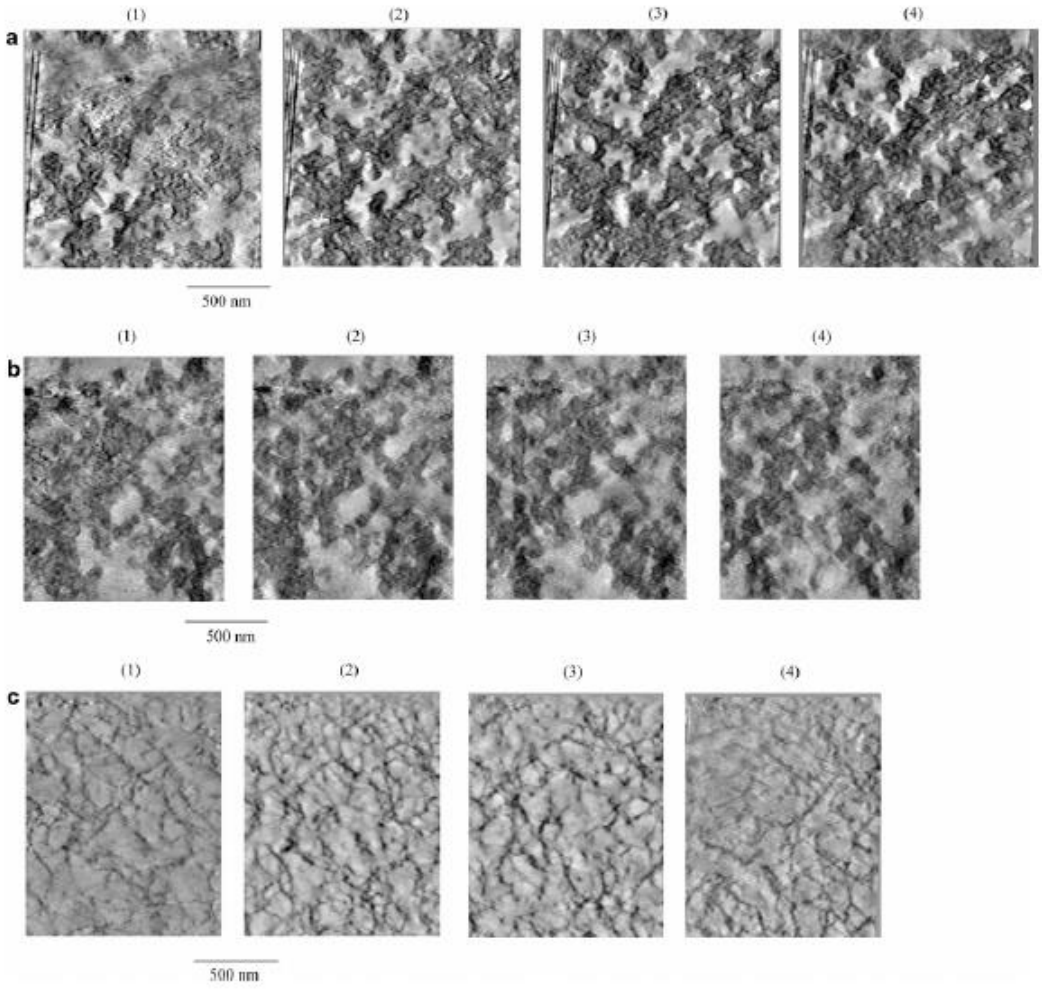

Figure 2.10. Tomographic reconstruction of a)Toyopearl SP-550 C, b) Toyopearl SP-650 C, c) CM Sepharose FF. Each sets from 1 to 4 are the slices 50 nm apart along to z-axis of the sample (Yao et al. 2006).

Light areas in Figure 2.10.a and b show the methacrylate base matrix. The darker lines show pore walls which are bound by protein. In Figure 2.10.c cross-linked agarose base matrix is stated as a dark region, and light regions are pore space as shown in Figure 2.10.c. The Toyopearl materials include pore channels, and along the channels, proteins are adsorbed. Toyopearl adsorbents have similar pore geometry, but SP-650 C has bigger pores than the SP-550-C. There are voids in CM Sepharose between cross-linked agarose bundles, and it causes larger porosity than the others. Besides 2-D imaging by using electron microscopy techniques, Yao et al. 2006 have done 3-D reconstruction.

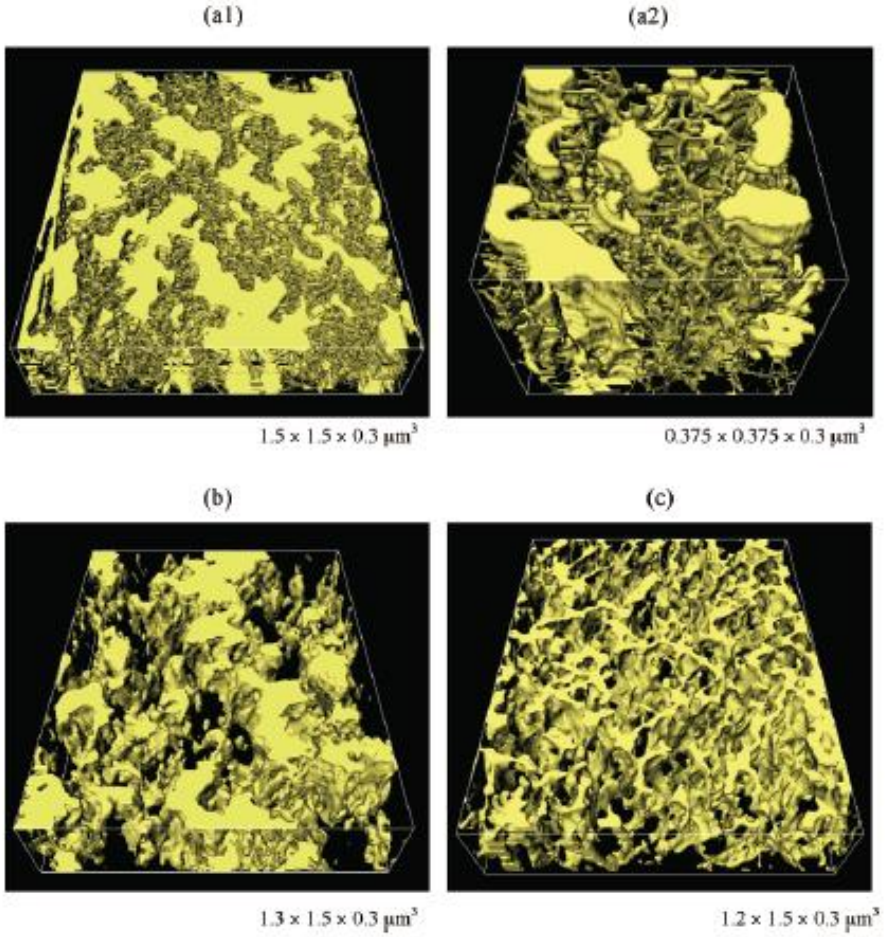

Figure 2.11. 3-D reconstruction of Toyopearl SP-550 C (a1 and a2), Toyopearl SP-650 C (b), and CM Sepharose FF (c) (Yao et al. 2006)

3-D reconstruction provides information on the internal structure. In Figure 2.11, bright regions correspond to solid. Larger pores exist in SP-650 C (Figure 2.11.b), and it has a simple structure, SP-550 C (Figure 2.11.a1 and a2) has small pores aggregated into the discrete pore sides. SP-550 C has more accessible surface area for adsorption, and it results in high binding capacity. Voids occur among the entangled agarose bundles in Sepharose FF (Figure 2.11.c).

In the same manner, Trilisky et al. 2009 have studied anion-exchangers with monolithic and perfusive structures to compare permeability, porosity, and binding capacity (Trilisky et al. 2009). Electron microscopy techniques were used to observe pore structure of monoliths which are commercially named as DEAE CIM disks, Proswift WAX-1S, and UNO Q-1, and perfusive material PL-SAX 4000Å 10µm. By using Adobe Photoshop, Electron images were binarized, and to predict porosity and binding capacity Matlab version 7.1 with the Image Processing Toolbox was used (Trilisky et al. 2009).

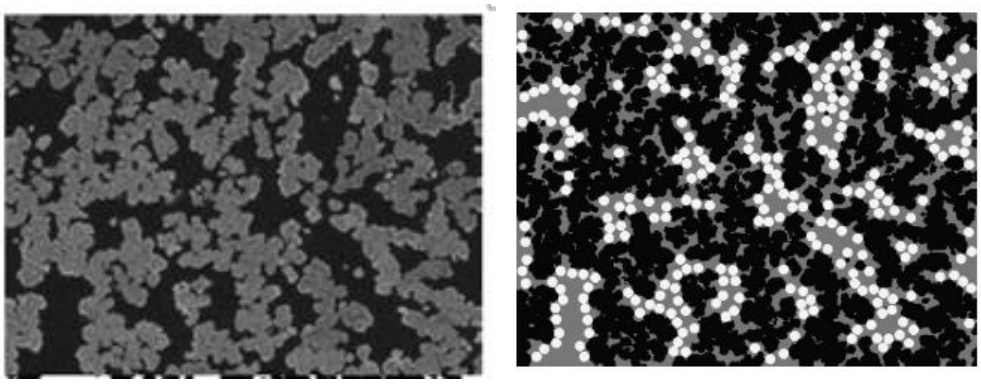

Figure 2.12. SEM image of CIM disk calculation of porosity using the binarized SEM images (left image), binding capacity prediction from the random placement algorithm using the binarized SEM image(right image) (Trilisky et al. 2009)

Solid polymer matrix which is polymethacrylate, is represented as lighter areas as seen in Figure 2.12 (left image), darker areas are the pore space. By using the SEM images of CIM disk and binarized image of it, porosity calculation, pore size distributions, and capacity predictions were obtained by applying basic operations of mathematical

morphology. (Trilisky et al. 2009). In Figure 2.12 (right image), the *black areas are the solid polymer matrix, grey areas are the pore space, and the white disks are the probes with 0.66 μm.*

Bowes and his colleagues have researched adsorption of protein on traditionally SP Sepharose Fast Flow (SP FF) and dextran modified resin SP Sepharose XL and Capto S (Bowes et al. 2009). In this research, protein size effects on adsorption have been worked. Used proteins were lysozyme having 1.6 nm radius and bovine lactoferrin having 2.8 nm radius. TEM and SEM analyses were done to investigate the differences in protein adsorption and localization behavior in ion exchangers. Figure 2.13 shows TEM images of Q Sepharose FF (Figure 2.13.a) and XL (Figure 2.13.b) with low adsorbed protein, whereas Figure 2.14 shows TEM images of the same adsorbents with high adsorbed protein.

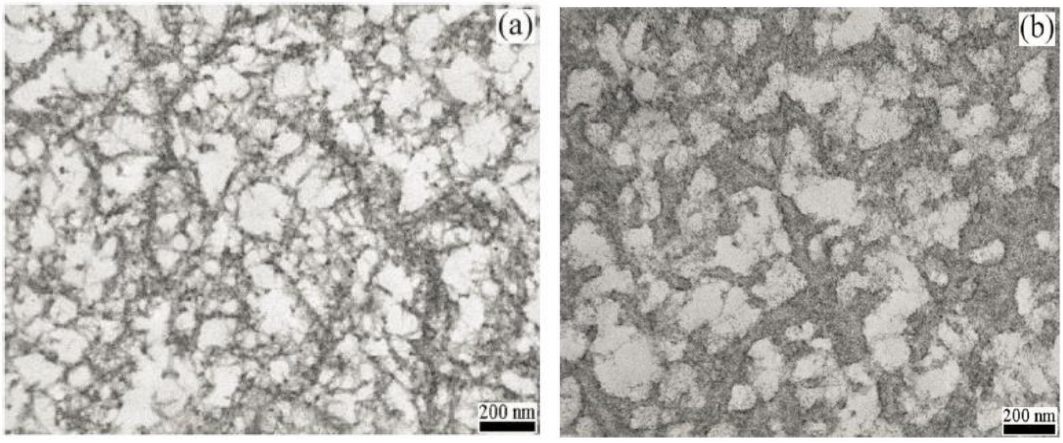

Figure 2.13. TEM images of Q Sepharose FF(a) and Q Sepharose XL (b) with low adsorbed protein (Bowes et al. 2009).

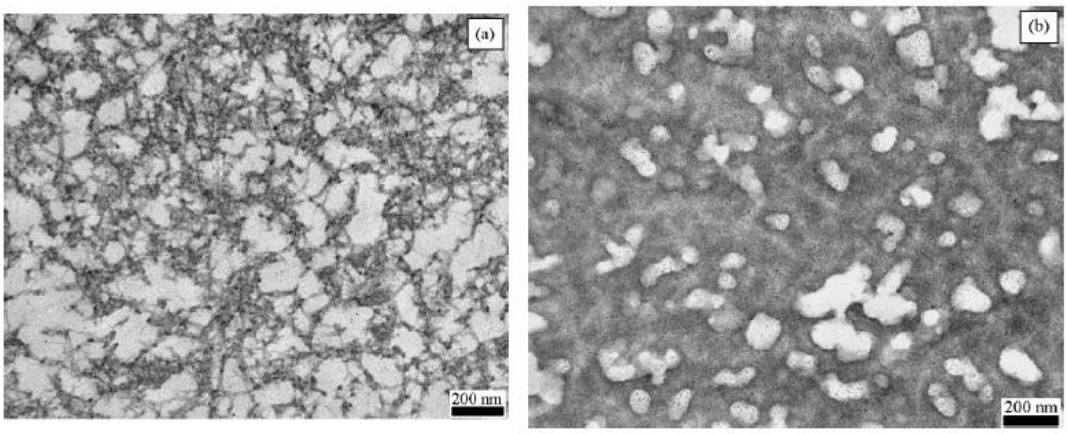

Figure 2.14. TEM images of Q Sepharose FF(a) and Q Sepharose XL (b) with high adsorbed protein (Bowes et al. 2009).

In Figures 2.13 and 2.14, stained proteins are shown as dark region, whereas light regions reflect as voids. When compared low and high protein adsorption on Sepharose FF and Sepharose XL, darker areas are much higher when used higher protein amount. While comparing low protein-loaded Sepharose FF & XL, proteins have been attached over the dextran layer in Sepharose FF. However, it seems that proteins are also linked into the dextran layers.

To investigate the protein adsorption behavior, SEM analyses were also done by Bowes and his colleagues,2009.

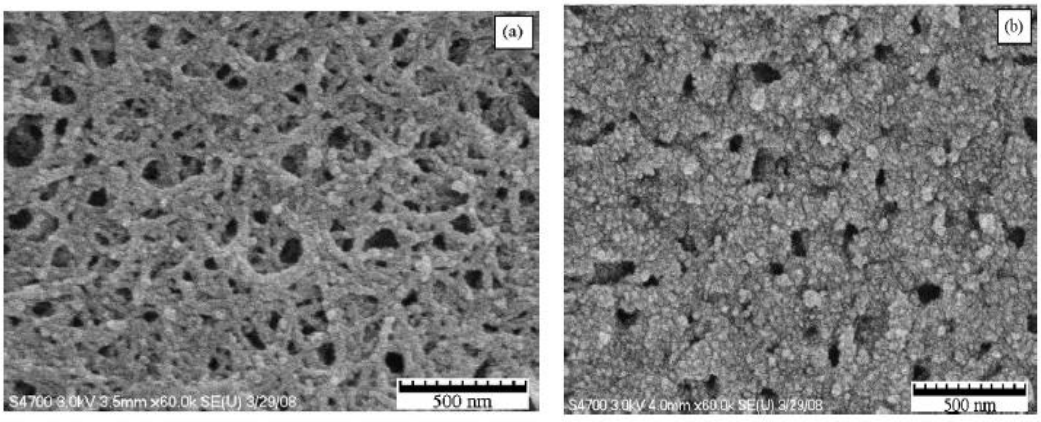

Figure 2.15. SEM images of Sepharose FF (a) and Sepharose XL(b) with high adsorbed protein (Bowes et al. 2009)

As seen in Figure 2.15.a, proteins have been localized over the agarose fibers surface in Sepharose FF, but proteins are also divided into the dextran layer in Sepharose XL (Figure 2.15.b). Proteins cover higher volume fraction in Sepharose XL than the Sepharose FF.

To investigate the retention and transport of protein along the adsorbent, polymer and the pore structures were highly researched. Conventional and polymer-modified media exhibit differences in properties and mechanism concerning chromatography such as binding capacity, and interphase transport, which was researched by Lenhoff (Lenhoff 2011). The aim of chromatographic operation is partitioning of protein into the layer of polymer. Driving force for sorption is electrostatic on conventional media, but the space ready for absorption may be restricted (Lenhoff 2011). This space is an accessible surface area for conventional media, whereas for polymer-modified media, it is the volume of the polymer. Generally, analyses based on prediction roughly suggest that volume is limiting on dextran modified agarose; however, available ligand charge may be limiting for proteins having high charged density (Lenhoff 2011). Still, Lenhoff could not reach the mechanistic basis for retention, especially the protein-surface interaction.

To characterize the structure of packed beds of small particles, there are also nondestructive and quantitative approach which is 3-D reconstruction by using their 2-D images. Tallerek et al. 2011 have been used 2.6μm sized Kinetex core-shell particles in their studies (Bruns and Tallarek 2011). They have obtained valuable experimental benchmark for researches of morphology-transport relationships in chromatographic media by using the reconstructed packings (Bruns and Tallarek 2011). For instance, they allow the evaluation of different algorithms for computer-generated packings for their ability to ensure more realistic model packings, and also for simulations of hydrodynamic flow and mass transport, they are able to serve as true packing microstructures.

Guiochon and Gritti have compared column properties packed with fully porous, shell, and pellicular particles. The volume fraction of superficially porous particles is much lower than the core-shell particle. Thus, retention on column packed with porous particle is much lower than with core-shell particles. Column packed with pellicular particles had diameters between 35-50 µm permeability is greater than new core-shell particles having a diameter around 1.7µm (Guiochon and Gritti 2011).

Guiochon has also discussed about Pore Size Distribution (PSD) and SEM imaging of nonporous silica cores used to produce the 2.7 µm particles. Figure 2.16.a has illustrated SEM images of HALO particles. SEM images of Kinetex core-shell particles having 1.7 µm diameter have been shown in Figure 2.16.c and 2.6 µm Kinetex core-shell particles was stated in Figure 2.16.b. Shell average thickness are 600 nm for HALO particle, 270 nm for 1.7µm Kinetex and 350 nm for 2.6µm Kinetex.

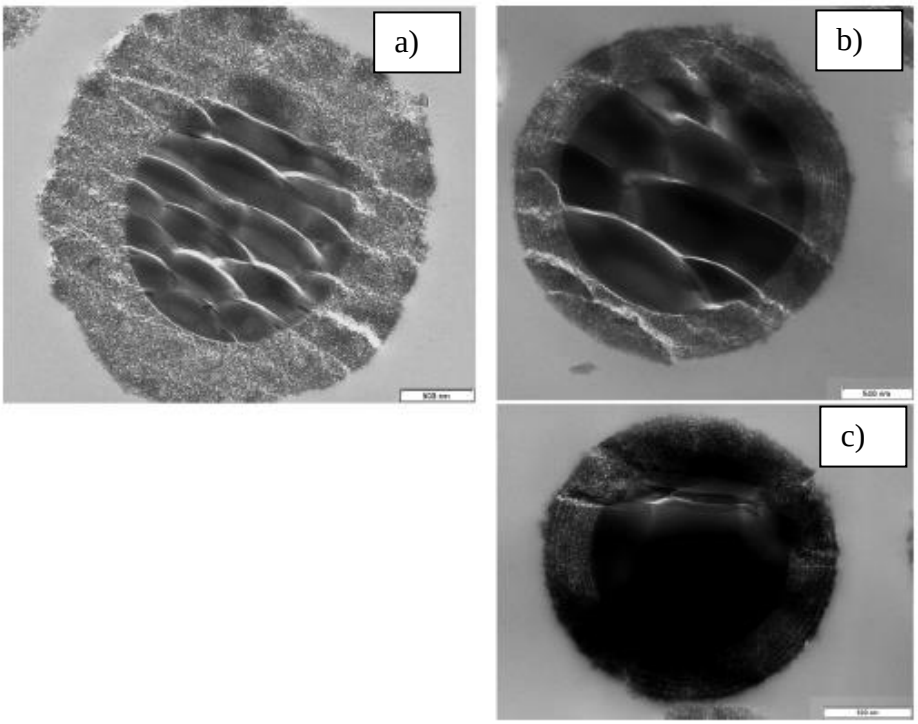

Figure 2.16. SEM cuts: 2.7µm HALO core–shell particles (a); 2.6µm Kinetex core–shell particles(b), 1.7µm Kinetex core–shell particles (c) (Guiochon and Gritti 2011).

Different core-shell particles have been analyzed concerning their chromatographic performance. Wagner et al. 2017 have been studied on HALO having very large pore (1000 Å) to separate large biomolecules (Wagner et al. 2017). They aimed to design core-shell particles having different pore sizes to find the best for analytical separation. They have characterized the HALO by using SEM and also to obtain a 3-D image they have used the FIB. Figure 2.17 shows the HALO particle microscopic images. Figure 2.17.a shows the SEM image, whereas the FIB image have been shown in Figure 2.17.b. From the SEM images, the porous side of the HALO is visible but core and the shell side of the particle is much clearer in FIB images. Wagner et al. 2017 have been used these images to obtain particle sizes and shell thickness.

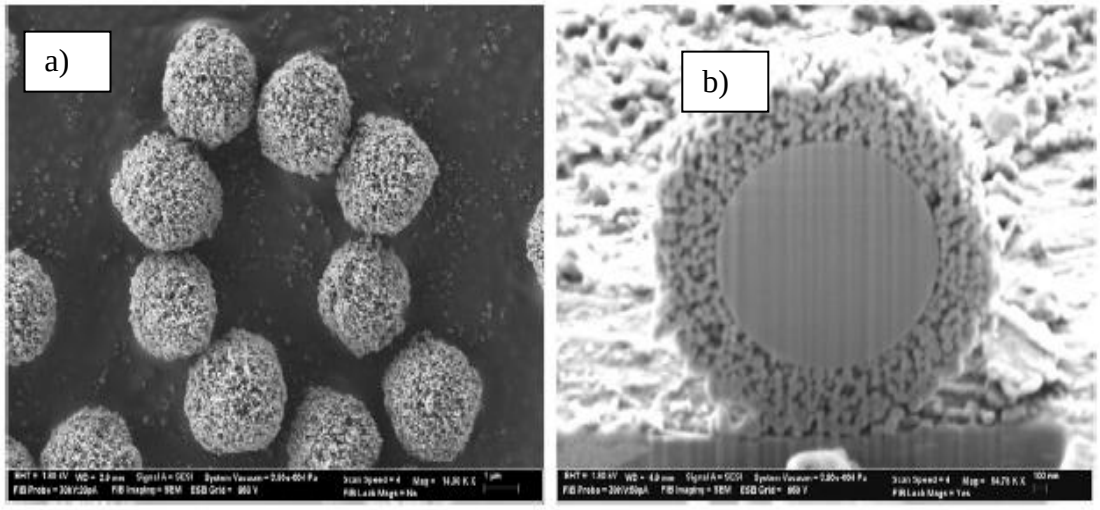

Figure 2.17. SEM of superficially porous particles with 1000 Å pores. (a). FIB SEM of 1000 Å superficially porous particles with a porous shell thickness of about 0.5µm (b) (Wagner et al. 2017)

Reconstruction of 2D images have been highly used for flow and mass transfer modeling. Koku et al. 2011 modeled the flow of the polymeric monolith Convective Interaction Media (CIM) by using reconstructed SEM images of monolith. They have used the Lattice-Boltzmann method to obtain velocity distribution and flow properties such as permeability and average velocity (Koku et al. 2011).

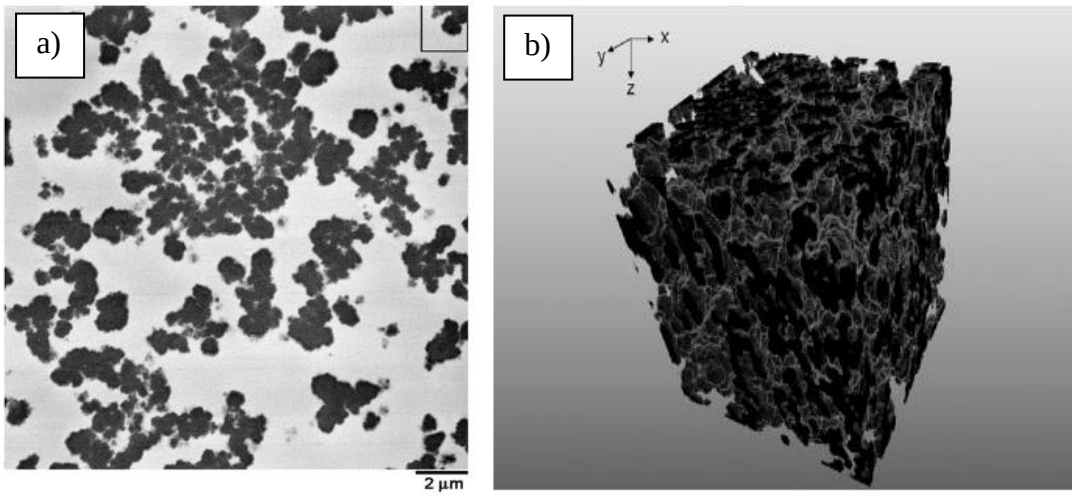

Figure 2.18. Raw section of CIM by backscattered SEM (a); reconstructed image of CIM (b)

2D (Figure 2.18.a) and 3D (Figure 2.18.b) images of CIM were obtained by backscattered SEM and 3D image of it. Black areas in Figure 2.18.b indicates the solid matrix. Pore size distribution of the raw sample block was obtained from image analysis (Koku et al. 2011).

After obtaining velocity distribution by the Lattice-Boltzmann method, Koku et al. 2012 have modeled mass transfer by using the random-walk algorithm (Koku et al. 2012).

Schure et al. 2017 have used FIB and the SEM images of HALO particles to analyze flow near into and out of the particle. Figure 2.19.a and b show the SEM and the FIB images of HALO experimentally. Figure 2.19 c and d show the simulated view of the HALO particle. They have concluded that simulated and the experimentally imaged particles are similar to each other. Therefore, they have used HALO images after reconstruction while simulating the flow in the pore by using Lattice- Boltzmann method (Schure et al. 2017).

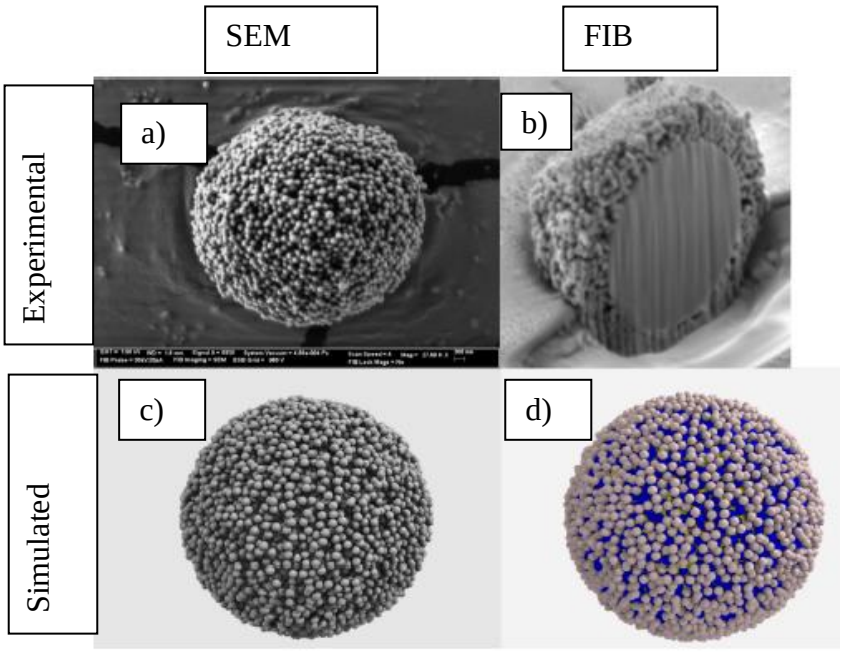

Figure 2.19. Visualization of the experimental (a, b) and simulated (c, d). Different external views showing the synthetic particle (Schure et al. 2017)

Up to now, mentioned findings of previous researches were related to imaging analyses and the reconstruction of 2-D images. However, there are also researches on stationary phases concerning other properties such as binding capacities, static capacities, and permeability and so on.

Tallarek et al. 2002 have studied C18-silica monolith to derive characteristic lengths with regard to its hydraulic permeability and dispersion (Tallarek, Leinweber, and Seidel-Morgenstern 2002). They have obtained longitudinal dispersivity concerning Pe number.

Kaphingst et al. 2010, have worked on binding capacities of Q Sepharose XL, Capto Q, and Source 30Q by using test proteins which are Bovine Serum Albumin, lipolase, and lysozyme (Kaphingst, Persky, and Lachance 2010). According to their findings, Capto Q binding strength is in between Q Sepharose XL and Source 30Q, whereas Q Sepharose XL resin has the highest binding strength.

Pore structure characteristics have effects on static capacity and transport properties. Dynamic binding capacity data from the point of structural information like pore size distribution is useful to investigate adsorbent selection. That is why Yao et al. have researched characterization of anion exchangers by using inverse size-exclusion chromatography analyses.

In my study, we focused on mostly electron microscopy imaging of anion exchanger which is Gigacap Q-650M (polymer modified exchanger) as a case study, and also on 3.4 μm and 5 μm HALO^{TM} core-shell particles microstructures.

As mentioned before, it is not enough to use continuum equations to model flow and mass transfer for the materials having complex geometry. In this case, a more rigorous mechanistic analysis of the complex interaction of flow and mass transfer with core-shell or polymer-modified stationary phases should include a description of actual pore structures. Mesoscopic approach is needed. In the long term, these microscopic analysis of Gigacap Q-650M and HALO can be used while modeling of flow and mass transfer using simulating algorithms.

CHAPTER 3

MATERIALS AND EXPERIMENTAL METHODS

3.1. Materials

3.1.1. Stationary Phases and Staining Proteins

In this study, two adsorbent particle types, namely the Gigacap Q-650M (TOYOPEARL) having strongly anion exchanger group-Quaternary amine, and HALO^{TM} core-shell particles which was provided as a gift via Mark Schure from Advanced Materials Technology were used. To investigate the similar characteristics of Gigacap resins produced by the same manufacturer, Gigacap S-650M which is the cation exchanger in unpublished research of Koku (Koku 2011) were compared with Gigacap Q-650M.

Gigacap Q-650M is anion exchange resin having a high binding capacity for the capture and purification of proteins, and it is the polymer-modified anion exchanger of TOYOPEARL HW-65 resin. The resin consists of a base material of hydroxylated methacrylic polymer beads which have been chemically modified to provide a higher number of anionic binding sites and functionalized with quaternary amine (Q) strong anion exchange groups (Tosoh Bioscience LLC. 2019). It has a 100 nm pore size and a 75 μm bead size. The manufacturer has not explained the secondary polymeric phase of Gigacap Q-650M, polysaccharide like dextran may be the secondary polymeric phase (Koku 2011). Gigacap Q-650M resin chemical structure is similar to TOYOPEARL HW-65 resin. That is why the chemical structure of TOYOPEARL HW (H=Hydrophilic, W=Water-compatible) resin was illustrated in Figure 3.1.

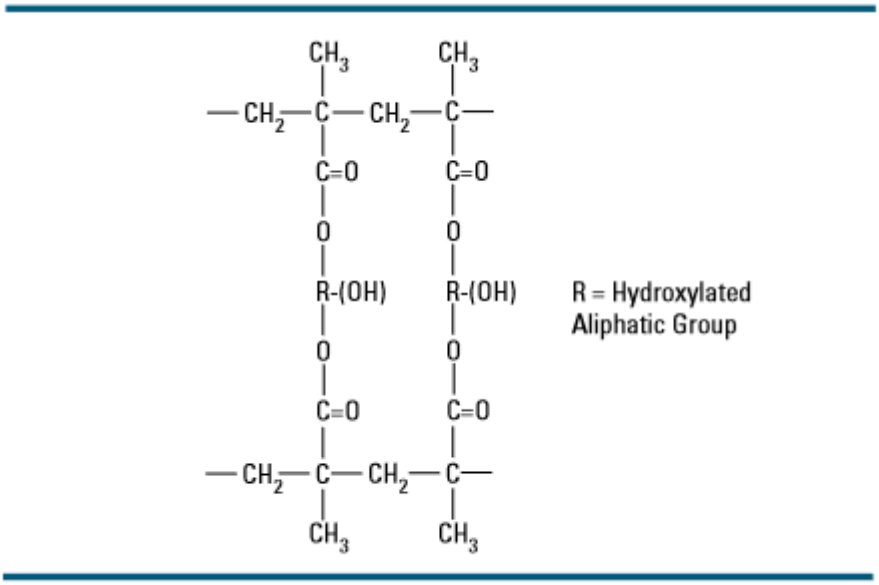

Figure 3.1. Resin chemistry of TOYOPEARL HW resins (Hydroxylated Acrylic) (Tosoh Bioscience 2014)

Gigacap Q-650M chemical structure is stated as (HW-65) -O-R'-N+-$(CH_3)_3$

(Bioscience 2014).

Gigacap S-650M is cation exchange resin. It has the same base matrix which is the hydroxylated methacrylic polymer beads like Gigacap Q-650M. It is also chemically modified to supply a higher number of cationic binding sites, and it is functionalized with sulfopropyl (S) strong cation exchange groups (Tosoh Bioscience LLC 2019).

HALO particles having the core-shell structure have been developed for high-resolution analysis of large proteins. They provide tight peak widths and enhanced resolution for characterization of bio molecules in comparison to fully porous particles. Two different HALO particles having 3.4 µm and 5 µm in size were used. They have high stability at high temperatures and low pH. Separations are due primarily to hydrophobic interactions and differences in hydrophobicity among analytes. Chemical structure of HALO 3.4 µm was shown in Figure 3.2.

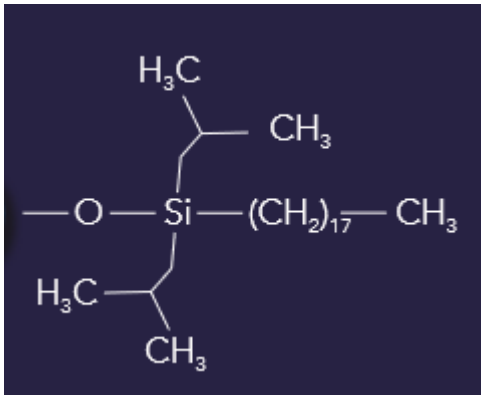

Figure 3.2. Chemical structure of HALO 3.4 µm (Advanced Materials Technology 2019)

Ligand of HALO 3.4 µm is di-isobutyl octadecylsilane as shown in Figure 3.2.

HALO 5 µm provides very high resolution and high peak capacity peptide separations (Advanced Materials Technology 2019). Figure 3.3 shows the chemical structure of HALO 5 µm.

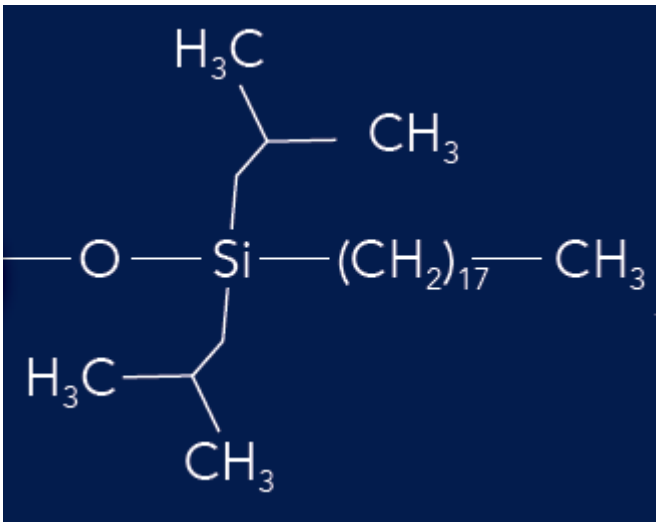

Figure 3.3. Chemical structure of HALO 3.4 µm (Advanced Materials Technology 2019)

Ligand of HALO 5 µm is di-isobutyl octadecylsilane as illustrated in Figure 3.3.

Detailed properties of adsorbents are tabulated in Table 3.1.

Table 3.1. *Physical and chemical properties of adsorbents*

Adsorbent	Base Bead	Pore Size	Particle Size(µm)	Bonded Phase	Dynamic Binding Capacity(g/L)	pH Stability
Gigacap Q-650M	Hw-65	100µm	75	C4	175 for BSA	3-13
Gigacap S-650M	Hw-65	100µm	75	C4	156 for human IgG	2-13
3.4µm HALO™ Core-Shell Particle	----	400Å	3µm Fuse Core, 0.2µm Porous shell	ES-C18	-----	2-9
5µm HALO™ Core-Shell Particle	-----	160 Å	3.3µm Fuse Core, 0.6µm. Porous shell		------	1-8

All data stated in Table 3.1 have been obtained from HALO and Gigacap Q-650M technical data sheets (Advanced Materials Technology Inc. 2018) (Tosoh Bioscience LLC. 2019).

α-Lactalbumin for both Gigacap Q-650M & HALO core-shell particle, bovine serum albumin and chicken egg lysozyme for HALO particle were used as staining proteins. These proteins are arbitrary substrates just used as marking or staining proteins due to their simple structures and small sizes. Only α-Lactalbumin was selected to attach to

functional group in Gigacap Q-650M since α-Lactalbumin is positively charged in phosphate buffer solution at pH 7.2. However, all three proteins are used to investigate the adsorption performance of HALO particle.

Properties of proteins are stated in Table 3.2.

Table 3.2. *Characteristic properties of proteins*

Protein	Manufacturer	Molecular weight[a] (kDa)	PI[a]	Hydrodynamic Radius (nm)	Estimated charge at pH 7	Lot No
α-Lactalbumin	SIGMA	14.2	4.5	2.1[b]	+5[c]	SLBM1466V
Bovine Serum Albumin	SIGMA	66.8	4.7-4.9	3.3-4.3[d]	-13[e]	M12177P6155
Chicken egg lysozyme	SIGMA	14.3	11.3	1.9[b]	-9[c]	SLBT5160

[a] Supplier data sheet

[b] Estimated using diffusivities and the Stokes-Einstein equation (Aragon and Hahn 2006)

[c] Estimated from sequence data (Putnam 2013)

[d] Radius estimated by Stokes-Einstein from diffusion coefficient of $D = 4.34*10^{-6}$ $cm^2\ s^{-1}$ (Hawe et al. 2011)

[e] Estimated net charged of BSA (Barbosa et al. 2010)

3.2. UV-Visible Spectrometry Analysis

In the upcoming sections, sample preparation methods will be given for imaging analysis. However, before imaging the sample, it should be known adsorption performance of stationary phases. To obtain protein adsorption amount, UV-Vis spectrometer was used. By using the UV-Spectrophotometer absorbance values of α-lactalbumin were obtain in different concentrations. At three different protein concentrations, wavelength scan was performed. To obtain a calibration curve of α-lactalbumin, at different concentrations, absorbance values were obtained at a specified wavelength. The final concentration of protein within the Gigacap Q-650M was obtained by using UV-Spectrophotometer (manufacturer is Shimadzu which has the serial number UV-2550) at a specified wavelength.

Adsorption performance of HALO particle is also important. Thus, lysozyme and BSA absorbance values were obtained at different concentration values by using UV-Vis Spectrometer.

HALO particles are novel stationary phases, and binding capacity of HALO for different proteins could not be found in literature. That is why several staining proteins were used to find out the higher adsorption amount over the HALO. Adsorbed protein amount in bulk solution was found by using UV-Vis Spectrometer by using the calibration curves of the proteins.

To investigate adsorption performance of HALO 3.4 μm on Lysozyme, firstly initial protein concentration in HALO -Phosphate buffer solution mixture was measured as 7.93 mg /ml. Mixture has been rotated in each 10 mins for an hour. Meanwhile, to obtain absorbance – concentration calibration curve of Lysozyme, absorbance values of different concentration of Lysozyme were found by using Uv-Vis Spectrophotometer.

Second trial was done with BSA. 50 mg of BSA was mixed with 10 ml PBS and 30 mg HALO particles. Initial protein concentration was 5 mg/ml of BSA. BSA, PBS and HALO mixture was rotated for an hour in each 10 min to increase the adsorption

of protein on HALO particle. The absorbance value of the mixture was measured by using UV-Vis Spectrophotometer.

Lastly, α-lactalbumin adsorption performance was tested on HALO particle. 50 mg of α-lactalbumin was mixed with 10 ml PBS and 30 mg of HALO solution. Mixture was shaken in each 10 min for an hour. The initial concentration of protein was 5 mg/ml. Absorbance value of protein concentration which was the final concentration of protein in bulk solution were obtained. By using the calibration curve of α-lactalbumin, the final concentration of protein was calculated. Detailed findings were stated in section 4 and the calibration curves of proteins were stated in appendix B, C, D, E.

3.3. Sample Preparation Methods

Methods of sample preparation vary depending on the type of imaging. However, for the general point of view, sample preparation methods were summarized below depending on imaging types such as TEM, SEM, and FIB. Several different sample preparation protocols were tested, depending on previously used methods (Kaphingst, Persky, and Lachance 2010) to maximize the contrast and resolution, and obtain good quality images.

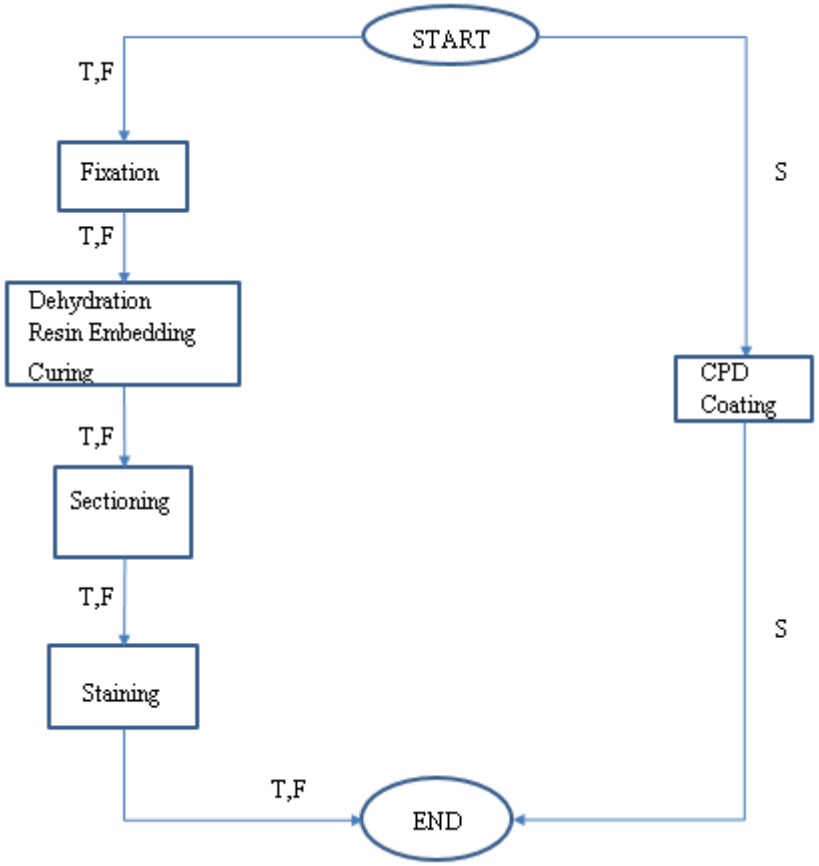

Figure 3.4. Electron microscopy procedure summary. T: TEM imaging, S: SEM imaging, F: Focus Ion Beam imaging

Summary of sample preparation for each electron microscopy technique has been stated in Figure 3.4. Both TEM and FIB sample preparation protocol are identical. For SEM imaging, critical point drier and coating steps were applied if needed. Fixation is the most crucial step for preparative procedure. The specimen has to be immobilized to avoid any changes in ultrastructure. Moreover, fixation should be strong to prevent any negative effects of dehydration and embedding procedures and electron beam. All sample fixation steps were adapted from Glauert et al., 2014 book (Glauert, Audrey M., Lewis 2014) and Hayat (Hayat 1973). Mostly, to fix the specimen, glutaraldehyde and paraformaldehyde mixtures are used. Glutaraldehyde is highly reactive and powerful fixatives of proteins. It stabilizes the structure of the specimen by forming crosslinking. Paraformaldehyde is gentle fixative than glutaraldehyde. The advantage

of using paraformaldehyde is the higher speed of penetration into the specimen. It can fix the specimen by forming methylene cross-bridge between free amino groups on the protein. However, paraformaldehyde can fix the sample temporarily while glutaraldehyde stabilizes the sample more permanently. That is why using the aldehyde mixture includes both would be the proper choice for primary fixation step. Osmium tetroxide (OsO_4) is mainly used as a post-fixative after aldehyde fixation step. It has two main effects on the sample: excellent cellular preservative and heavy metal capable of scattering electrons (Ganguly Bhaskar 2011). It has a high affinity for nitrogenous compounds. It penetrates the specimen so slowly but gives better preservation of structure than other fixatives. Post fixation step follows by dehydration step. After the dehydration step, the embedding step is applied. Mostly, resins are used for embedding material. Embed-812 resin was used in this study. They are chemically inert concerning the samples. They dissolve in dehydrating agents. They should be electron transparent and stable under the electron beam.

3.3.1. Gigacap Q-650M Preparation Method for TEM and FIB Analyses

In this section, the preparation procedure of Gigacap Q-650M will be introduced. Preparation methods for both TEM and FIB are identical. That is why the prepared samples can be used for TEM and FIB imaging analyses. To increase the contrast and resolution of images, proteins were loaded on Gigacap Q-650M. In the upcoming sections, TEM and FIB preparation procedures of Gigacap Q-650M with and without protein loading will be described.

3.3.1.1. Gigacap Q-650M without Adsorbed Protein Preparation Method for TEM

The first trial was done without marking proteins. First, a particle slurry volume of 800µL was measured using Wiretrol calibrated tubes. The sample was washed three times by distilled water and shaken slowly to remove the storage solution ethanol in Gigacap Q-650M. Then, the sample was washed three times by Phosphate buffer solution (PBS) at pH 7. The reason of using buffer is to maintain the pH stable while

fixing the sample. Preparation receipt of PBS was based on Liverpool buffer calculation tool (Calculator for pH buffers 2018). To make 1000 ml of 0.02 M PBS at pH 7, preparation steps were stated below.

Recipe:

- Dissolve 0.0096 mol of acid(KH_2PO_4)
- Dissolve 0.0103 mol of base (K_2HPO_4)
- Make up to 1000 ml with pure water.

1.79 gr of K_2HPO_4 (molecular weight: 174.2 g/mol) and 1.31 gr of KH_2PO_4 (molecular weight: 136.1 g/mol) were mixed and made up to 1000 ml with pure water.

For fixing, embedding, and staining steps, the chemicals were used from Electron Microscopy Sciences. Detailed information is tabulated in Table 3.3.

Table 3.3. *Details of the chemicals used for fixing and embedding*

Chemicals	Manufacturer	Used for	Lot No
Paraformaldehyde 8% Aqueous Solution	Electron Microscopy Science	Pre-fixation	151123
Glutaraldehyde 8% Aqueous Solution	Electron Microscopy Science	Pre-fixation	8150508
Embed 812 RESIN	Electron Microscopy Science	Embedding	150610

Osmium Tetroxide 2%	Electron Microscopy Science	Post Fixation	151216
Lead Citrate,Trihydrate	Electron Microscopy Science	Post Fixation	17810
Uranyless	Electron Microscopy Science	Post Fixation	160907-03
DDSA-Dodecenyl Succinic Anhydride Specially Distilled	Electron Microscopy Science	Embedding	13710
NMA	Electron Microscopy Science	Embedding	150424
DMP-30	Electron Microscopy Science	Accelerator	13600
SeaPlaque GTG Agarose	Lonza	Fixation	0000566893

For TEM and FIB imaging, standard sample preparation methods (Hayat 1973) were used.

In the first fixation step, Glutaraldehyde (8% concentration) and Paraformaldehyde (8% concentration) were used and the final concentration of the aldehyde mixture was 1%. After that; the samples were washed three times by PBS, and then washed three

times by distilled water. The reason for washing by water is to avoid reaction between osmium tetroxide (OsO_4) and PBS. A mass of 1.5 gr. of agarose was added to 50 ml. of distilled water mixture to form a 3 % agarose mixture. Agarose mixture was heated in a microwave oven until the agar dissolved completely in water and then poured into a petri dish. The fixed Gigacap Q-650M particles were embedded into the slightly cooled but still liquid agarose solution, and then the agarose was allowed to gel completely. Then, solid agarose layer was cut into 2 mm strips and placed in small vials. After that they were fixed by OsO_4 for 2 hours. Three times washing by distilled water came next. Since the embedding resin quality is severely affected by even slight moisture, samples were dehydrated by gradually increasing concentration of distilled acetone in water (25%, 50%, 75%, 95%, and 100%). The reason of gradually dehydration of the sample is to avoid any extreme dimensional changes during the dehydration step (Glauert, Audrey M., Lewis 2014). Detailed acetone-water mixture calculations are shown in Table 3.4.

Table 3.4. *Acetone-water mixture amount*

	Acetone(ml)	Water(ml)
25%	1.5	4.5
50%	3	3
75%	4.5	1.5
95%	5.7	0.3
100%	6	0

The dehydration times in acetone were 10-15 minutes each. For the last dehydration step (100% acetone) an unopened bottle of acetone was used. The resin infiltration steps were carried out by a medium hardness formula of Embed 812 resin kit mixture

in increasing ratio. Table 3.5 shows the medium hardness formulation of Embed 812 resin kit.

Table 3.5. *Medium formula of embed 812 resin kit*

	Medium Concentration
Embed 812	20 ml
DDSA	16 ml
NMA	8 ml
DMP-30	0.66-0.88ml

Samples were infiltrated with resin by gradually increasing concentration of Embed 812 in acetone. First, the sample was infiltrated with resin in 25% concentration in acetone. After, infiltrated in 33% concentration of resin. Then the sample was infiltrated in 50% and 66.6%, 75%, and 100% concentration of resin. The last infiltration step by 100% resin concentration were performed using DMP-30(Hardener) Hardener can form cross-linkages between resin monomers. Detailed calculation of resin-acetone mixture is given in Table 3.6.

Table 3.6. *Resin-acetone mixture concentration calculation*

Resin/Solvent Ratio (resin vol %)	Resin(ml)	Acetone(ml)	Infiltration time (hr)
1/3 (25%)	1.5	4.5	1
½ (33.3%)	2	4	1
1/1 (50%)	3	3	1.5
2/1 (66.6%)	4	2	1.5
3/1 (75%)	4.5	1.5	2
100%	6	0	2

When the infiltration step was finished, samples were placed into silicone molds and placed in a fume hood at 65°C for 48 hours for hardening.

Prepared samples for TEM imaging were split approximately 70nm in size by using microtome. Sections were located in 200 mesh formvar-carbon supported copper grids. Whereas some of the samples were imaged without exposing any further staining, some sectioned samples were stained with Uranyless. Samples were imaged by the FEI 120kV HC TEM device in MERLAB, METU.

3.3.1.2. Gigacap Q-650M with Adsorbed Protein Preparation Method for TEM and FIB Analyses

Section 3.3.1.1 has described the sample preparation method for TEM analyses. In this section, sample preparation protocol is the same for both TEM and FIB.

Protein adsorption may enhance the crosslinking between fixatives as well as the functional groups exist in Gigacap Q-650M, and crosslinking may increase the contrast of images. In this section, the preparation method for Gigacap Q-650M with adsorbed protein will be described. Different protein-loaded samples were prepared. α-lactalbumin was used as the marking protein. It is a low molecular weight protein which enables it to Gigacap Q-650M all accessible pores and is negatively charged so it can attach the functional group (quaternary amine) of anion exchanger at pH 7. Firstly, Gigacap Q-650M particle volume of 800μL was measured. The particle suspension was added to 15 ml of 8 mg/ml protein solution. To achieve the adsorption, the adsorbent-protein mixture was rotated in each 10 min for an hour.

Fixing procedures by aldehydes were the same as section 3.3.1.1. Fixed samples were left into the agarose layer, and solidified agarose-sample layers were cut to different sizes. Thicker stripes have approximately 3 mm thickness. The other stripes have the same thickness, which is 1.5 mm. All stripes were put in different vials, and each vials were labeled as A, B, and C having a thickness of 1.5 mm, 1.5 mm, and 3 mm respectively. Then, all the samples were fixed by OsO_4. Dehydration and the embedding steps were the same as section 3.3.1.1. After embedding, samples were left for curing a fume hood at 65°C for 48 hours.

To analyze the effect of the protein adsorbed amount on the contrast of TEM and FIB images, Gigacap Q-650M particles having high protein adsorbed amount were prepared.

The preparation method for 800μl volume of Gigacap Q-650M added to 120 mg protein solution were described above. Then, by changing the volume of Gigacap Q-650M and the protein amount, a new sample solution was prepared.

The volume of Gigacap Q-650M has been changed from 800µL to 400 µL. The sample was washed three times by distilled water, then washed three times by PBS. After that, 130 mg α-lactalbumin was added to 15 ml of PBS solution. Gigacap Q-650M were added in protein-PBS solution. Mixture were shaken for an hour to achieve adsorption of protein on sample (shake it in every 10 min.). After washing step, different fixation and staining protocols were tried according to literature. Fixing by paraformaldehyde and glutaraldehyde were done as mentioned in the previous section 3.3.1.1. Then, washing step with PBS and water came next. The rest steps were different from the previous section (3.3.1.1).

After fixing and washing steps as mentioned above, protein adsorbed sample solutions were put on the agarose layer, and then samples were put in three vials. Each samples in different vials were exposed to the different treatment method.

In the 1st treatment method, after fixing with OsO_4, the sample was washed by distilled water for three times to eliminate any phosphate ions to not react with OsO_4 and to prevent precipitation of Uranyless with phosphate ions. After washing, the sample was fixed by Uranyless-methanol mixture for one hour at room temperature or sample could also be preserved at 4 °C in the dark for 2 hours to prevent precipitation of Uranyless. In previous researches, Uranyl acetate-methanol solution was used as a staining solution (Stempak and Ward 1964). Solubility of uranyl acetate in methanol is higher than that of water or ethanol (Stempak and Ward 1964). That is why to compare the Uranyless-methanol solution staining performance with Uranyl acetate-methanol solution, methanol-Uranyless solution was used for fixing. Then, dehydration and infiltration steps were performed.

In the 2nd treatment, the preparation method was the same as section 3.3.1.1 that consists of OsO_4 fixation step, washing, dehydrating, and embedding steps.

In the 3rd treatment, after OsO_4 fixation and washing step, the sample was stained by only Uranyless for an hour to investigate the differences in between methanol-

Uranyless staining and only Uranyless staining. After staining, the sample preparation protocol follows by dehydrating and embedding steps.

As mentioned in section 3.3, TEM and FIB sample preparation methods were identical. For FIB analyses, only 800µL of Gigacap Q-650M was used after the embedding step. Summary of sample preparation methods for TEM and FIB analyses were given in Figure 3.5.

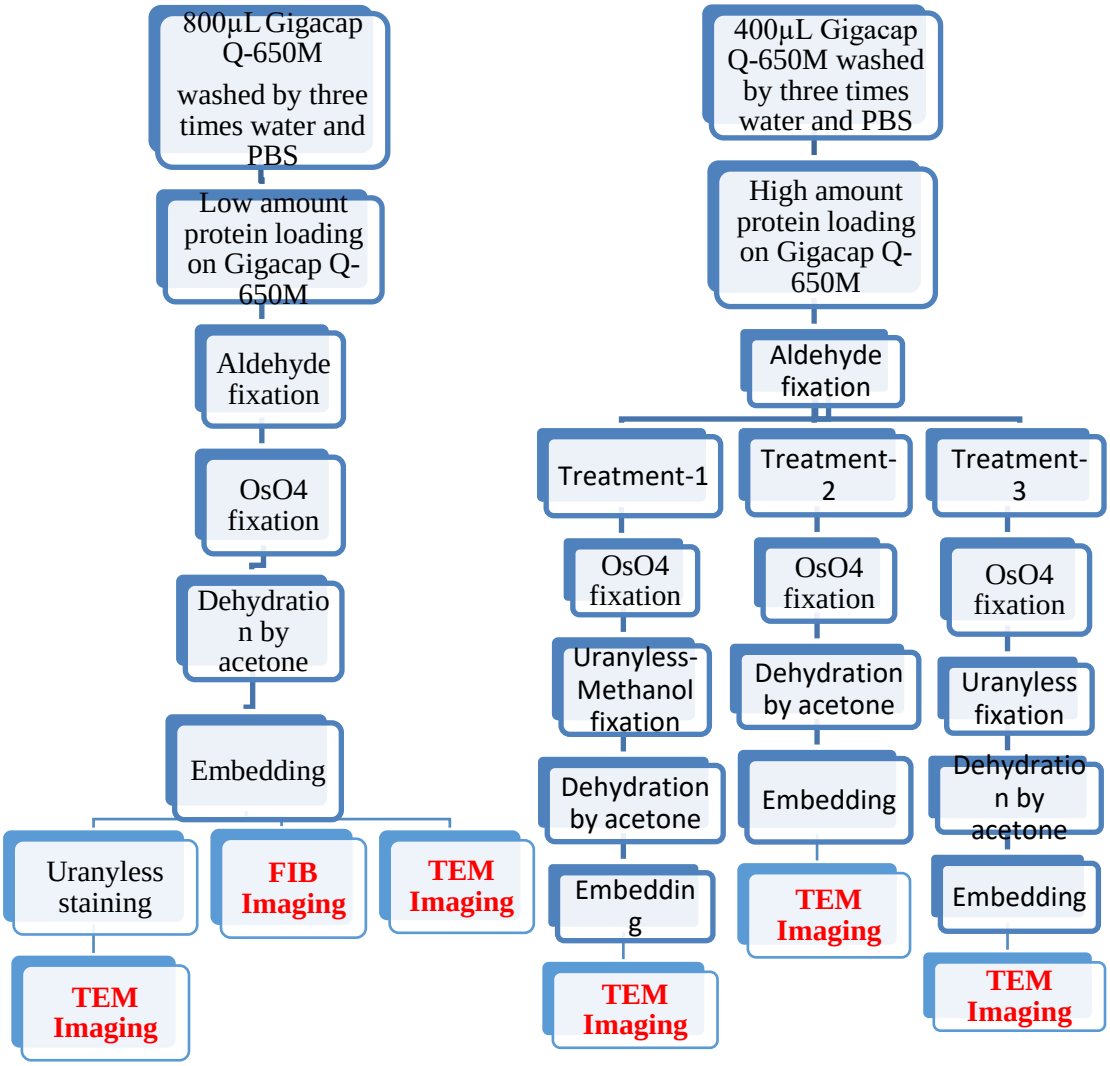

Figure 3.5. Summary of sample preparation method

As seen in Figure 3.5, after embedding step of 800µL of Gigacap Q-650M, the samples were used for FIB and TEM imaging.

Before FIB imaging, previously, by using Leica EM FC6 ultramicrotome, the tip of the embedded sample (800µL Gigacap Q-650M) was cut. Right before imaging, the sample has been covered by a sacrificial protective layer of platinum. Sample was milled with a thickness of 100 nm slices at 5 kV by gallium ions, and then cross-sectional images were taken by SEM at BSE mode in UNAM, Bilkent. Figure of the focused ion beam instrument, FEI Nova NanoLab 600i, placed in UNAM was given in appendix H.

However, some of them were exposed to the Uranyless staining after embedding section.

Uranyless staining method is commonly used for embedded samples. Uranyless staining method was applied according to Electron Microscopy Science protocol. (Electron Microscopy Sciences 2019). 800µL of Gigacap Q-650M having low-adsorbed protein were used for the Uranyless staining technique (Electron Microscopy Sciences 2019). Staining protocol, as described below.

Staining Protocol(Electron Microscopy Sciences 2019)

- One drop of Uranyless was poured onto parafilm
- Hardened resin blocks were cut to 70 nm slices by using Microtome
- Grids were put on Uranyless drop for 1-2 minutes.
- Then, blot the grids on filter paper, washing step by distilled water comes next.
- Finally, samples were dried.

After Uranyless staining, TEM analyses of embedded samples were performed.

Prepared samples for TEM imaging were split approximately 70nm in size by using microtome. Sections were located in 200 mesh formvar-carbon supported copper grids, and some samples were stained by Uranyless. Prepared samples mentioned in

Section 3.3.1, 3.3.2, and 3.3.3 were imaged by the FEI 120kV HC TEM device in MERLAB, METU.

3.3.2. Gigacap Q-650M Preparation Method for SEM Imaging

Sample preparation method is simpler for SEM analyses. Figure 3.2 has shown the preparation method flow chart for TEM and FIB shortly. In this section, Gigacap Q-650M preparation procedure will be introduced for SEM imaging. Accordingly, the Gigacap Q-650M particle volume of 800µL was measured firstly. Then, the sample was washed three times by distilled water and shaken slowly to remove the storage solution ethanol in Gigacap Q-650M. After that, 15 ml of 8 mg/ml protein solution were added to particle suspension then shaken for each 10 min for an hour. No fixation with aldehydes were done. Gigacap Q-650M should be dried first to avoid interference in the SEM vacuum chamber just before imaging.

To improve conductivity and resolution, samples were covered by carbon layer. Then, images were taken. Bilkent UNAM facilities have been used for SEM analyses. Secondary electron mode was used for SEM imaging with the 5 kV of accelerating voltage by using QUANTA 200EF device produced by FEI.

3.3.3. HALO Preparation Method for FIB and TEM Imaging

HALO particle having 3.4 µm and 5 µm diameters from Advanced Materials Technology were used in this study. Specifications of HALO were stated in section 3.1. However, the embedding procedure mentioned below was only applied to the HALO 3.4 µm particle. As a marking protein, α-lactalbumin was chosen. Prepared samples were used for both FIB and TEM analyses.

Firstly, 10 ml of PBS was mixed with 33.6 mg HALO particles. Then, 52 mg of α-lactalbumin was added to the solution. Mixtures were rotated for an hour to enhance the mass transfer of protein. Then, the absorbance value of protein was measured by using UV-Vis Spectrophotometer. After that, by using a material balance equation (detailed calculations were stated in result section), protein concentration in bulk

solution was found. After washing step by water and PBS, the α-lactalbumin-HALO mixture was fixed by 1% concentration of paraformaldehyde and glutaraldehyde mixture. After, samples were washed by PBS, then washed by water by three times. Meanwhile, 3% Agarose solution was prepared. Heated agarose was poured in petri dish, and then fixed samples were put on the agarose layer. After that, samples were cut to 2-3 mm slices, and they were put into three different vials. Since three different treatment methods will be used to increase the contrast of samples. Each sample was fixed by 2% OsO_4 and had been waiting for a night.

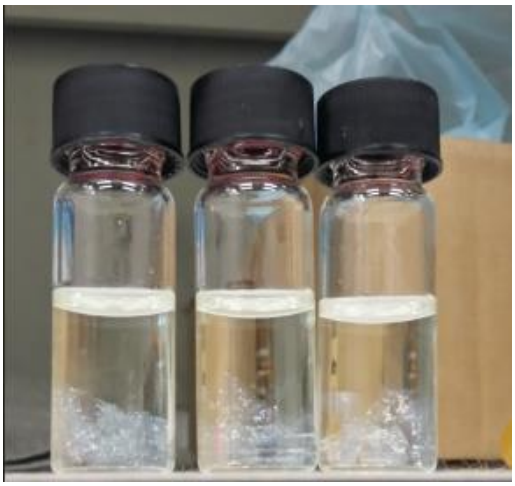

Figure 3.6. HALO particles in agarose appearances after OsO_4 fixation

After fixation, sample appearances are shown in Figure 3.6. After OsO_4 fixation, different staining protocols were performed. Figure 3.7 illustrates the summary of the preparation steps.

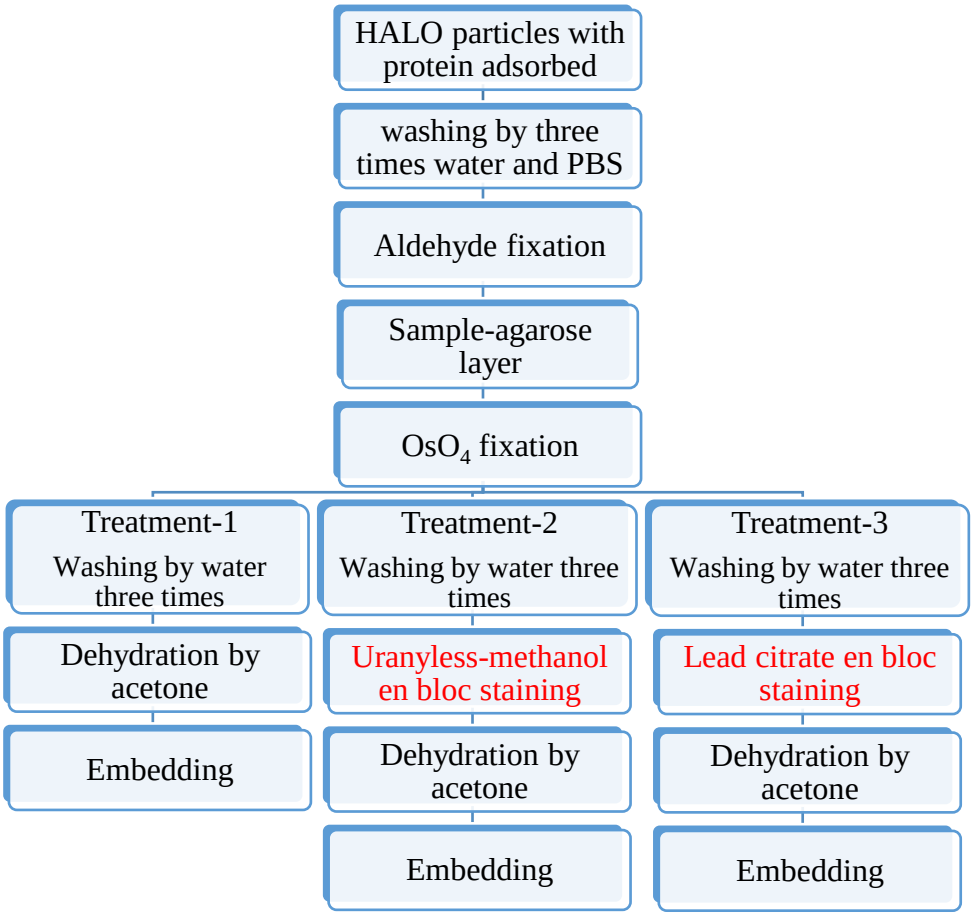

Figure 3.7. Summary chart of HALO sample preparation method for FIB

For the sample placed into vial-1, standard protocol was followed, as mentioned in section 3.3.1. After OsO_4 fixation, the sample was washed three times by water, and then, dehydration step was performed. Lastly embedding step was followed. These sequences were written as 'Treatment-1' in Figure 3.7

For the sample in vial-2, after washing step by water, en-bloc staining was performed by Uranyless-methanol mixture. 6 ml Uranyless was mixed by 2 ml of methanol. Let the sample wait in Uranyless-methanol solution for two hours. This method was mentioned in Figure 3.7 as 'Treatment-2'.

The sample placed into vial-3 were fixed by lead citrate for two hours after washing step by water. Besides Uranyless or uranyl acetate, lead citrate is also common staining material used in electron microscopy. To make 10 ml of stain, it was weighted out 0.034 gr of lead citrate, added it to 10 ml of distilled water, then drop in 0.1 ml of 10 N NaOH. The solution was shaken approximately 5 min to dissolve lead citrate (Leica Microsystems 2013).

After performing different en-bloc staining and fixing method, each sample was washed by distilled water three times. Samples were dehydrated by acetone after that according to protocol stated in section 3.3.1. After dehydration, the infiltration step was performed by using Embed-812 Resin. Resin preparation method was described in section 3.3.1. Then, Samples were placed into silicone flat molds, and samples were left in a fume hood at 65°C for 48 hours for hardening.

Embedded samples will be imaged by using FIB and TEM. HALO particles can also be imaged without embedding. However, to obtain high-quality images, embedding sample preparation protocol was chosen.

The imaging of two different kinds of samples was carried out using FIB: The first sample had HALO particles embedded in resin as was done previously described above, and the second had free particles placed on an adhesive surface. For the embedded samples, first, the embedded samples were trimmed and faced using the Leica EM FC6 ultramicrotome at UNAM, Bilkent as shown in appendix i.

Samples were put on aluminum stub for coating. Stub images were shown in Figure 3.8. Then, they were covered with Pd-Au by forming plasma by using Argon gas. Thickness of Pd-Au layer was approximately 30nm. The figure of coating device was given in appendix j.

Figure 3.8. Aluminum stub used for coating

Additionally, HALO particles which were not embedded in resin were coated by Pd-Au layer. Leica EM ACE200 instrument was used for coating in the Central Chemical Engineering Laboratory, METU.

HALO particles have been coated approximately 10nm thickness for 125 s. Coating instrument is illustrated in appendix K.

HALO particles having a diameter of 3.4 and 5 μm were imaged by using the TESCAN GAIA3 Triglav^{TM} instrument in HUNITEK, Hacettepe University as given in appendix H.

FIB images results of both embedded and free HALO will be given in section 4.3.2.

For TEM imaging, embedded samples which were treated by lead citrate (treatment-3) were trimmed approximately 90 nm in size by using microtome. Sections were located in 300 mesh formvar-carbon supported copper grids. After that, TEM imaging was performed.

3.3.4. HALO Preparation Method for SEM Imaging

For SEM analyses, HALO was not fixed or embedded in resin. Besides, the particles were used as it is. Two types of HALO particles were imaged which have different diameters which are 3.4μm and 5 μm. Firstly, particles were placed on stub as seen

Figure 3.9. Then, HALO particles have been covered by Pd-Au alloy approximately 6 nm to increase the conductivity by using Polaron Range Sputter Coater device in MERLAB, METU. Sputter coater device was given in appendix J.

Figure 3.9. HALO particles for SEM imaging

Edward Oil Mist Filter EMF10 has been worked at 7 pascal.

Images were taken by a Quanta FEG 400 device produced by FEI. Secondary electron mode was used with the accelerating voltage from 10 kV to 30kV.

CHAPTER 4

RESULTS AND DISCUSSIONS

4.1. Calculation of Adsorbed Amount of Staining Proteins

Before obtaining the calibration curve of α-lactalbumin, the maximum absorbance value was found by doing a wavelength scan at different protein concentrations. Maximum absorbance value was obtained at 280 nm. Detailed wavelength scan figure is shown in appendix-a section. Calibration curve of α-lactalbumin was obtained by using absorbance and concentration values at 280 nm. In different concentration of α-lactalbumin, absorbance values were obtained by using UV-Visible Spectrometer. Tabulated results are shown in Table 4.1.

Table 4.1. *Absorbance vs. concentration values of α-lactalbumin at 280 nm*

Concentration (mg/ml)	Absorbance
0.25	0.44
0.5	0.93
1	1.82

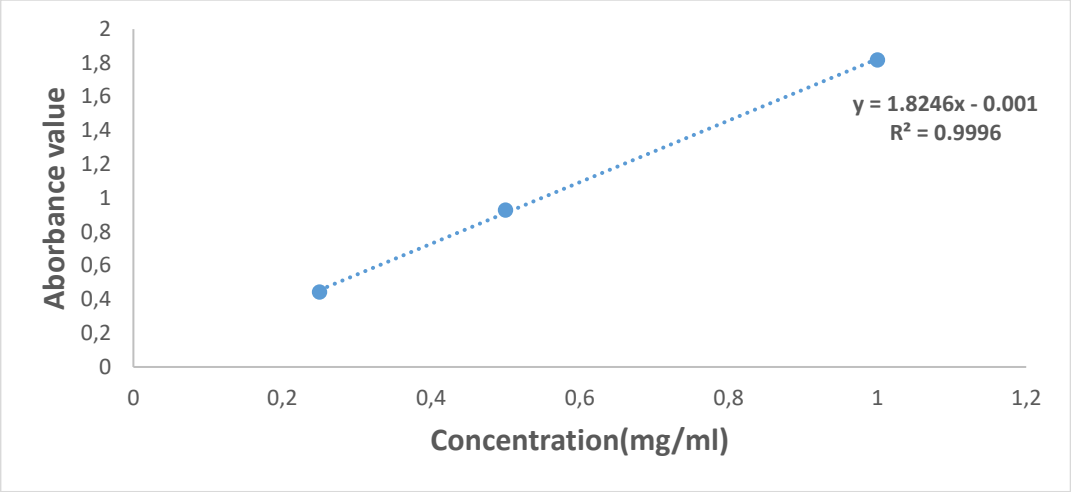

Figure 4.1. Calibration curve of α-lactalbumin at 280nm.

By using the obtained calibration curve, which was illustrated in Figure 4.1. α-lactalbumin adsorbed amount of protein was found for both 400 and 800µl of Gigacap Q-650M.

The initial protein concentration was 8 mg/ml in 800µL of Gigacap Q-650M.

$C_{initial,protein}$=8 mg/ml

$C_{final,protein}$=4.92 mg/ml

$$Q=\frac{V}{Vads}(C_{initial,protein}-C_{final,protein}) \quad (4.1.1)$$

V is the volume of the bulk solution, V_{ads} is the volume of the particle suspension. C initial and final indicates the protein concentration at the final and initial state. By using equation 4.1.1, adsorbed protein amount found as 57.8 mg/ml was found.

The initial concentration of protein in solution was 8.7mg/ml in 400µl of Gigacap Q-650M. The final concentration of protein within the particle was found by using UV-Vis Spectrophotometer at 280 nm. By applying material balance on the bulk solution, adsorbed protein amount by particle were found by using equation 4.1.1.

$C_{i,protein}$=8.7 mg/ml

$C_{f,protein}$=3.36 mg/ml

It was found that 97.1 mg of protein adsorbed by Gigacap Q-650M. Low (57.8 mg/ml) and high (97.1 mg/ml) protein adsorbed Gigacap Q-650M was imaged.

For HALO particles, three types of protein which were BSA, lysozyme, and α-lactalbumin were investigated according to adsorption performance. For each protein wavelength scan was performed to investigate the maximum absorbance value could be obtained at which wavelength. It was found that maximum absorbance value for lysozyme and BSA was obtained at 280nm. Detailed wavelength scan results are attached in appendix B, and D.

To obtain the calibration curve of lysozyme, absorbance values of lysozyme at different concentrations were obtained and are listed in Table 4.2. Then, the calibration curve of lysozyme was obtained and is displayed in appendix B, C, and F.

Table 4.2. *Concentration vs. absorbance value of lysozyme at 280 nm*

Concentration of Lyzosyme (mg/ml)	Absorbance Values
0.25	0.408
0.5	0.801
0.75	1.168
1.0	1.523

By using the calibration curve of lysozyme, final protein concentration was found 8.01 mg/ml.

$C_{i,protein}$=7.93 mg/ml

$C_{f,protein}$=8.01 mg/ml

According to calculations, final concentration has been found greater than the initial concentration of lysozyme. However, there are small differences between them. Small

deviation may come from the experimental error. That is why it can be concluded that no adsorption was seen when using lysozyme as staining protein. Final and the initial protein concentrations were very similar to each other. Lysozyme adsorption kinetics on the hydrophobic surface are invariant with pH (van der Veen, Stuart, and Norde 2007). That is why the net charge of lysozyme does not affect the adsorption on hydrophobic surface. It can be concluded that hydrophobic interaction is the major driving force for protein adsorption at the hydrophobic surface (van der Veen, Stuart, and Norde 2007). Maybe adsorption did not occur because of the lack of hydrophobic interaction between HALO and lysozyme. Hence, lysozyme was not a proper choice for staining protein.

At different concentrations, BSA absorbance values were obtained by using a UV-Vis spectrometer. Tabulated results are in Table 4.3.

Table 4.3. *Absorbance values of BSA at different concentrations at 280 nm*

Concentration	Absorbance Value
0.05	0.041
0.25	0.150
0.5	0.415

It was found that the final concentration of BSA in the bulk solution was 3.9 mg/ml

$C_{i,protein}$= 5 mg/ml

$C_{f,protein}$=3.9 mg/ml

Lastly, α-lactalbumin adsorption amount on the HALO particle was calculated by using the calibration curve of α-lactalbumin in Figure 4.1.

$C_{i,protein}$=7.93 mg/ml

$C_{f,protein}$=3.78 mg/ml

Summary of the experimental results are shown in Table 4.4.

Table 4.4. *Adsorption amount of proteins on stationary phases at pH 7*

Stationary Phase	Staining Protein	Initial concentration (mg/ml)	Final Concentration (mg/ml)	Adsorbed amount of protein
800 µL of Gigacap Q-650M	α-lactalbumin	8.0	4.92	57.8 mg/ml
400 µL of Gigacap Q-650M	α-lactalbumin	8.70	3.36	97.1mg/ml
HALO	α-lactalbumin	7.93	3.78	2306 mg/ml*
HALO	BSA	5.0	3.9	611 mg/ml*
HALO	Lysozyme	7.93	8.0	0

*Calculations were stated in appendix N because of the nonsense results.

According to tabulated results in Table 4.4, BSA and α-lactalbumin adsorbed to HALO particles were calculated 2306 and 611 mg/ml. These results seem that they are not realistic.

HALO particles have hydrophobic interaction. Protein absorption is driven by the attraction of the non-polar parts of BSA molecules toward the surface on the hydrophobic surface, which is HALO. However, according to research done by Jeyachandran et al. 2009, the BSA molecules adsorb to the hydrophilic surface with more significant interaction strength than to the hydrophobic surface (Jeyachandran et al. 2009). Thus, it was decided to use α-lactalbumin as the staining protein.

5.2 mg/ml of α-lactalbumin was present in a bulk solution. Then, by using the UV-Vis spectrometer, and calibration curve, the final concentration of α-lactalbumin was found as 2.86 mg/ml. Microstructure analyses of HALO particles with adsorbed α-lactalbumin will be given in section 4.3.

4.2. Microstructure Analyses of Gigacap Q-650M by Electron Microscopy Techniques

Several imaging techniques and the staining treatments will be evaluated in this section. Summary of imaging techniques and treatment types are summarized in Table

4.5. In the following sections, imaging run numbers will be used to refer to the corresponding imaging experiments.

Table 4.5. Performed imaging techniques and applied treatments

Imaging Run	Imaged Material	Imaging Method/Mode	Sample Preparation Treatment
1	Gigacap Q-650M	TEM	only fixation
2	Gigacap Q-650M	TEM	57.8 mg Protein loading
3	Gigacap Q-650M	TEM	57.8 mg Protein loading and Uranyless Post Staining
4	Gigacap Q-650M	TEM	97.1 mg Protein loading and applied Uranyless-methanol en bloc staining
5	Gigacap Q-650M	TEM	97.1 mg Protein loading
6	Gigacap Q-650M	TEM	97.1 mg Protein loading and applied Uranyless en bloc staining
7	Gigacap Q-650M	SEM/BSE	97.1 mg Protein loading and without applying any fixation
8	Gigacap Q-650M	FIB-SEM/BSE	57.75 mg Protein loading

In total, eight imaging runs were performed. To obtain better resolution and microstructure analyses, TEM techniques were used. SEM analyses were done to understand the morphology of Gigacap Q-650M. Lastly, FIB-SEM combination technique was used to reconstruct the sample structure by using 2-D images. However, FIB results were not satisfactory concerning contrast and resolution.

4.2.1. TEM Analyses of Gigacap Q-650M Structure

Gigacap Q-650M samples with and without protein loading were imaged in this part of the study. Gigacap Q-650M has functional groups. Fixative and sample functional groups can form crosslinking, which can provide contrast even when protein is not present (Glauert, Audrey M., Lewis 2014). Thus, for the first trial, protein was not used. Sample without protein-loaded blocks were sectioned at 55-65 nm thickness by

microtome (Image run-1 in Table 4.5). These sections were placed on 200 mesh formvar-carbon supported copper grids. Digital images were taken by using FEI 120kV HC TEM device. Image is shown in Figure 4.2.

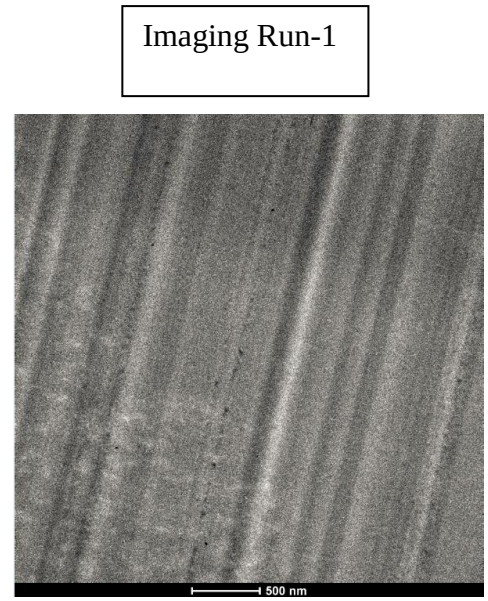

Figure 4.2. TEM images of Gigacap-Q650M without protein loading

As seen from Figure 4.2, no contrast was obtained in image run-1. Aldehydes used for fixatives react with Q-amine moieties exist in Gigacap Q-650M, and they form cross-linking. Besides, osmium tetroxide improves the contrast. It acts as a fixative as well as a promoter of contrast during post-staining (Pandithage 2013). Therefore, the first imaging run was done without using proteins. Probably, Q-amine moieties were not dense enough to get high contrast.

To improve contrast, Gigacap Q-650M was loaded with protein (α-lactalbumin), then fixed, embedded, and imaged. The adsorbed protein concentration was found as 57.8 mg/ml in the particles. No post-staining was applied. There were three types of samples labeled as A, B, and C as mentioned in section 3.3.1.2. However, when imaged, there were no contrast of samples A, and B. Either no staining or non-proper sectioning of samples may lead the poor resolution. Sample number C was the thicker one. Compared to the other samples, the contrast of sample C was better. It may be

because of the higher OsO4 penetration on sample clumps. Images are shown in Figure 4.3.

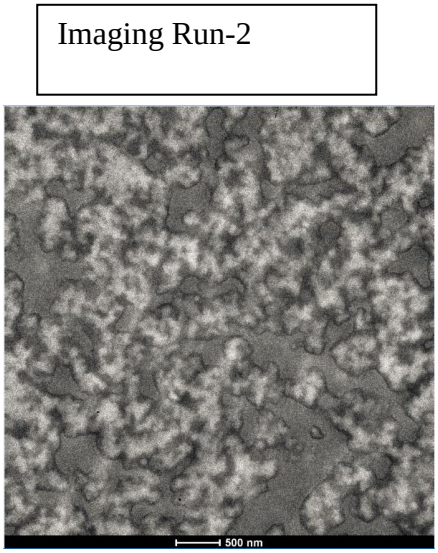

Figure 4.3. TEM images of α-lactalbumin adsorbed (57.8 mg/ml) Gigacap Q-650M (Scale bar: 500 nm)

It was seen that dark regions over the surface of pores show protein localization. Lighter phase seems as solids. It can be concluded that adsorbed proteins were placed around the surface of pores, and they could not penetrate the solid. Although knowledge of chemical reaction of staining is still limited or absent for many stains (Belazi et al. 2009), the reason of obtaining more contrast compared to image run-1 may be the functional groups of Gigacap Q-650M bind the protein. As a result of it, protein and functional groups exist in Gigacap Q-650M form the crosslinking. The presence of protein probably resulted in more extensive crosslinking and staining. It has also been introduced that osmium tetroxide simply attaches to aliphatic side chains and proteins by hydrogen bonds in the tissue (Belazi et al. 2009). Therefore, OsO_4 may react with the α-lactalbumin by hydrogen bonds and provides rise to strong electron scattering from electron donor ligands. As a result of this, the contrast is increased.

To increase the contrast level of sample C more, post-fixation by Uranyless was applied on the grids just before imaging the sample (image run-3).

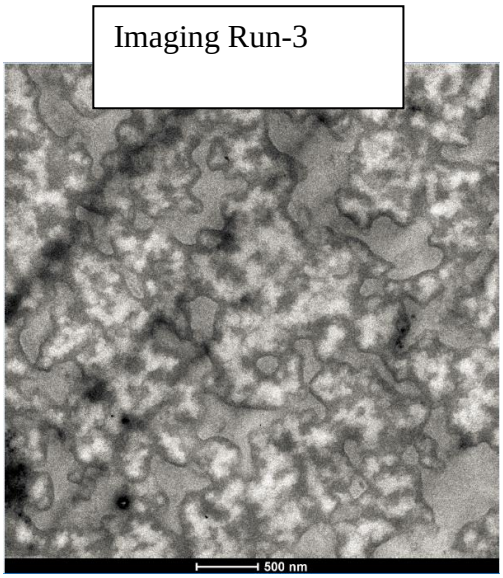

Figure 4.4. TEM images of Uranyless stained and protein loaded Gigacap-Q650M

UranyLess is a proprietary mix of multiple lanthanides, and it is ready to use aqueous solution (Electron Microscopy Sciences 2019). It has a higher affinity for biological material. UranyLess staining solution is ideal for ultra-fine sections. It was seen that Uranyless post staining (staining of sectioned sample) have worked on contrast. Protein localization corresponds to seen as darker areas near the edges of pores as seen from Figure 4.4. Besides, there are dark spots on the images; perhaps these are because of the non-homogeneous staining by Uranyless.

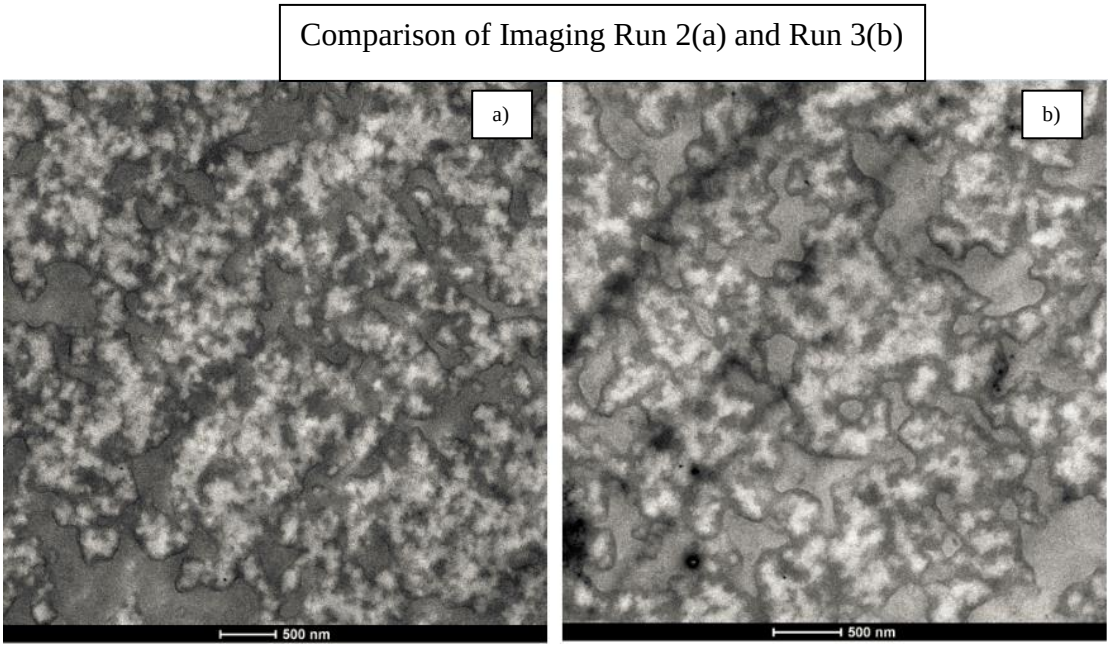

Figure 4.5. TEM images of adsorbed protein (α-lactalbumin) Gigacap-Q650M samples with post-stained (b) and without post- stained (a)

Figure 4.5.b illustrates that staining protocol (Image run 3) enhanced contrast slightly better than the sample without post-stained (Figure 4.5.a). It was seen that dark layers and accumulated dark regions on stained samples because of the Uranyless.

Protein loaded sample number C were sectioned about 70 nm in size. Some sectioned samples were imaged without staining, whereas some of them were imaged after post staining by Uranyless. TEM images are shown in Figure 4.6.

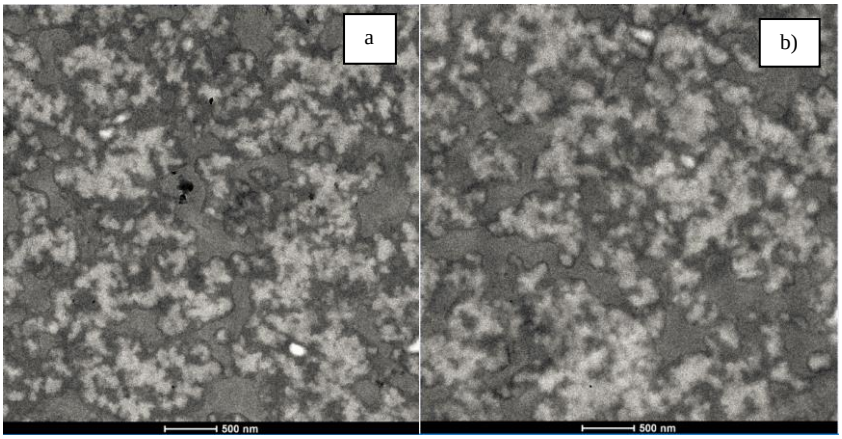

Figure 4.6. TEM imaging of post-stained (a) and unstained (b) samples 70 nm in size.

Some stained parts were seen in Figure 4.6.a as dark spots. Since Uranyless binds the proteins more, it gives darker appearances locally. Samples which are applied post staining by Uranyless (Figure 4.6.a) have higher contrast than the sample without applied post staining (Figure 4.6.b). Better contrast may be obtained by loading more protein on adsorbent. Thus, protein loading amount was increased to see the effects on contrast.

To obtain TEM images having higher contrast, protein loading amount was increased from 57.8 mg/ml to 97.1 mg/ml. Moreover, TEM sample preparation methods were changed to see the effects of fixation methods on TEM images.

After OsO_4 fixation, Uranyless-methanol fixation step was performed to understand the effect of fixation methods on contrast. TEM images are shown in Figure 4.7 (image run- 4).

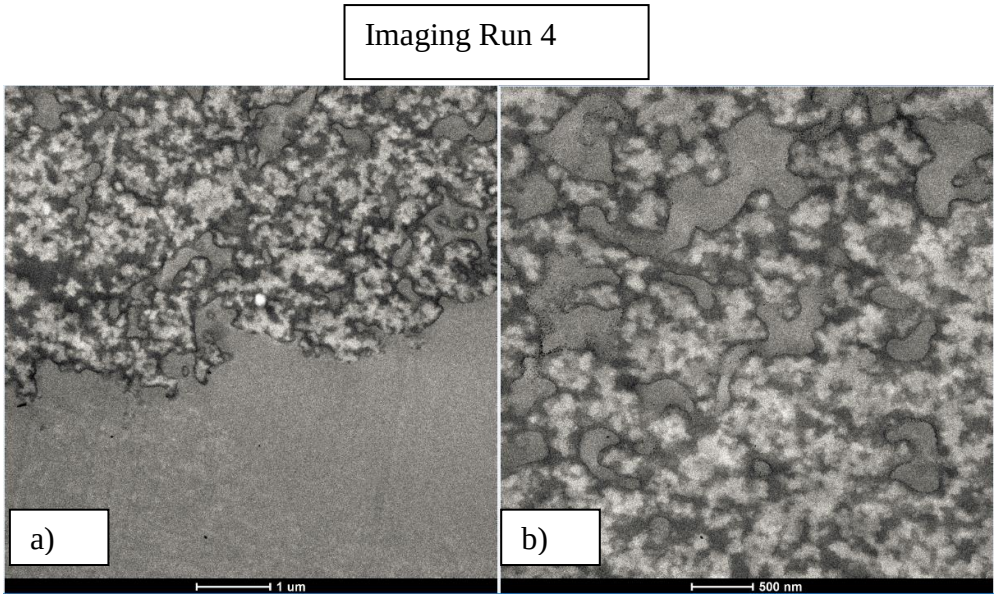

Figure 4.7. TEM images of Gigacap-Q650M (97.1mg/ml protein loaded) Uranyless-methanol mixture for en bloc staining method at different magnifications

Figure 4.7.a shows Gigacap Q-650M image at 1µm magnification, whereas images were taken at 500 nm magnification in Figure 4.7.b. It was seen that by using Uranyless-methanol en-bloc fixation method, more contrast had been obtained. The contrast enhancement observed in the sample is mainly due to the high affinity of Uranyless for proteins, and hydroxyl groups in Gigacap Q-650M. By using en bloc staining with Uranyless-methanol mixture, without necessity to further post staining, samples could be ready directly to the TEM imaging. However, it should be noted that more protein loading gives high contrast. Since proteins are attached to the functional group of Gigacap Q-650 M, and it is visible in Figure 4.7, proteins were located along the pores of the ion exchanger.

The second sample was prepared by using the protocol mentioned in section 3.3. The procedure was followed by using only OsO_4 fixation after aldehyde prefixation. After increasing protein loading amount by Gigacap Q-650M from 57.75 mg/ml to 97.1 mg/ml obtained TEM images (image run-5) had high contrast, and higher resolution compared to sample having low protein loading. It was understood from the images, proteins were seen over the edges of Gigacap Q-650M. When protein loading was high, crosslink formation between Q-amine moieties and protein were increasing.

Lighter phases were solids, and darker phases have been shown adsorbed proteins and Gigacap Q-650M sample.

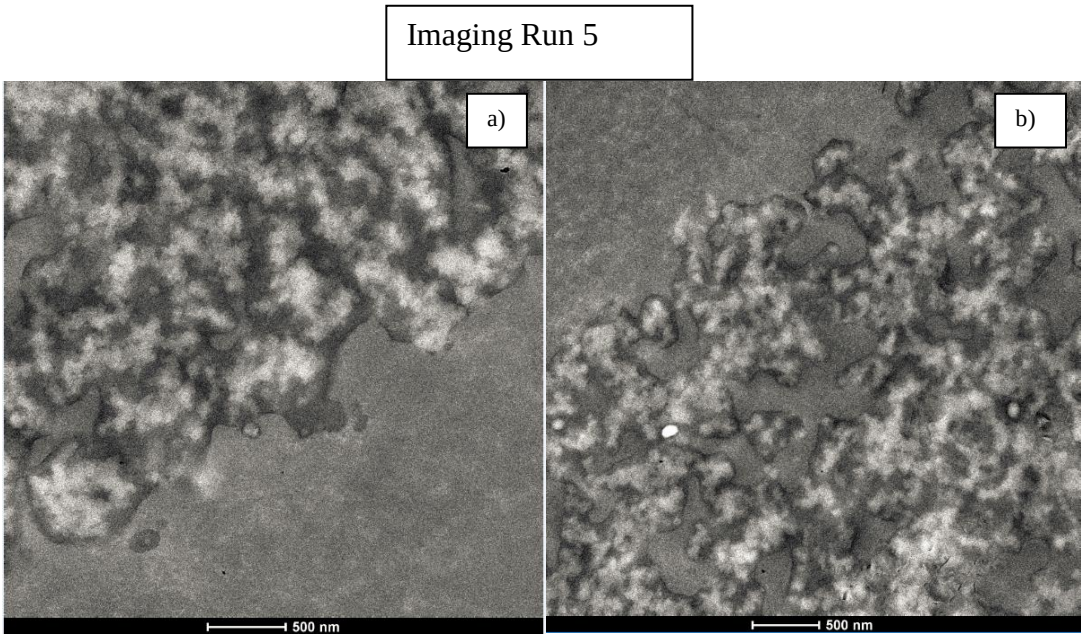

Figure 4.8. Comparison of the TEM images of Gigacap-Q650M samples with 57.8 mg/ml (a) and 97.1 mg/ml (b) adsorbed protein

It can be concluded that, protein locations over the edge of Gigacap Q-650M (Figure 4.8.b) provided more contrast compared to less adsorbed protein of Gigacap-Q650M. Because of the protein localization over the porous layer of ion exchange resin, the light phase appears smaller compared to Figure 4.8.a. Most voids were covered by the protein.

Other imaged Gigacap-Q650M were prepared by using only Uranyless after OsO_4 fixation.

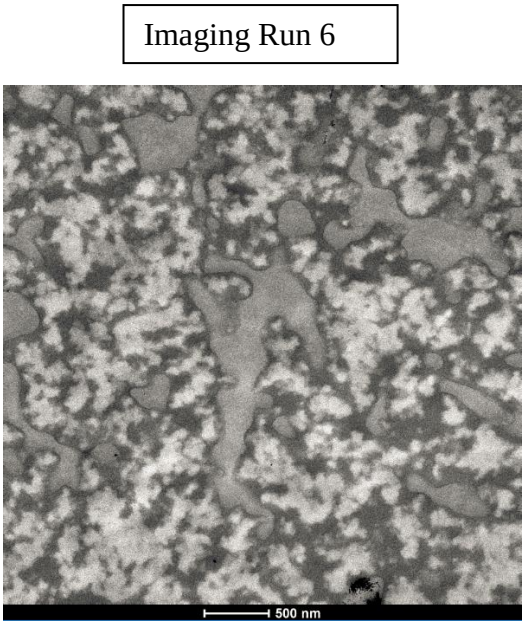

Figure 4.9. Representative example obtained for Uranyless en bloc staining method

Uranyless produces high image contrast (image run-6) and electron density, as stated in Figure 4.9. Moreover, Proteins were bound by the Uranyless, and it results in higher contrast that one can get.

To get a better idea about the effects of different staining methods on image contrast of TEM, comparison of images having different staining method are illustrated in Figure 4.10.

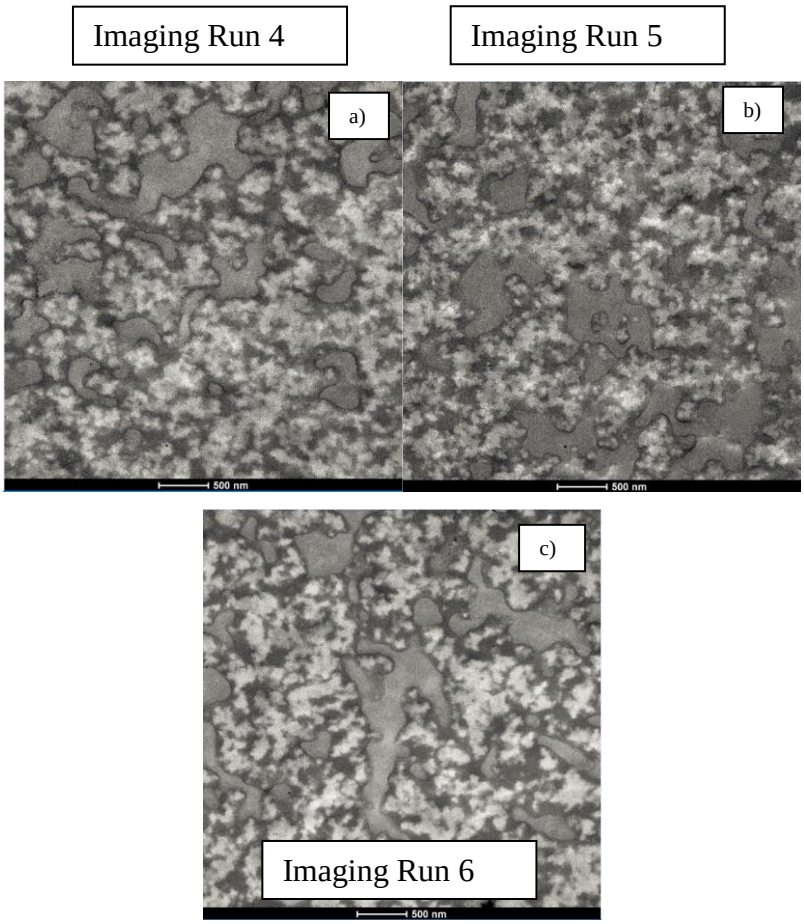

Figure 4.10. Comparison of TEM images of Gigacap-Q650M prepared by different fixation method (a) prepared by Uranyless-methanol mixture en bloc staining method; b) prepared by only OsO_4 fixation; c)Uranyless en bloc staining used

Research shows that after aldehyde fixation step, fixing with osmium tetraoxide followed by Uranyl acetate provides better contrast (Glauert, Audrey M., Lewis 2014). Using the uranyl acetate solution with methanol increases the penetration into samples (Stempak and Ward 1964). To observe the effects of fixation methods on contrast, both methods were used. Uranyless (instead of Uranyl Acetate)-methanol mixture was used for en bloc staining to prepare the first sample (image run-4) which is shown in Figure 4.10.a. However, the last sample (Figure 4.10.c) was prepared by using Uranyless instead of using Uranyless-Methanol mixture for en bloc staining method. Other sample (Figure 4.10.b) was prepared by applying the default protocol mentioned in section 3.3.1. Uranyless may allow deeper penetration by using methanol into the

sample. Denser staining of certain components may occur. However, the sample image obtained by using the en-bloc staining method with only Uranyless (image run-6) has more contrast compared to the image prepared by Uranyless-methanol mixture (image run-5). It was seen that the addition of methanol into the Uranyless solution had no positive effect on contrast. Maybe there was not enough time to penetrate the sample, or methanol concentration within the Uranyless solution was not enough to obtain more contrast. TEM image contrast of sample which has been exposed to only OsO_4 (image run-4) is lower than the sample images exposed to Uranyless en- bloc staining (image run-6). Uranyless has the advantage of producing higher electron density and binds to α-lactalbumin proteins. As a result of this, contrast increased. While comparing the methods which are en-bloc staining protocol using Uranyless-methanol (image run-5) mixture and OsO_4 post-fixation (image run-4) only, it can be said that more contrast was achieved when used Uranyless-methanol en-bloc staining method.

To investigate the effect of en-bloc staining and post staining by using Uranyless on contrast, a comparison of these methods was illustrated in Figure 4.11.

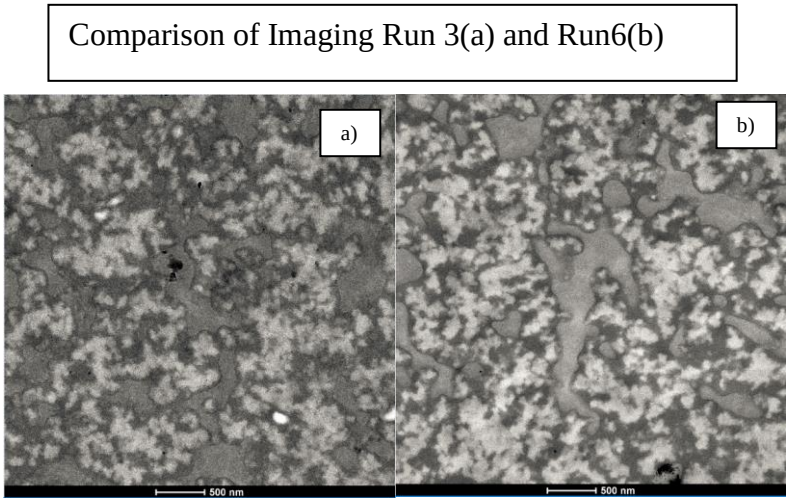

Figure 4.11. Comparison of post staining (a) and en bloc staining (b) method by using Uranyless on Gigacap-Q650M sample

It is seen in Figure 4.11; contrast is better using the en-bloc staining method shown in Figure 4.11.b rather than using the post staining method illustrated in Figure 4.11.a. Gigacap Q-650M structure is clearer in Figure 4.11.b. However, it may be due to the protein loading application for staining or method differences. Gigacap Q-650M samples were adsorbed 97.1 mg/ml of protein while applying en-bloc staining method by Uranyless. In image run-3(Figure 4.11.a), the adsorbed protein amount was 57.8 mg/ml. Because of the increasing of adsorbed protein on Gigacap Q-650M, the contrast of the image may be higher concerning the post staining method. Normally, the post staining method is more effective than en-bloc staining method. But in this case, it seems that en-bloc staining method together with increasing protein amount is useful to get higher contrast.

Koku,2011 studied Gigacap S-650M and Toyopearl SP-650M (Koku 2011). Both resins have the same base matrix being methacrylate. However, while Toyopearl SP-650M is a traditional ion exchanger, Gigacap S-650M is the polymer-modified resin. Figure 4.12 shows the TEM images of Gigacap S-650M and Toyopearl SP-650M which are cation exchangers, and of Gigacap Q-650M, which is anion exchanger. Gigacap S-650M and Gigacap Q-650M have similar properties. However, while Gigacap Q-650M is anion exchanger, Gigacap S-650M is cation exchanger.

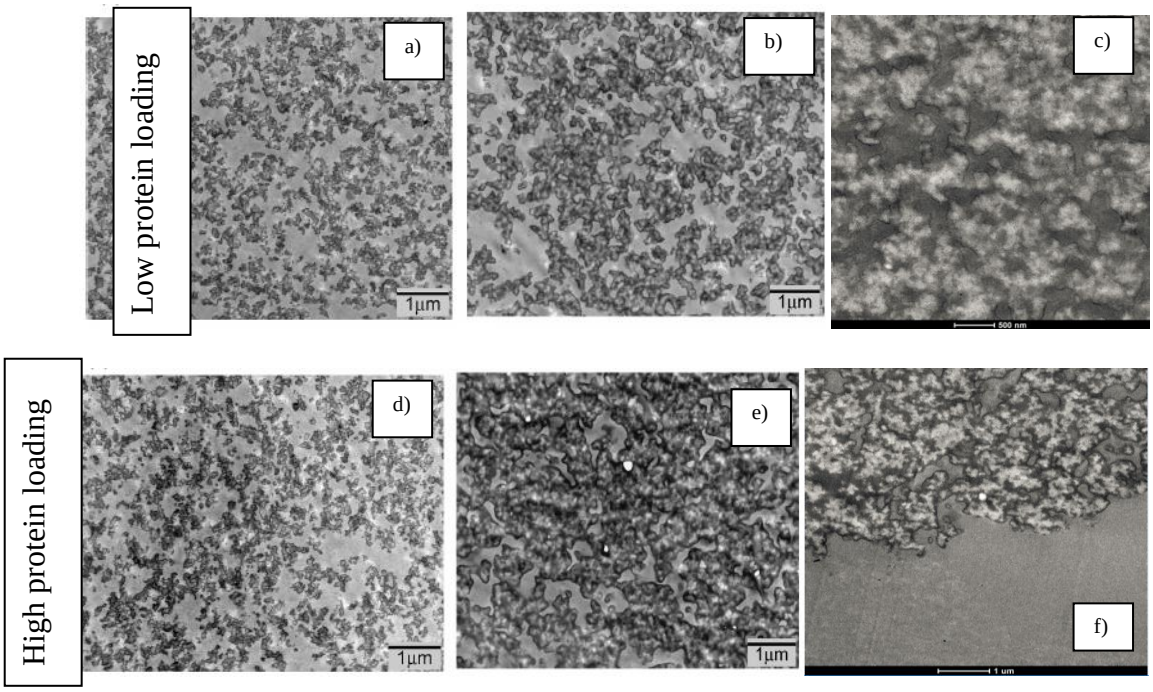

Figure 4.12. Sample TEM images of Toyopearl SP-650M, GigaCap S-650M, and Gigacap Q-650M sections at low (a,b,c) and high (d,e,f) protein loadings. (a) SP-650M, low protein load, final concentration in particles 33 mg/ml(b) GigaCap S-650M, low load, concentration 83 mg/ml (c) Gigacap Q-650M, low load, concentration 57.8 mg/ml(d) SP-650M, high load, 58 mg/ml (e) GigaCap S-650M, high load, 211mg/ml (f) Gigacap Q-650M, high load, 97.1 mg/ml.

While comparing the structures according to Figure 4.12, all ion exchangers have similar structural characteristics due to having the same base matrix. However, Gigacap S-650M, which is the polymer-modified resin of traditional SP-650M, have a secondary polymeric phase, and it binds the protein more. As a result of this, pores of Gigacap S-650M covered by proteins more. Koku, 2011 has observed fully dark regions for solids. It may be due to the more protein adsorbed on resin (high load: 211 mg/ml) or better staining. Loading more protein to the resins results in more contrast as seen Figure 4.12.e. The situation confirms the dynamic binding capacities of both resins (Gigacap S-650M binding capacities:150 g/L for human immunoglobulin G, Toyopearl SP-650M binding capacities:50g/L for lysozyme) (Tosoh Bioscience LLC. 2019). For high protein load of Gigacap Q-650M and Gigacap S-650M, it seems that

proteins have covered the pores of Gigacap S-650M mostly than Gigacap Q-650M. It is because of the adsorption of protein is higher than Gigacap Q-650M.

4.2.2. SEM Analyses of Gigacap Q-650M Structure

Firstly, SEM images of Gigacap Q-650M were captured in secondary electron mode with a voltage of 5 kV. All images were taken by UNAM, BİLKENT. All images refer to imaging run-7 in Table 4.5.

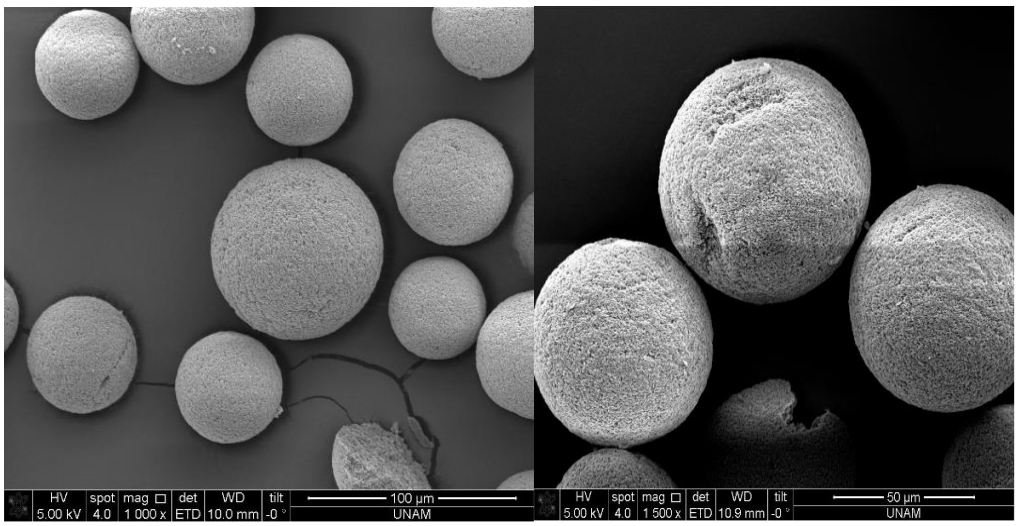

Figure 4.13. Gigacap Q-650M SEM images by having lower magnification (which are 1000x –left image & 1500x-righ image).

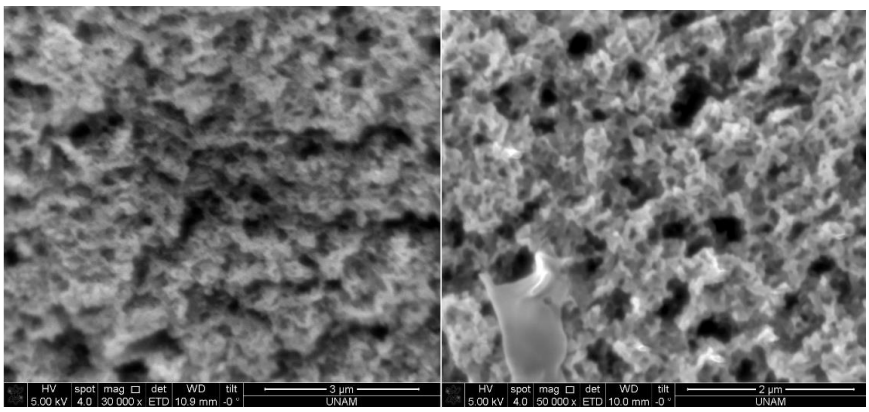

Figure 4.14. Obtained SEM images of Gigacap Q-650M particles at increased magnification left: 30.000x, Right: 50.000x

The images show the fibrous nature of Gigacap Q-650M. Figure 4.13 displays the Gigacap Q-650M images by using lower magnification, whereas Figure 4.14 shows images taken by using higher magnifications. Polymer features can be shown better by taking high magnification images. Secondary electron mode in SEM analyses generates contrast by the help of releasing secondary electrons over the surface. Images formed by using the SE mode are highly dependent on structural or geometry properties. Therefore, topography and the atomic composition of the specimen can be determined by the amount of secondary electrons (Koku 2011). Better images can be captured by increasing beam voltage; however it may result in radiation damage leading to irreversible breakdown of structural property. Besides, imaged samples were air-dried instead of using critical point drier apparatus. Since microporous specimen capsules for sample storage did not exist, therefore, critical point drier could not be used just before SEM analyses. However, water evaporation may cause artifacts resulting from surface tension effects in dried samples by air (Koku 2011). Maybe, it affects the structure of the sample, and accurate structure may obtain if critical point drier would be used.

Bowes and his colleagues, 2009 have also investigated the structure of SP Sepharose XL dextran modified particles whereas in the present research Gigacap Q-650M was used. SP Sepharose XL is a cation exchanger, whereas Gigacap Q-650M is anion exchanger.

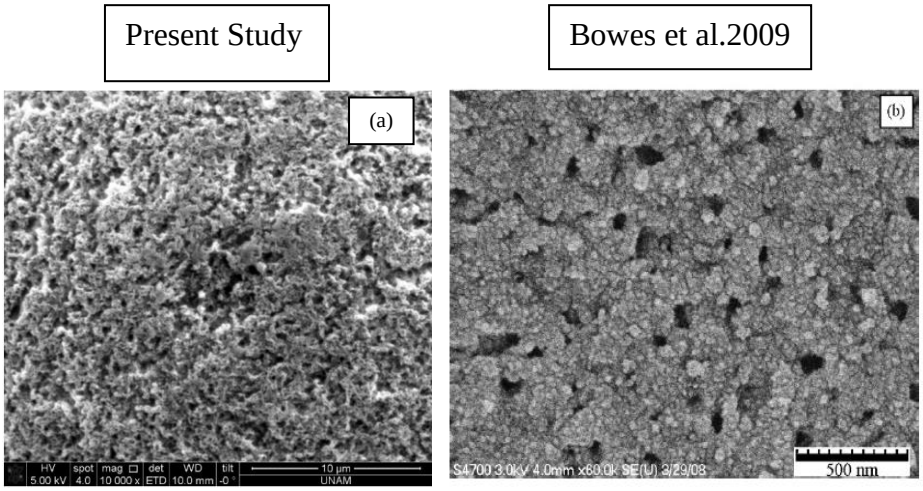

Figure 4.15. SEM images of Gigacap Q-650M(a) and SP Sepharose XL(b) (Bowes et al. 2009)

Figure 4.15 illustrates the microstructures of Gigacap Q-650M and Sepharose XL. The base matrix of Sepharose XL (Figure 4.15.b) is crosslinked agarose, and it is polymer modified with dextran molecules while Gigacap Q-650M (Figure 4.15.a) has the hydroxylated methacrylic polymer beads chemically modified. Bowes, 2009 has used different sample preparation methods. After protein loading, they have fixed the sample chemically by aldehydes and OsO_4 (Bowes et al. 2009). That is why applied procedure for SEM analysis is different from this study. Although polymer-modified media of Gigacap Q-650M is unknown, it is seen that both exchangers exhibit similarities. It seems that SP Sepharose XL has bigger pores than Gigacap Q-650M. Besides, protein has partitioned into dextran layer in Sepharose XL. However, it is difficult to reach a conclusion on structure comparison due to the used SEM mode, focusing magnification differences, and differences in preparation methods.

Structural analysis of Gigacap S-650M by using SEM with secondary electron mode has been investigated in Koku's unpublished research. It would be meaningful to compare Gigacap Q-650M and S-650M. Both ion exchangers have similar properties and preparation methods are the same. Thus, to verify the results of the SEM analysis of Gigacap Q-650M, structural comparison should be done. Figure 4.16 illustrates the comparison of Gigacap Q-650M and Gigacap S-650M.

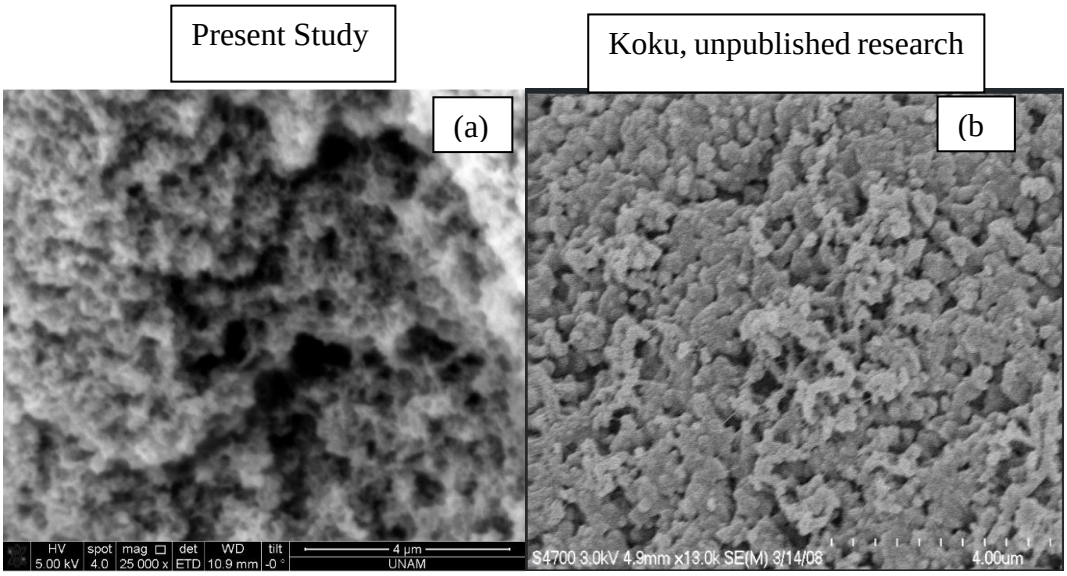

Figure 4.16. SEM Analyses of Gigacap-Q650M by using secondary electron mode(a) and Gigacap-S650M by using secondary electron mode(b) (Koku 2011).

The only differences between Gigacap Q-650M (anion exchanger) and S-650M (cation exchanger) are secondary polymeric phases. They have the same methacrylate base matrix. Because of having the same base matrix, structures of both ion exchangers seem similar, as seen in Figure 4.16. Sample preparation methods were the same for both Gigacap Q-650M and Gigacap S-650M. However, protein loading amount was 211 mg/ml for Gigacap S-650M, whereas 57.8 mg/ml protein was loaded to Gigacap Q-650M. Thus, higher resolution was obtained in Figure 4.16.b because of the higher protein loading amount. Nevertheless, both adsorbents exhibit similar microstructures. Gigacap Q-650 M (Figure 4.16.a) images have been captured by SE mode, black regions reflect the voids, whereas grey or white regions represent the polymer-modified sample. Resolution is limited when using secondary electron mode of SEM since image formed related to at least partly on the backscattered electrons. After protein loading, if Gigacap Q-650M particles would be exposed to fixation by aldehydes, contrast may be better than it is.

4.2.3. FIB Analyses of Gigacap Q-650M Structure

Gigacap Q-650M (having 57.8 mg/ml adsorbed protein) were imaged by using FIB-SEM combination technique. Images were taken at BSE mode of SEM by UNAM, BILKENT.

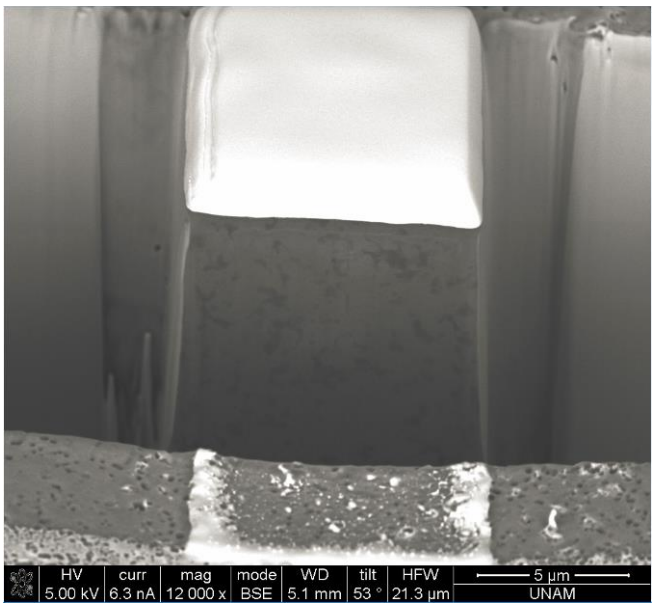

Figure 4.17. Cross-sectional view of Gigacap Q-650M after milling

As shown in Figure 4.17, at 5 kV voltage, 6.3 nA current, contrast, and the resolution was not good enough to observe the structure of Gigacap Q-650M. The white layer over the sample was platinum coating. To prevent any damage on the sample because of the gallium ions, before the imaging, platinum has been coated. Nevertheless, images were taken after each 100nm milling.

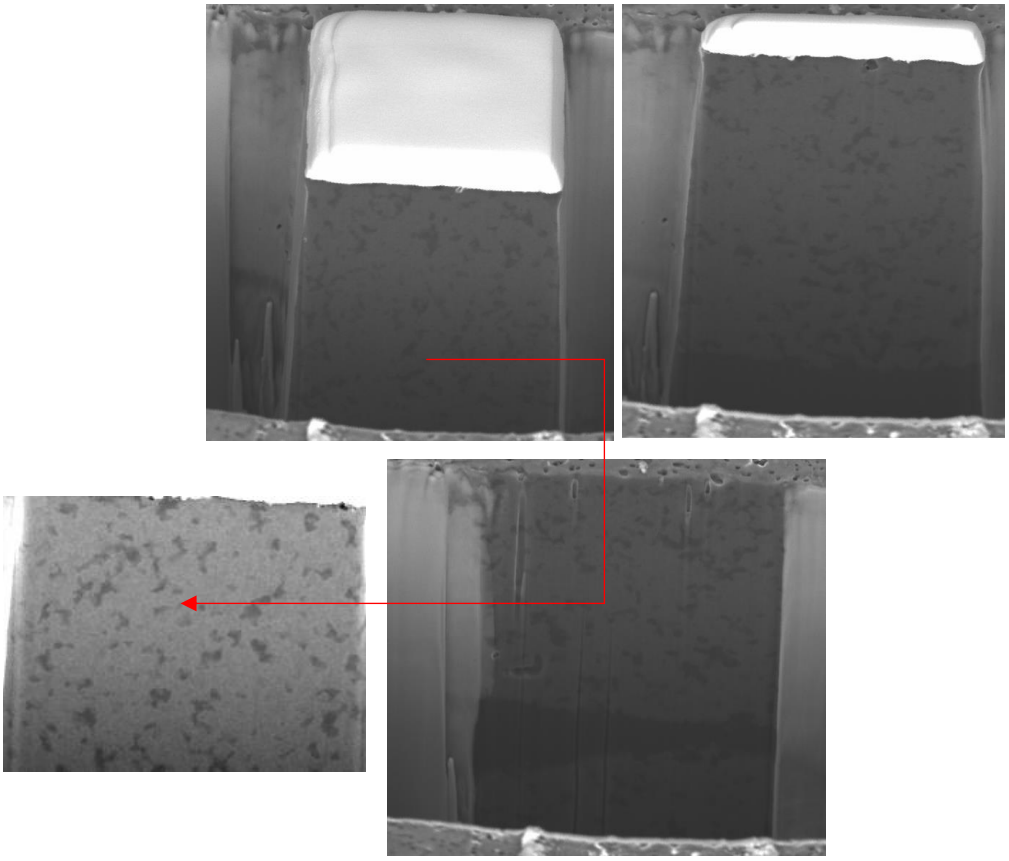

Figure 4.18. Cross-sectional view of Gigacap Q-650M after several milling

Figure 4.18 indicates taken images at BSE mode of SEM. All images had 1024x884, 8 bit. Dark grey areas were stated as resin, and darker grey areas were Gigacap Q-650M particles. However, as mentioned before, contrast is so low that is why we cannot comment on the structure. However using ImageJ software, contrast is obtained by tuning up on brightness/contrast level as stated with red arrow. The aim was to use FIB images for reconstruction. However, in this case, it can be concluded that these resolutions and the contrast were not good enough to reconstruct the images. Contrast level could be increased by loading more protein on Gigacap Q-650M or by performing en-bloc staining by Lead acetate, Uranyl acetate, or Uranyless contrast may be increased. Mostly, if images are taken at low magnification levels, higher beam current may be chosen. Therefore, resolution may be increased by using low spot size and higher beam current.

4.3. Microstructure analyses of HALO Particles by Electron Microscopy Techniques

In this section, several imaging techniques were applied to investigate the microstructure of the HALO particles. Summary of imaging runs were tabulated below.

Table 4.6. *Summary of sample treatments methods and imaging modes*

Imaging Run	Imaged Material	Imaging Method/Mode	Sample Preparation Treatment
1	HALO- 3.4 μm	SEM/SE	Free particles
2	HALO-5 μm	SEM/SE	Free particles
3	HALO- 3.4 μm	FIB/SEM	HALO with adsorbed protein,embedding protocol
4	HALO- 3.4 μm	FIB/SEM	HALO with adsorbed protein,en-bloc staining by Uranyless methanol mixture
5	HALO- 3.4 μm	FIB/SEM	HALO with adsorbed protein,en-bloc staining by Lead citrate
6	HALO-5 μm	FIB/SEM-SE at 800 pA	Free particles
7	HALO-5 μm	FIB/SEM-SE at 470 pA	Free particles
8	HALO-5 μm	FIB/SEM-In SE at 470 pA	Free particles

4.3.1. SEM Analyses of HALO Particle Structure

SEM images were captured of HALO core-shell particles from Advanced Materials Technology, having a diameter of 3.4 and 5 μm. After samples were coated by Pd-Au alloy, SEM images were taken at 20 kV in secondary electron mode. However, to avoid any damage on samples because of the high level of voltage, images were taken at 10 kV firstly, then beam voltage was increased gradually.

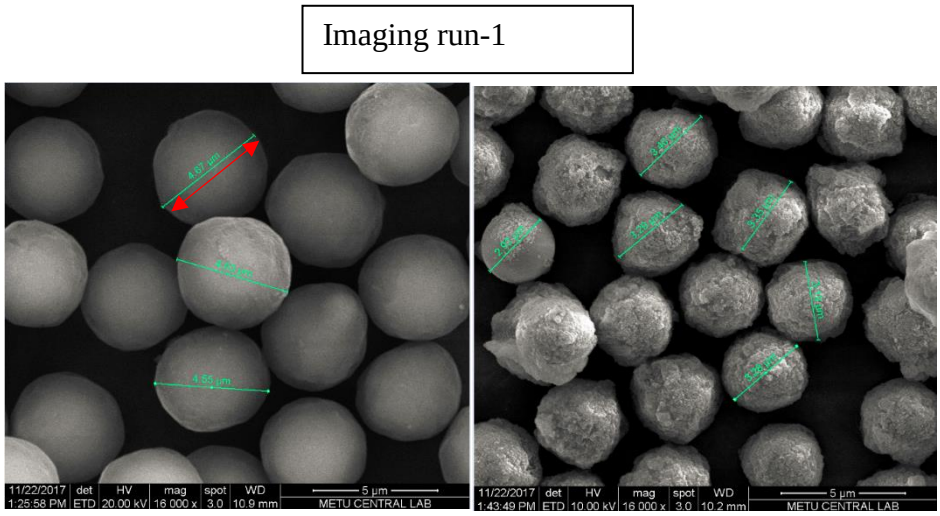

Figure 4.19. Comparison of SEM images of HALO particles in different sizes (left side-having diameter of 5µm-beam voltage is 20kV; right side-having particle diameter of 3.4 µm-beam voltage is 10 kV)

It can be seen from Figure 4.19 that HALO particles are spherical. It was seen that images contrast is better while running the device having voltage beam is 10kV. Actually, image resolution was lower at 10 kV, whereas the contrast was increased. Optimum working parameter should be found since higher voltage can cause damages of feature of HALO particles. Even though the theoretical HALO particle diameters are 5 and 3.4 µm as specified by the manufacturer, obtained diameters from the SEM analyses are somewhat below the theoretical diameters. For HALO 5µm particles, measured diameters were changing from 4 to 4.67 µm. For HALO 3.4 µm, diameters vary from 2.97 to 3.4 µm. Maybe some regions of particles could be split due to the mobilization.

Additionally, all measurements were taken manually over the images, and measurement errors are also possible. Besides, HALO particles may have diameter tolerances. However, there was not any information about it in the technical data sheet of HALO.

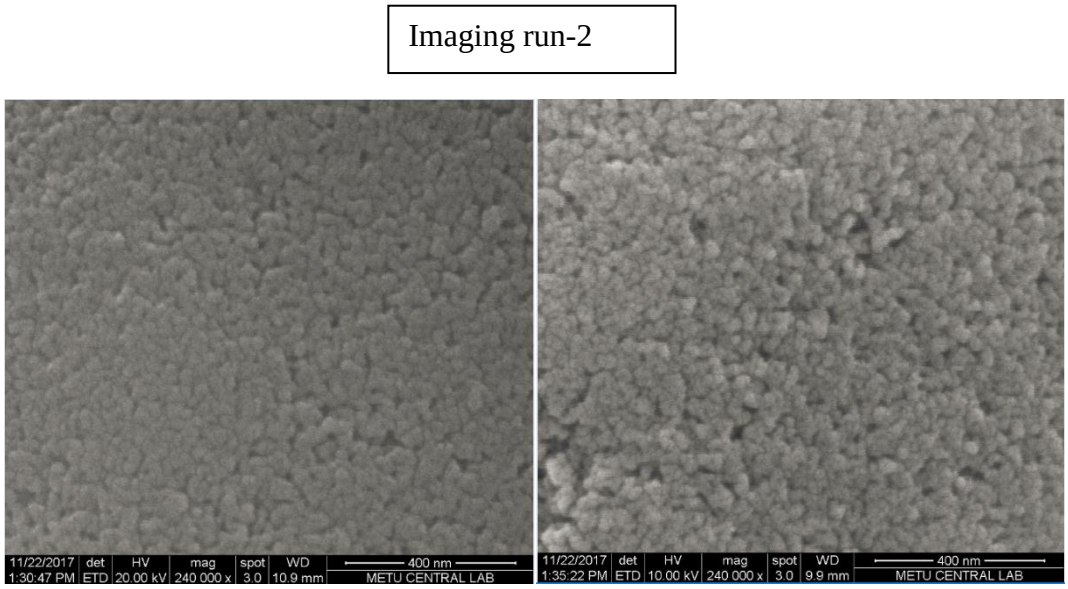

Figure 4.20. Comparison of SEM images of sample having 5µm diameter by changing beam voltage

By decreasing the beam voltage from 20kV to 10 kV better contrast was obtained seen in Figure 4.20. However, working with higher voltages can help to get high resolution.

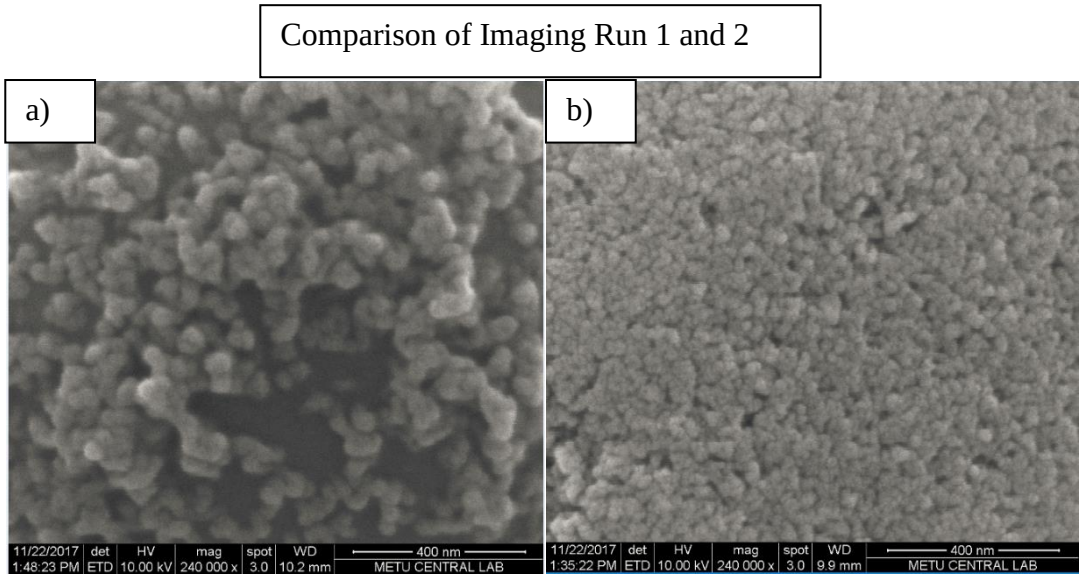

Figure 4.21. HALO particles sections having diameter of 3.4 µm (a) and 5µm (b)

HALO particle features (displayed in Figure 4.21) reflect core and shell geometry. Lighter regions in the images (magnification x 240.000) show the porous side; dark

areas show the core side of the samples. Captured images of 5µm (Figure 4.21.b) at the magnification of 240.000 have lower contrast than the particle having a diameter of 3.5 µm (Figure 4.21.a). Focusing may be hard while having working distance is low. By increasing the working distance, it may be obtained a better depth of focus; however, in this case, resolution may be poorer. Moreover, pore diameter of HALO 3.4µm seems greater than HALO-5µm particles, and it supports the literature pore diameters of HALO particles which are different in particle size (HALO-3.4µm. pore diameter is 400Å, HALO-5µm. pore diameter is 160Å) (Advanced Materials Technology Inc. 2018).

Maier and his colleagues, 2018 worked on a superficially porous particle bed model, and the model particles are composed of solid spherical core which is surrounded by porous shell. They have assumed the porous shell as small spheres (Maier and Schure 2018). Additionally, Hatipoglu et al. 2017, has improved mathematical modeling, i.e., a random-walk based algorithm, to simulate diffusion in a core-shell particle geometry. Diffusion simulations were carried out on a randomly packed geometry formed from these particles (Hatipoğlu and Koku 2017). To support it, SEM images of HALO particles were taken in secondary electron mode to see the microstructure of shell part of the HALO.

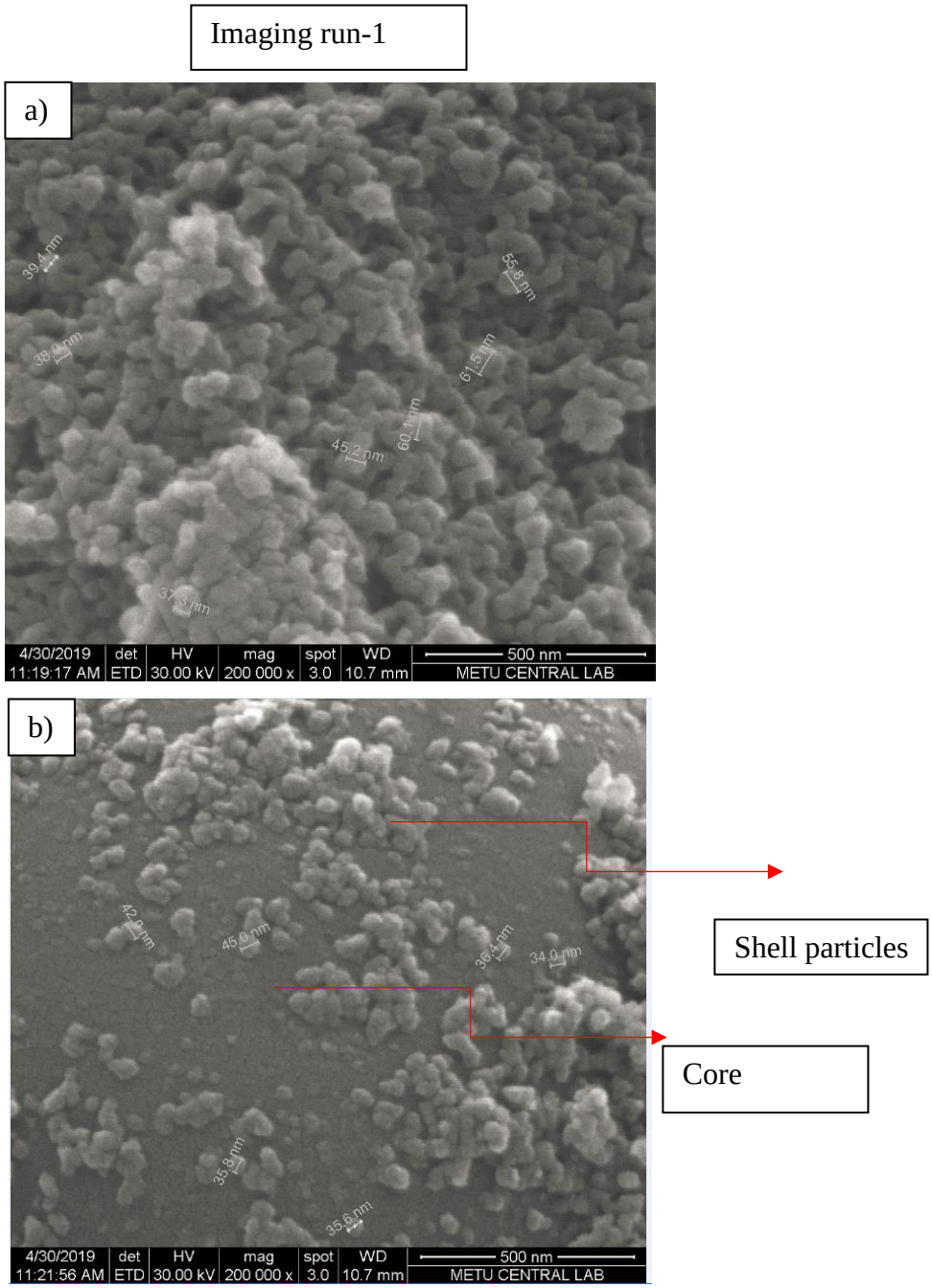

Figure 4.22. SEM images of Shell part of 3.4µm of HALO particle

Figure 4.22.a shows that the HALO particle shell side is composed of spheres and diameters that vary from 34 nm to 61.5 nm. Maier et al. 2018, assumed the diameter of the sphere along the shell side of HALO as 57.5 nm (Maier and Schure 2018) while modeling the HALO particles. In this study, Maier's assumption has been proven.

Due to the movement of samples, shell particles seem to be damaged and split apart from the core side, as illustrated in Figure 4.22.b. The reason for this, the core side of the HALO can be seen partly. Figure 4.23 demonstrates the microstructure of the shell side of HALO and the approximate shell thickness of the sample.

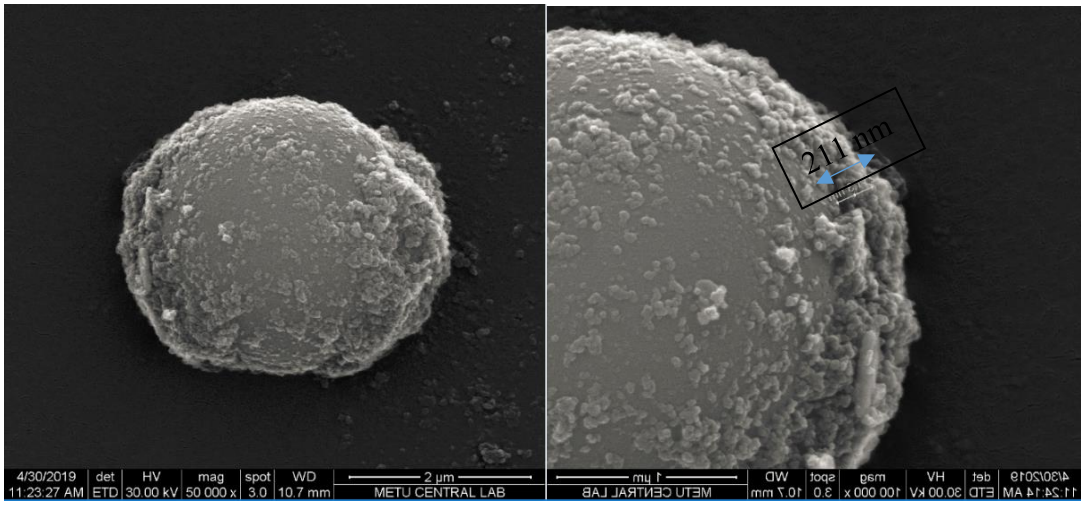

Figure 4.23. SEM images of 3.4µm HALO particles

It was measured approximately shell thickness of the sample as 211nm as seen in Figure 4.23. The theoretical shell thickness of HALO 3.4µm is 0.2µm (Advanced Materials Technology Inc. 2018). Accordingly, theoretical shell thickness and the measured shell thickness by SEM is nearly the same.

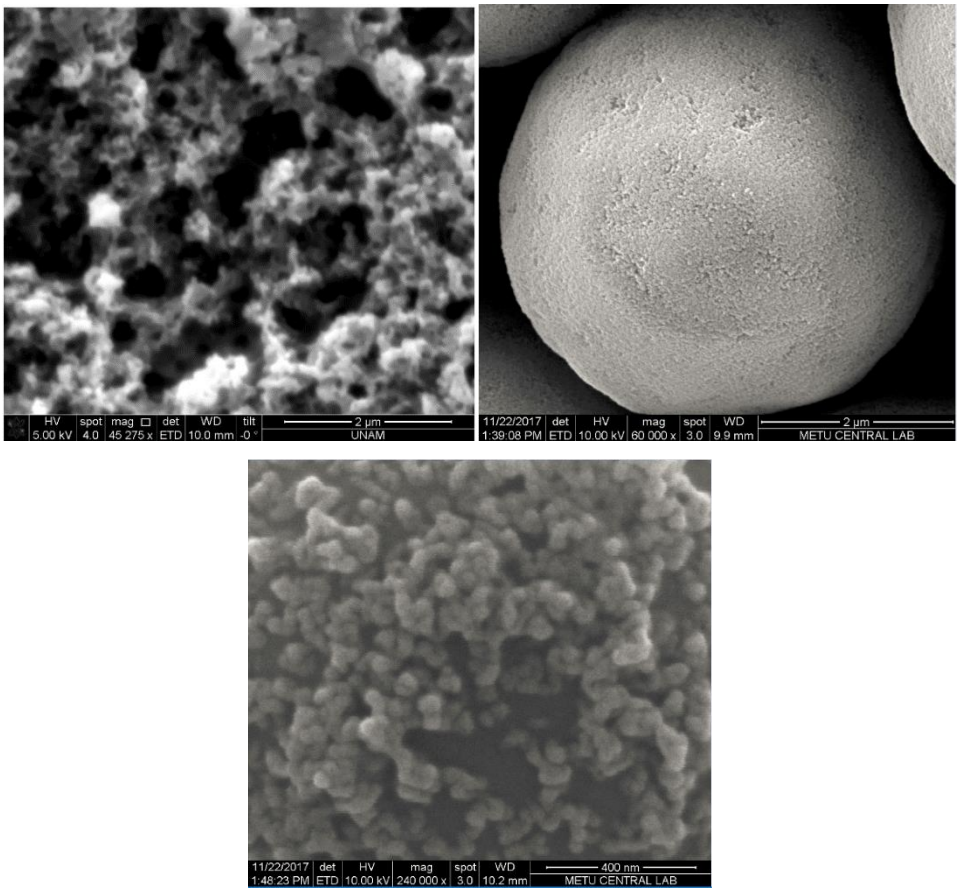

Figure 4.24. Gigacap-Q650M (top left) and HALO particles (top right & bottom) SEM images

Gigacap Q-650M and HALO adsorbents have different microstructures, as seen in Figure 4.24. Fibers and pores of Gigacap-Q650M (Figure 4.24-top left image) are quietly visible. Gigacap Q-650M may have tentacle structure with polymer modification. On the other hand, HALO particles (Figure 4.24-top right and bottom image) have core-shell structures, and it can be seen porous particles in the shell side is quite visible. At low magnification levels, HALO particles seem as spherical in shape, and shell and core region cannot be seen distinctly visible. The darker region in HALO particle seems as core side.

4.3.2. FIB and TEM Analyses of HALO Particle Structure

As mentioned in section 3.3.3, two HALO samples were prepared, which were embedded and free particles. While preparing the embedded HALO sample, three different treatments were used to obtain stained particles. Figure 4.25 shows sample appearances after being exposed to different treatments.

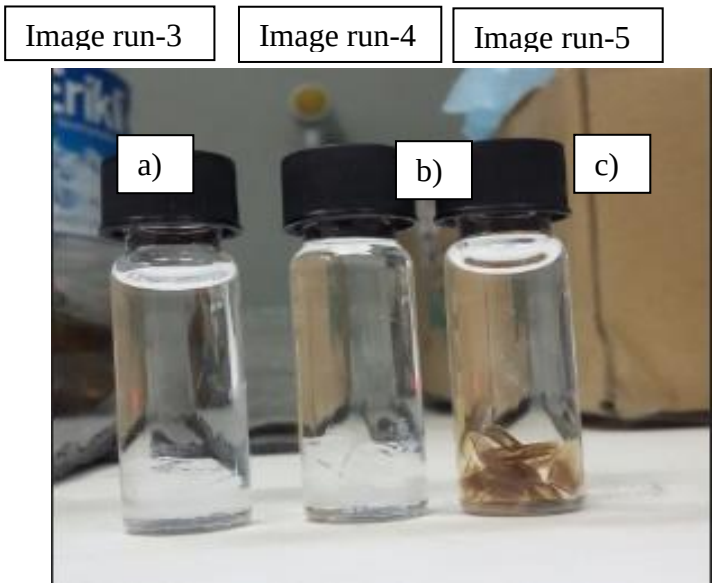

Figure 4.25. Sample appearances after fixation by OsO4 (image run-3); fixed by Uranyless-methanol solution (image run-4); En-bloc staining by Lead Citrate (image run-5).

.

Image run-3 in Figure 4.25.a was captured after post-fixation by OsO_4. It can be said that OsO_4 fixation did not provide staining on the HALO. Maybe adsorbed protein amount was not high to interact with OsO_4 or HALO does not have enough functional group to form a crosslink.

Image run-4 was illustrated in Figure 4.25.b shows the HALO sample after Osmium tetroxide followed by Uranyless-methanol solution. Uranyless-methanol solution did not provide any staining on the sample. Uranyl acetate has the highest solubility in alcoholic solution such as methanol (Leica Microsystems 2013). That is why even if Uranyless does not have any uranyl ion, to test whether or not Uranyless behaves

similarly like Uranyl acetate, methanol solution was used. However, it seems that Uranyless methanol solution failed according to staining performance on the sample. Maybe Uranyless concentration was not enough to get a stain.

The last treatment was done with lead citrate, as shown in Figure 4.25.c (image run-5). By using lead citrate, staining was obtained. The enhancement of the contrasting effect depends on the interaction with OsO_4 since it allows the attachment of lead ions to the polar groups of molecules. That is why Lead citrate en-bloc staining method seems to work better.

Hardened samples are shown in Figure 4.26.

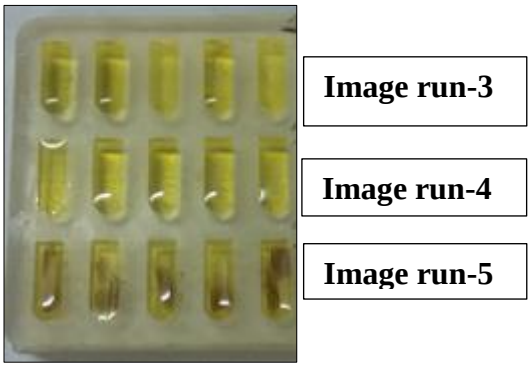

Figure 4.26. Hardened samples in silicone flat mold after taking out of fume hood. Upper samples (image run-3) were exposed to OsO4 fixation, Middle sample (image run-4) were exposed to Uranyless-Methanol en bloc staining method, Bottom samples (image run-5) were exposed to lead citrate en-bloc staining method.

Each row of hardened sample in Figure 4.26 corresponds to a different sample treatment as mentioned above. After trials on treatment method, embedded particles treated by Lead citrate (Image run-5 in Figure 4.26) was used for imaging.

Before imaging, platinum deposition on sample were done to improve imaging quality. Then, embedded HALO particles were imaged.

Firstly, 20µmx20µm area was chosen for imaging over the sample (illustrated in Figure 4.27). Slice thickness was set to 200 nm.

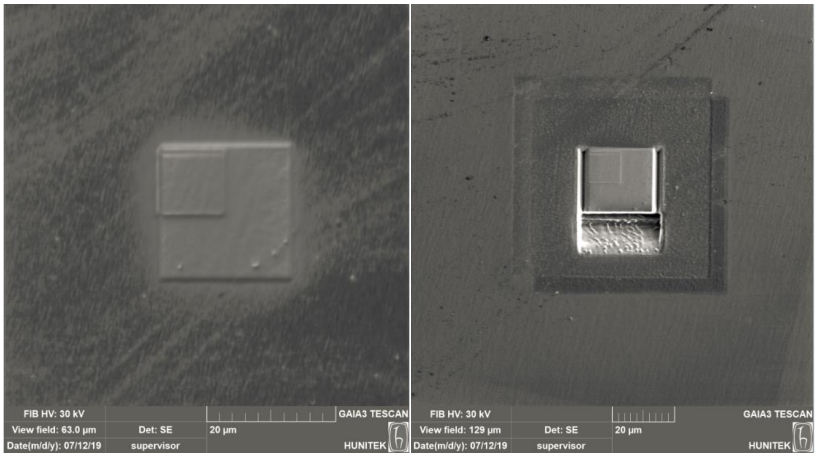

Figure 4.27. Chosen sample area for milling

SEM secondary electron mode was used for imaging, and beam voltage was 5kV. After each milling, polishing was done to obtain high-quality images.

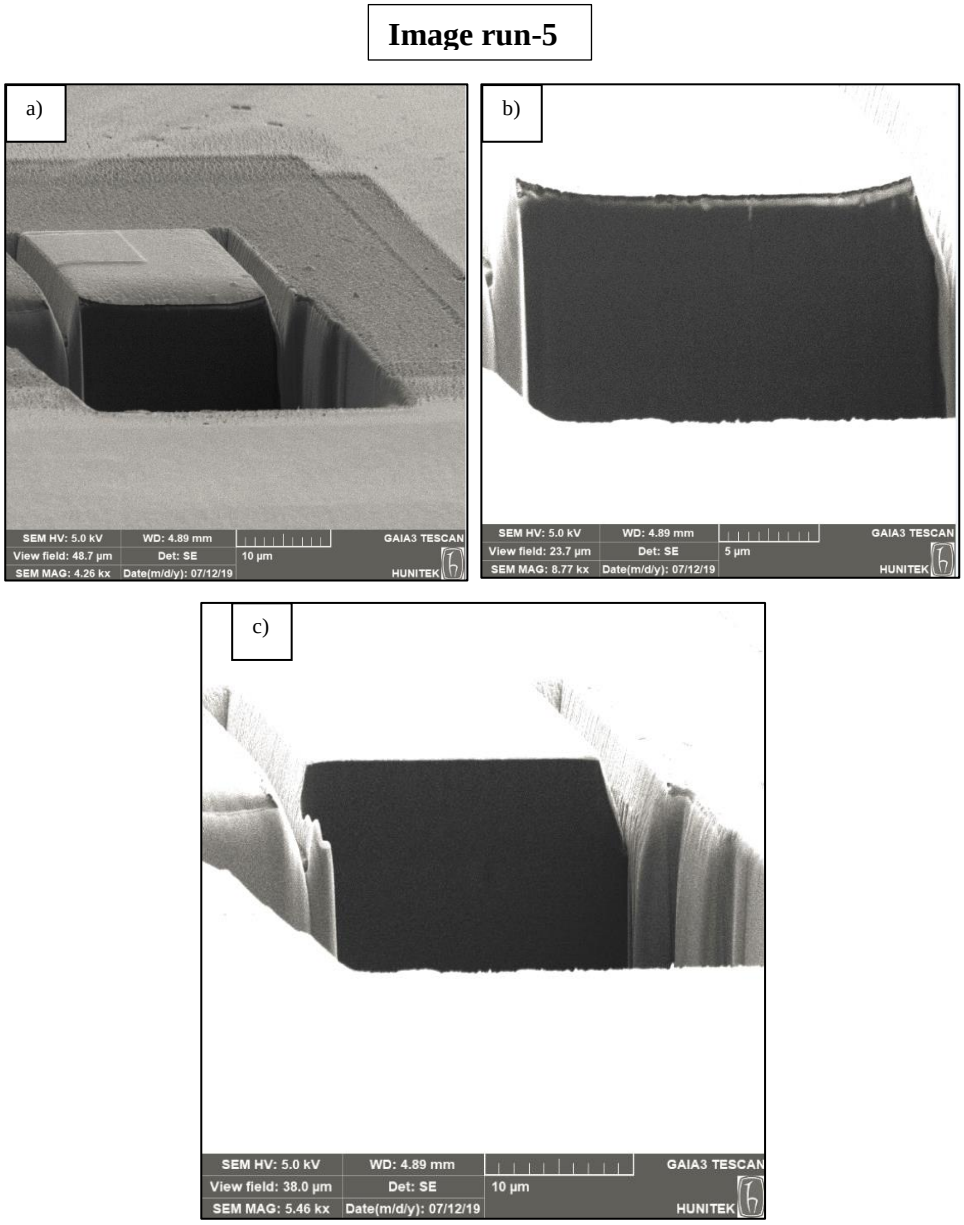

Figure 4.28. FIB images of the HALO during milling

Figure 4.28 (a) shows the first section of the sample after first milling by 200nm thickness. Dark Black area shows the resin. In Figure 4.28 (b) and (c) bright top layer seems like a platinum-coated layer. After three milling steps, the last milling section was 2µm thickness, and the HALO particle could not be imaged. Only visible area was the resin. Embedded sample imaging (image run-5) by FIB was not successful. The reason for this, the chosen area for imaging may not have an embedded sample.

Actually, by using the microtome, the embedded HALO sample was trimmed to bring out around the surface of resin. Maybe the sample cannot be taken to surface by using microtome because of lack of visibility. Thus, even if marking protein and en-bloc staining method by lead citrate were used to increase the contrast level, SEM images cannot detect the sample structure.

As embedded HALO particles could not be imaged, free HALO particles coated by Pd-Au were imaged as an alternative.

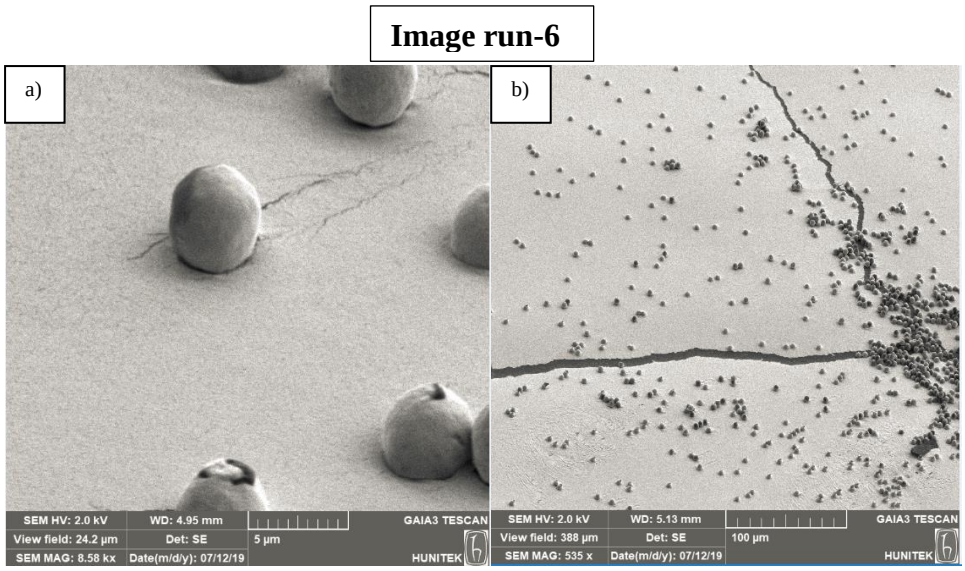

Figure 4.29. SEM images of HALO particles before the milling,

Figure 4.29 shows the HALO particle images before the milling by using secondary electron mode at 2kV. Figure 4.29 (a) has a higher magnification than Figure 4.29 (b). Section thickness for milling was 200 nm. Images were taken at 800 pA current.

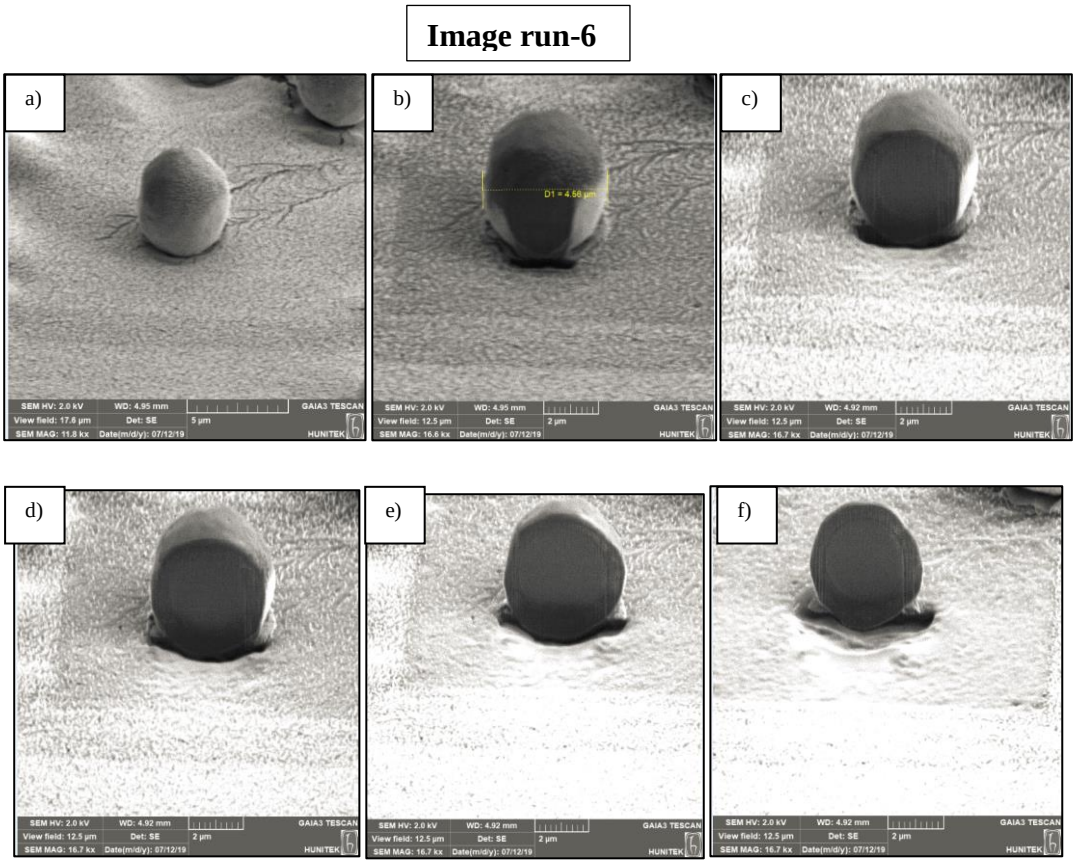

Figure 4.30. Milled images of HALO particles at 800 pA current

The applied current was 800 pA. However, due to the high current amount, in each milling step, the HALO sample has moved slightly from the previous location. Indeed, in each sectioning, the core part of the HALO particles has not been seen. The diameter of the HALO particle was measured as 4.56 μm as seen from Figure 4.30 (b). It is quite close to the theoretical diameter, which is 5 μm. The differences may occur because of the abrasion of the samples due to the transportation, or manual measurement.

Applied current was changed from 800 pA to the 470 pA to decrease the harm on the sample because of the current. Besides, to see the effect of current on sample resolution, current was decreased from 800 pA to 470 pA.

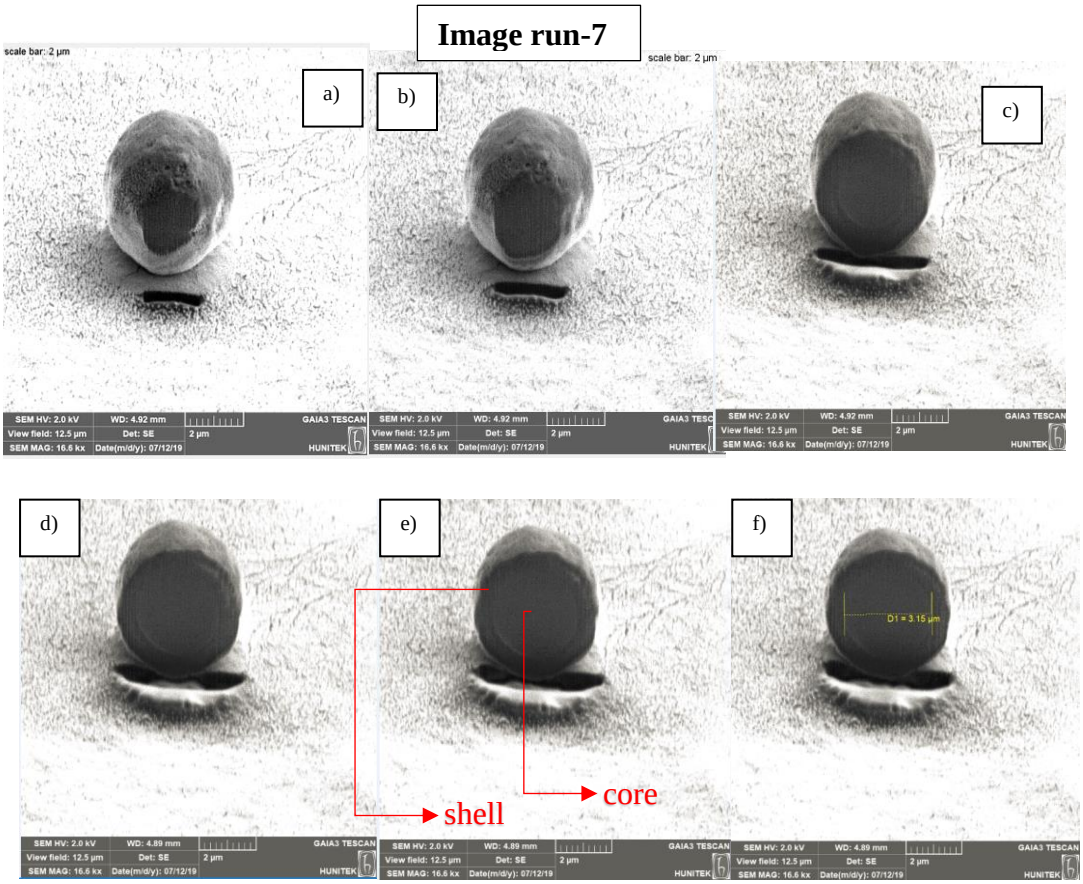

Figure 4.31. Milled images of HALO particles at 470 pA current

Figure 4.31 shows the milled view of the HALO. In total, 14 sectioned images were taken. At 470 pA current, sample movement was decreased. However, still, it was hard to cut the samples slice by slice without causing any movement of the sample because the sample was not fixed in resin. That is why embedding technique may give better results concerning rigidity. Besides, when decreased the applied current, clearer images were taken. The approximate core diameter of HALO was measured as 3.15µm as seen from Figure 4.31 (f). Measured core particle size is quite close to the size mentioned in the technical data sheet of HALO, which is 3.3 µm (Advanced Materials Technology Inc. 2018). Small size difference may come from the measurement error. All images were taken by using secondary electron mode of SEM. Then, imaging mode was changed from SE to Immersion lens. The aim was to obtain

higher resolution images that can be seen clearer boundary layer between the shell and the core.

Image run-8

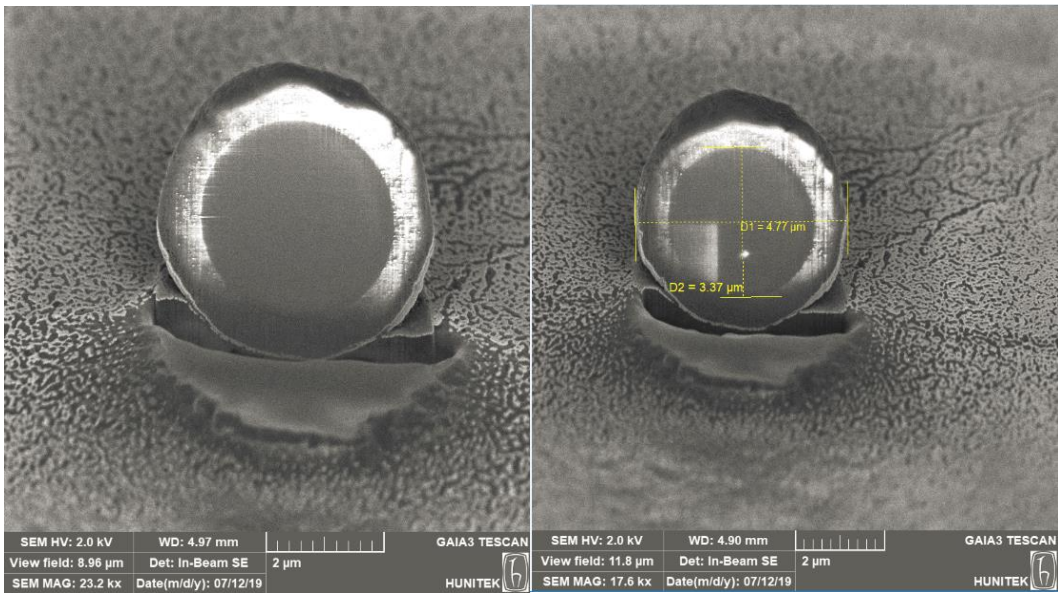

Figure 4.32. HALO particle core-shell section image by using FIB/In-Beam SE

As seen from Figure 4.32, cross-sectional surface reflects the core and the shell area of the particle. There are some light and bright areas over the shell side, but this is because of the imaging working parameters to get high-resolution images. Maybe bright areas exist because of the gallium ions used for milling, and it caused the charging of the sample. Dark circle shows the core side of the particle. Over the cross-sectional area, overall and the core side diameters of the particle has been tried to measure. Core diameter was found as 3.37µm whereas overall diameter was found as 4.77µm.

In Figure 4.32.a, brightening effect is substantial, and it affects the resolution of the image. To decrease bright surfaces, immersion-lens configuration parameters were changed to obtain higher resolution. Detailed imaging parameters are stated in appendix H.

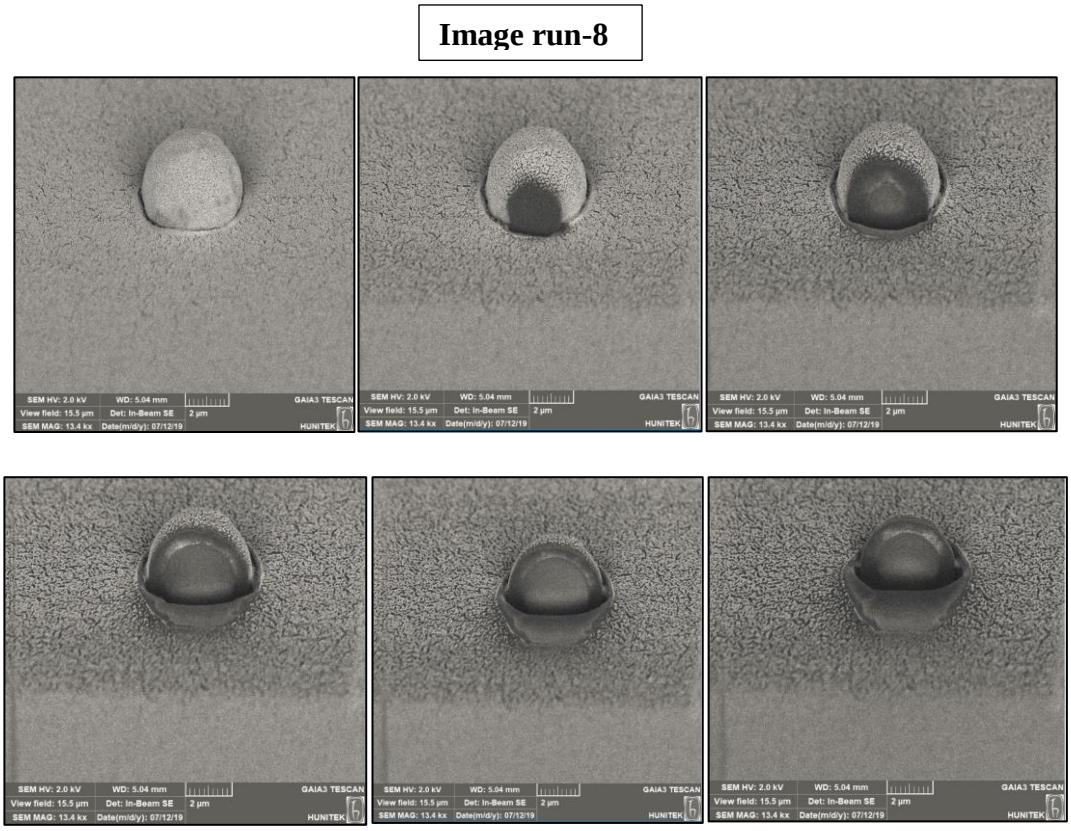

Figure 4.33. Captured HALO FIB images by using Immersion lens

Figure 4.33 shows the FIB images of HALO particle slice by slice, each slice with a thickness of 200 nm, and in total, nineteen images were taken. The spot size was 4 nm. Image resolution is higher when compared to Figure 4.32. Core and the porous side of the HALO particle is seen from the Figure 4.32. Before milling the sample, HALO particle seems embedded on carbon tape. In each milling, the sample seems embedded more because of the beam intensity. Ions may harm the carbon tape, and the tape may flake away over the stub, and they may cover the sample surface. To form an image, immersion lenses generally combine with energy filtering of secondary electrons (Egerton 2006). The signal from an immersion lens detector corresponds to secondaries emitted almost perpendicular to the specimen surface, and by the help of this the SE image shows no directional or shadowing effects (Egerton 2006).

TEM imaging was examined on the HALO particles were treated by lead citrate. However, due to the rupture of samples while trimming by microtome, TEM images did not give any detailed results on microstructures. TEM images of the HALO particles are found in appendix M.

Simulating of mass and fluid transfer along the complex is hard to obtain by using continuum equations. By obtaining microstructures of these stationary phases, imaged-based, direct physical reconstructions of these geometries are good options to simulate mass transfer or flow. To achieve this, 2D image resolutions are highly important for 3D reconstruction. First, it should be noted that the resolution is a function of the location of osmium clusters and also proteins that are adsorbed on the sample. Besides, treatments by heavy metals also give contrast to the samples. If high-resolution images can be obtained, mesoscopic analysis can be done by using direct image-based methods.

CHAPTER 5

CONCLUSIONS AND RECOMMENDATIONS

The main aim of this study was to analyze the microstructures of novel chromatographic adsorbents by using high-resolution imaging techniques. Ion exchangers which are Gigacap Q-650M and HALO particles were used for microstructure analysis.

Electron microscopy analyses were done for both Gigacap Q-650M and HALO particles. The structure of Gigacap Q-650M was imaged. Previous research also shows the structural studies of Gigacap S-650M, which has a similar structure with Gigacap Q-650M except that secondary polymeric phases. It was found that Gigacap Q-650M and S-650M reflect similar topography. HALO particles having a diameter of 3.4 μm and 5μm were also imaged by using SEM. According to SEM images, the shell side of the HALO particles was seen clearly, whereas the core side of the HALO could not be observed. While increasing the imaging magnification such as 240.000x, the porous structure of the HALO was observed clearly. Additionally, the splitting of porous particles from the surface of the core side enabled to see some part of the core side of HALO.

Polymer modified ion exchanger Gigacap Q-650M was also imaged by TEM. However, without applying any staining protocol, contrast cannot be achieved. Therefore, to get high-resolution imaging, post-staining, en-bloc staining methods and staining proteins were applied. Protein localization was mapped. Since proteins were adsorbed by Gigacap Q-650M, they were seen as darker areas. Besides, the more protein attached to the ion exchanger, the more contrast was obtained. En-bloc staining and post-staining method by using Uranyless were compared. While using the en-bloc staining method, higher contrast images were gathered. Thus, it helps to get an idea about the structure of the Gigacap Q-650M more. To obtain 3-D topography of the Gigacap Q-650M and HALO particles, FIB technology was used. Each slice of

Gigacap Q-650M was 100nm and after each milling images were taken by using SEM backscatter electron mode. However, obtained images have no excellent resolution and contrast. Each image has 1024x884 pixel. That is why, for 3-D reconstruction, taken images were not good enough. HALO particles structure analyses were also done by using FIB. Different staining methods were used, such as Uranyless staining, lead citrate staining, and OsO4 staining. Lead citrate staining gave the most contrast on the sample. Embedded HALO particles could not be imaged even if they are stained by lead citrate. This may be due to the sample orientation along the resin in such a way that the sample may not be close to the surface of the resin. That is why free HALO particles have been tried to be analyzed. Core and shell side of the HALO particle were imaged by taking slices around 200 nm. After each milling, images were captured just after the polishing steps to get better resolution. Moreover, the effects of current were noted on the resolution of images. At 480 pA HALO particle microstructure is more visible and resolution was better than the images taken at 800 pA. Additionally, SEM modes have been changed to obtain better images. When using an immersion lens, obtained images have more contrast and higher resolution than secondary electron mode. Approximately 20 slices were imaged then by using ImageJ analysis software. Each 2-D slices were reunited and finally generated a 3-D image of HALO particle.

Mostly, in this study, qualitative analysis was studied. However, by using obtained 2D images, quantitative analysis can also be analyzed. Pore size distribution and static capacity estimations can be examined by using image-based toolbox such as Matlab imaging toolbox and ImageJ.

For similar imaging researches, several recommendations could be taken into consideration.

- In this work, the critical point drier method could not be applied before the SEM imaging for dehydrating of the sample. By using CPD, the sample can

be imaged without surface tension effect, which deface structure and the morphology.

- Gigacap Q-650M has a functional group. That is why it is easy to bind staining proteins, even if it is big enough, such as BSA. However, to stain HALO particle, small protein molecules should be used, such as α-lactalbumin to be adsorbed. Halo-5μ has no functional group, and staining by protein was not a successful method.
- Lead citrate was used for staining of HALO particle. However, to obtain more staining on sample, lead citrate and uranyl acetate can be used together.
- Embedding of sample in resin is highly important to get better images for FIB. Since, because of the gallium ion density, after each milling, the sample was moved backward more, and it affects milling. FIB imaging of embedded HALO particle was unsuccessful since the sample was not the surface of the resin. It should be noted that the sample should be as close as possible to the resin surface to enable imaging.
- While imaging of not embedded sample by using FIB, applied current should be lower not to dislocate the sample. Since the particle is not fixed, applying high current may cause the dislocation of the sample, and it affects the resolution and the image quality.

REFERENCES

Advanced Materials Technology. 2019. “HALO Bioclass Catalog.” : 20.

Advanced Materials Technology Inc. 2018. “Discover the Advantages of HALO and HALO BioClass Fused-Core® Columns.”

Amersham, Pharmacia. 1991. “Chromatography Ion Exchange Chromatography.” *Ion Exchange Chromatography: Principles and Methods*: 9–154.

Aragon, Sergio, and David K Hahn. 2006. “Precise Boundary Element Computation of Protein Transport Properties: Diffusion Tensors, Specific Volume, and Hydration.” *Biophysical journal* 91(5): 1591–1603. http://www.ncbi.nlm.nih.gov/pubmed/16714342 (April 19, 2019).

Barbosa, Leandro R S et al. 2010. “The Importance of Protein-Protein Interactions on the PH-Induced Conformational Changes of Bovine Serum Albumin: A Small-Angle X-Ray Scattering Study.” *Biophysical journal* 98(1): 147–57. http://www.ncbi.nlm.nih.gov/pubmed/20085727 (April 19, 2019).

Belazi, Dalila et al. 2009. “Chemical Analysis of Osmium Tetroxide Staining in Adipose Tissue Using Imaging ToF-SIMS.” *Histochemistry and Cell Biology* 132(1): 105–15.

Bioscience, Tosoh. 2014. “Product Specification Sheet Toyopearl NH2-750F.” 49(July): 70567.

Bowes, Brian D., Harun Koku, Kirk J. Czymmek, and Abraham M. Lenhoff. 2009. “Protein Adsorption and Transport in Dextran-Modified Ion-Exchange Media. I: Adsorption.” *Journal of Chromatography A* 1216(45): 7774–84.

Brooks, C. J. W. 1986. *Trends in Analytical Chemistry. Volume 5 : TrAC. Volume 5*. https://books.google.com.tr/books?hl=en&lr=&id=vIPNCgAAQBAJ&oi=fnd&pg=PA82&dq=amino+acid+net+charged+calculation&ots=P6U_KFTp9G&sig=v98Yf4pEbyrmusdO43RC1cAv1yI&redir_esc=y#v=onepage&q=amino acid net charged calculation&f=false (March 10, 2019).

Bruns, Stefan, and Ulrich Tallarek. 2011. “Physical Reconstruction of Packed Beds and Their Morphological Analysis: Core-Shell Packings as an Example.” *Journal of Chromatography A* 1218(14): 1849–60.

“Calculator for PH Buffers.” 2018.

https://www.liverpool.ac.uk/pfg/Research/Tools/BuffferCalc/Buffer.html (August 4, 2019).

Carta, Giorgio, Antonio R. Ubiera, and Timothy M. Pabst. 2005. "Protein Mass Transfer Kinetics in Ion Exchange Media: Measurements and Interpretations." *Chemical Engineering and Technology* 28(11): 1252–64.

van Deemter, J.J., F.J. Zuiderweg, and A. Klinkenberg. 1956. "Longitudinal Diffusion and Resistance to Mass Transfer as Causes of Nonideality in Chromatography." *Chemical Engineering Science* 5(6): 271–89. https://www.sciencedirect.com/science/article/pii/0009250956800031 (March 14, 2019).

DeStefano, Joseph J., Stephanie A. Schuster, Jason M. Lawhorn, and Joseph J. Kirkland. 2012. "Performance Characteristics of New Superficially Porous Particles." *Journal of Chromatography A* 1258: 76–83. http://dx.doi.org/10.1016/j.chroma.2012.08.036.

Egerton, Ray F. 2006. Physical Principles of Electron Microscopy *Physical Principles of Electron Microscopy*.

Electron Microscopy Sciences. 2019. "UranyLess Protocols of Use: Classic Contrast." https://www.emsdiasum.com/microscopy/technical/datasheet/22409a.aspx (April 22, 2019).

Fok, A. C., and J. S. Cheah. 1987. "Schmidt's Syndrome: A Case Report." *Singapore Medical Journal* 28(3): 269–72.

Fornstedt, Torgny, Patrik Forssén, and Douglas Westerlund. 2015. "Basic HPLC Theory and Definitions: Retention, Thermodynamics, Selectivity, Zone Spreading, Kinetics, and Resolution." *Analytical Separation Science* (November): 1–24.

Ganguly Bhaskar. 2011. "Tissue Processing for TEM: Fixation, Rinsing, Dehydration and Embedding | Fixation (Histology) | Transmission Electron Microscopy." : 30. https://www.scribd.com/document/76636027/Tissue-Processing-for-TEM-Fixation-Rinsing-Dehydration-and-Embedding (September 15, 2019).

Glauert, Audrey M., Lewis, Peter R. 2014. "Biological Specimen Preparation for Transmission Electron Microscopy." *Cell Biology International* 23(8): 592. http://0-eds.a.ebscohost.com.library.metu.edu.tr/eds/ebookviewer/ebook/bmxlYmtfXzc5MDc3MV9fQU41?sid=6483ac8e-8a83-4d7d-8a9f-fd28f2bc97f5@sdc-v-sessmgr04&vid=2&format=EB (April 21, 2019).

Guiochon, Georges, and Fabrice Gritti. 2011. "Shell Particles, Trials, Tribulations and Triumphs." *Journal of Chromatography A* 1218(15): 1915–38. http://dx.doi.org/10.1016/j.chroma.2011.01.080.

Hagita, Katsumi, Takeshi Higuchi, and Hiroshi Jinnai. 2018. “Super-Resolution for Asymmetric Resolution of FIB-SEM 3D Imaging Using AI with Deep Learning.” *Scientific Reports* 8(1): 1–8. http://dx.doi.org/10.1038/s41598-018-24330-1.

Harrison, Roger G., Paul Todd, Scott R. Rudge, and Demetri P. Petrides. 2003. *Bioseparations Science and Engineering*. ed. Keith E. Gubbins. Oxford University Press. https://books.google.com.tr/books/about/Bioseparations_Science_and_Engineering.html?id=15IKBgAAQBAJ&redir_esc=y (August 18, 2019).

Hatipoğlu, Emre, and Harun Koku. 2017. “Modelling of Diffusion in Random Packings of Core-Shell Particles.” *Hacettepe Journal of Biology and Chemistry* 2(45): 269–75.

Hawe, Andrea, Wendy L Hulse, Wim Jiskoot, and Robert T Forbes. 2011. “Taylor Dispersion Analysis Compared to Dynamic Light Scattering for the Size Analysis of Therapeutic Peptides and Proteins and Their Aggregates.” *Pharmaceutical research* 28(9): 2302–10. http://www.ncbi.nlm.nih.gov/pubmed/21560019 (April 19, 2019).

Hayat, M.A. 1973. “Principles and Techniques of Electron Microscopy.” : 3–42.

Hayes, Richard, Adham Ahmed, Tony Edge, and Haifei Zhang. 2014. “Core – Shell Particles : Preparation , Fundamentals and Applications in High Performance Liquid Chromatography.” *Journal of Chromatography A* 1357: 36–52. http://dx.doi.org/10.1016/j.chroma.2014.05.010.

Helfferich, Friedrich. 1995. “Ion Exchange - Friedrich G. Helfferich - Google Books.” *Dover Publications,New York*: 603. https://books.google.com.tr/books?hl=en&lr=&id=F9OQMEA88CAC&oi=fnd&pg=PA1&dq=porous+ion+exchange+resins&ots=836zSO4P-t&sig=oB7bwDsX_SspDy_wWts41NszSGs&redir_esc=y#v=onepage&q=porous ion exchange resins&f=false (March 11, 2019).

Jeyachandran, Y. L., E. Mielczarski, B. Rai, and J. A. Mielczarski. 2009. “Quantitative and Qualitative Evaluation of Adsorption/Desorption of Bovine Serum Albumin on Hydrophilic and Hydrophobic Surfaces.” *Langmuir* 25(19): 11614–20. https://pubs.acs.org/doi/10.1021/la901453a (September 19, 2019).

Jungbauer, Alois. 2005. “Chromatographic Media for Bioseparation.” *Journal of Chromatography A* 1065(1): 3–12.

Jungbauer, Alois, and Rainer Hahn. 2009. 463 Methods in Enzymology *Chapter 22 Ion-Exchange Chromatography*. 1st ed. Elsevier Inc. http://dx.doi.org/10.1016/S0076-6879(09)63022-6.

Kaphingst, Kimberly A, Susan Persky, and Christina Lachance. 2010. 14 *NIH Public*

Access.

Koku, Harun et al. 2011. "Modeling of Flow in a Polymeric Chromatographic Monolith." *Journal of Chromatography A* 1218(22): 3466–75. http://dx.doi.org/10.1016/j.chroma.2011.03.064.

Koku, Harun. 2011. University of Delaware "Thesis: Microstructure-Based Analysis and Simulation of Flow and Mass Transfer in Chromatographic Stationary Phases." University of Delaware.

Koku, Harun, Robert S. Maier, Mark R. Schure, and Abraham M. Lenhoff. 2012. "Modeling of Dispersion in a Polymeric Chromatographic Monolith." *Journal of Chromatography A* 1237: 55–63. http://dx.doi.org/10.1016/j.chroma.2012.03.005.

Krinsley, D. H., Pye, K., Boggs, S., and Tovey, N. K. 1998. "Image Analysis, Sediments and Paleoenvironments - Google Kitaplar." *Springer*: 319. https://books.google.com.tr/books?id=SRGDk2Gbj4UC&pg=PA33&lpg=PA33&dq=Krinsley,+D.+H.,+Pye,+K.,+Boggs,+S.,+and+Tovey,+N.+K.+(1998).+Backscattered+Scanning+Electron+Microscopy+and+Image+Analysis+of+Sediments+and+Sedimentary+Rocks.+Cambridge:+Cambridge+Univ (August 2, 2019).

Leica Microsystems. 2013. "EM Sample Preparation-Contrasting." *Structural Biology*: 1–16.

Lenhoff, Abraham M. 2011. "Protein Adsorption and Transport in Polymer-Functionalized Ion-Exchangers." *Journal of Chromatography A* 1218(49): 8748–59. http://dx.doi.org/10.1016/j.chroma.2011.06.061.

Leonard, M. 1997. "New Packing Materials for Protein Chromatography." *Journal of Chromatography B: Biomedical Applications* 699(1–2): 3–27.

Maier, Robert S., and Mark R. Schure. 2018. "Transport Properties and Size Exclusion Effects in Wide-Pore Superficially Porous Particles." *Chemical Engineering Science* 185: 243–55. https://doi.org/10.1016/j.ces.2018.03.041.

Mellors, J. Scott, and James W. Jorgenson. 2004. "Use of 1.5-Mm Porous Ethyl-Bridged Hybrid Particles as a Stationary-Phase Support for Reversed-Phase Ultrahigh-Pressure Liquid Chromatography." *Analytical Chemistry* 76(18): 5441–50.

Ottens, Marcel, Johannes A. Wesselingh, and Luuk A M van der Wielen. 2006. "Downstream Processing." *Basic Biotechnology: Third Edition*: 219–50.

Pandithage, Ruwin. 2013. "Brief Introduction to Contrasting for EM Sample Preparation." https://www.leica-microsystems.com/science-lab/brief-introduction-to-contrasting-for-em-sample-preparation/ (September 22, 2019).

Putnam, C. 2013. “Protein Calculator.” *May 13*. http://protcalc.sourceforge.net/ (April 19, 2019).

Rigort, Alexander, and Jürgen M. Plitzko. 2015. “Cryo-Focused-Ion-Beam Applications in Structural Biology.” *Archives of Biochemistry and Biophysics* 581: 122–30. http://dx.doi.org/10.1016/j.abb.2015.02.009.

Schure, Mark R. et al. 2017. “Intraparticle and Interstitial Flow in Wide-Pore Superficially Porous and Fully Porous Particles.” *Chemical Engineering Science* 174: 445–58.

Seidel-Morgenstern, Andreas, Michael Schulte, and Achim Epping. 2013. “Fundamentals and General Terminology.” *Preparative Chromatography: Second Edition*: 7–46.

Staby Arne,Nielsen Jacob, Krarup Janus. 2004. “Advances in Chromatography - Google Books.” *CRC Press*: 1034. https://books.google.com.tr/books?hl=en&lr=&id=H-glMWL0TkEC&oi=fnd&pg=PA193&dq=Staby+A,+Sand+MB,+Hansen+RG,+Jacobsen+JH,+Andersen+LA,+Gerstenberg+M,+Bruus+UK,+Jensen+IH.+J+Chromatogr+A+2004%3B1034:85&ots=Qwufhvt7ud&sig=6sTAK12bY9y4ckGkXYgj14yU1d0&redir_es (April 3, 2019).

Stempak, Jerome G., and Robert T. Ward. 1964. “Brief Notes an Improved Staining Method for Electron Microscopy.” *The Journal of Cell Biology*: 697–701.

Tallarek, Ulrich, Felix C. Leinweber, and Andreas Seidel-Morgenstern. 2002. “Fluid Dynamics in Monolithic Adsorbents: Phenomenological Approach to Equivalent Particle Dimensions.” *Chemical Engineering and Technology* 25(12): 1177–81.

Thompson, J. D., J. S. Brown, and P. W. Carr. 2001. “Dependence of Thermal Mismatch Broadening on Column Diameter in High-Speed Liquid Chromatography at Elevated Temperatures.” *Analytical Chemistry* 73(14): 3340–47.

Tosoh Bioscience. 2014. “Size Exclusion Chromatography.” : 12. https://www.separations.asia.tosohbioscience.com/File Library/TBJS/Lit_EN/Catalog/Medias/Cat1_SEC.pdf (September 14, 2019).

Tosoh Bioscience LLC. 2019. “| Https://Www.Separations.Us.Tosohbioscience.Com.” https://www.separations.us.tosohbioscience.com/Process_Media/id-7037/TOYOPEARL_GigaCap_S-650M (April 27, 2019).

Tosoh Bioscience LLC. 2019. “| Https://Www.Separations.Us.Tosohbioscience.Com.” https://www.separations.us.tosohbioscience.com/Process_Media/id-7037/TOYOPEARL_GigaCap_S-650M (September 14, 2019).

Trilisky, Egor I., Harun Koku, Kirk J. Czymmek, and Abraham M. Lenhoff. 2009. "Relation of Structure to Performance Characteristics of Monolithic and Perfusive Stationary Phases." *Journal of Chromatography A* 1216(36): 6365–76.

Unger, Klaus K., Romas Skudas, and Michael M. Schulte. 2008. "Particle Packed Columns and Monolithic Columns in High-Performance Liquid Chromatography-Comparison and Critical Appraisal." *Journal of Chromatography A* 1184(1–2): 393–415.

van der Veen, Marijn, Martien Cohen Stuart, and Willem Norde. 2007. "Spreading of Proteins and Its Effect on Adsorption and Desorption Kinetics." *Colloids and Surfaces B: Biointerfaces* 54(2): 136–42.

Wagner, Brian M. et al. 2017. "Superficially Porous Particles with 1000 Å Pores for Large Biomolecule High Performance Liquid Chromatography and Polymer Size Exclusion Chromatography." *Journal of Chromatography A* 1489: 75–85. http://dx.doi.org/10.1016/j.chroma.2017.01.082.

Weiß, Joachim. 2016. *Handbook of Ion Chromatography*. 4th ed. Germany: Wiley-VCH. https://books.google.com.tr/books?id=pR-HDAAAQBAJ&lpg=PP1&hl=tr&pg=PR10#v=onepage&q&f=false (January 27, 2019).

Xiong, Qingrong, Todor G. Baychev, and Andrey P. Jivkov. 2016. "Review of Pore Network Modelling of Porous Media: Experimental Characterisations, Network Constructions and Applications to Reactive Transport." *Journal of Contaminant Hydrology* 192: 101–17. http://dx.doi.org/10.1016/j.jconhyd.2016.07.002.

Yao, Yan, Kirk J. Czymmek, Rajesh Pazhianur, and Abraham M. Lenhoff. 2006. "Three-Dimensional Pore Structure of Chromatographic Adsorbents from Electron Tomography." *Langmuir* 22(26): 11148–57.

APPENDICES

A. α-Lactalbumin Wavelength Scan at 0.25 mg/ml, 0.5 mg/ml and 1 mg/ml

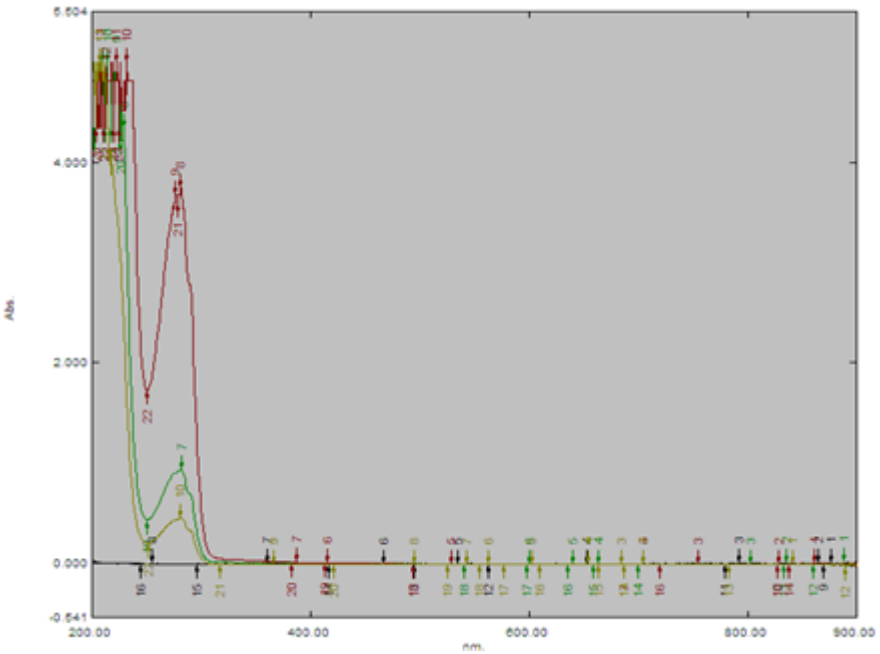

Figure 0.1. Wavelength scan of α-lactalbumin at different concentrations which are 0.25 mg/ml, 0.5 mg/ml and 1 mg/ml

B. Lysozyme Wavelength Scan at 0.25 mg/ml and 0.5 mg/ml

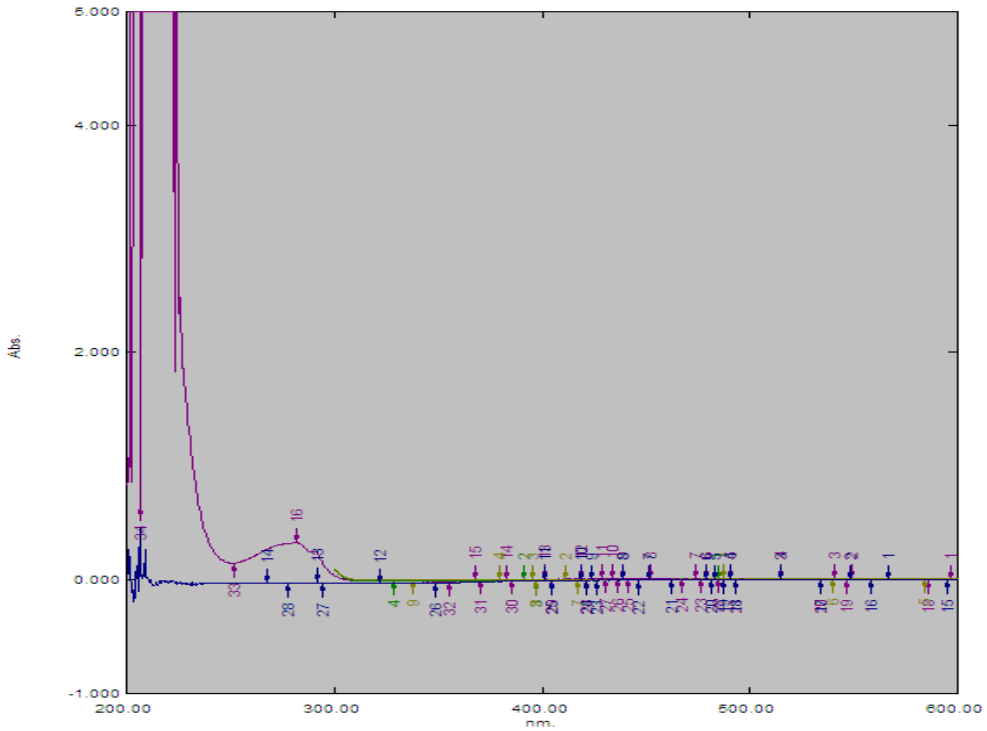

Figure 0.2. Wavelength scan of lysozyme

C. Calibration Curve of Lysosome

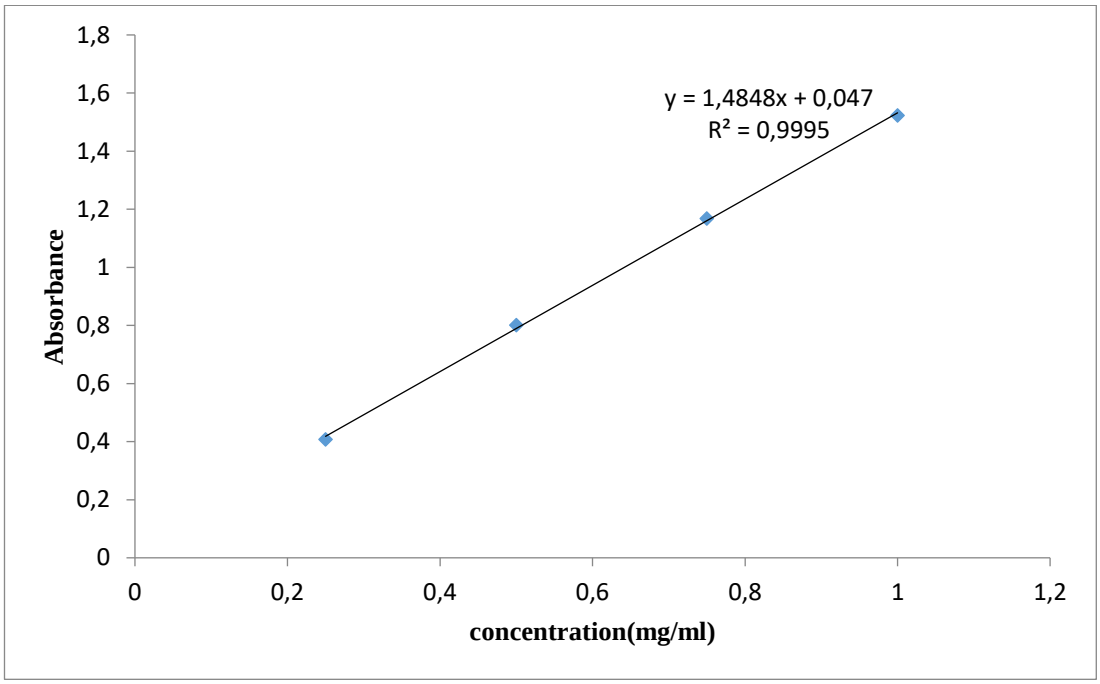

Figure 0.3. Calibration curve of lysozyme

D. Wavelength Scan of Bovine Serum Albumin at 0.05 mg/ml, 0.25 mg/ml, 0.5mg/ml and 0.75 mg/ml

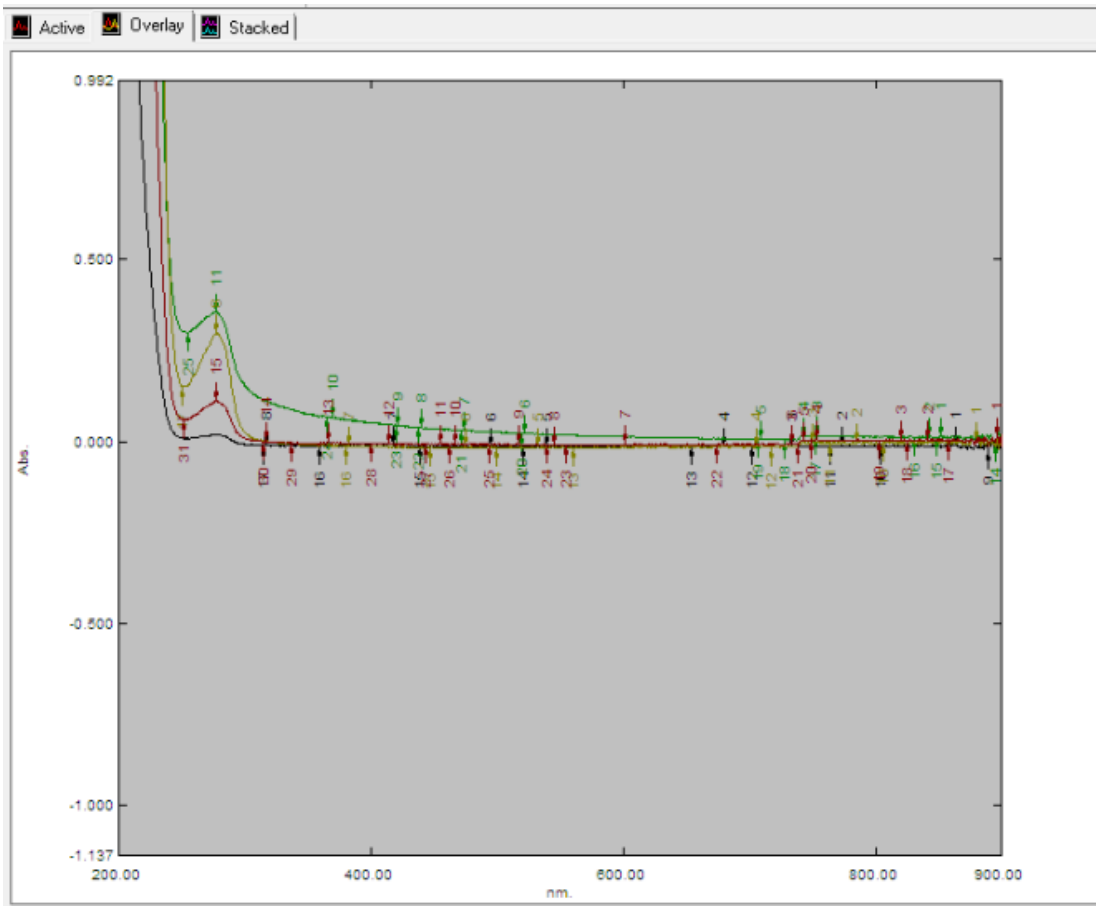

E. Calibration Curve of Bovine Serum Albumin

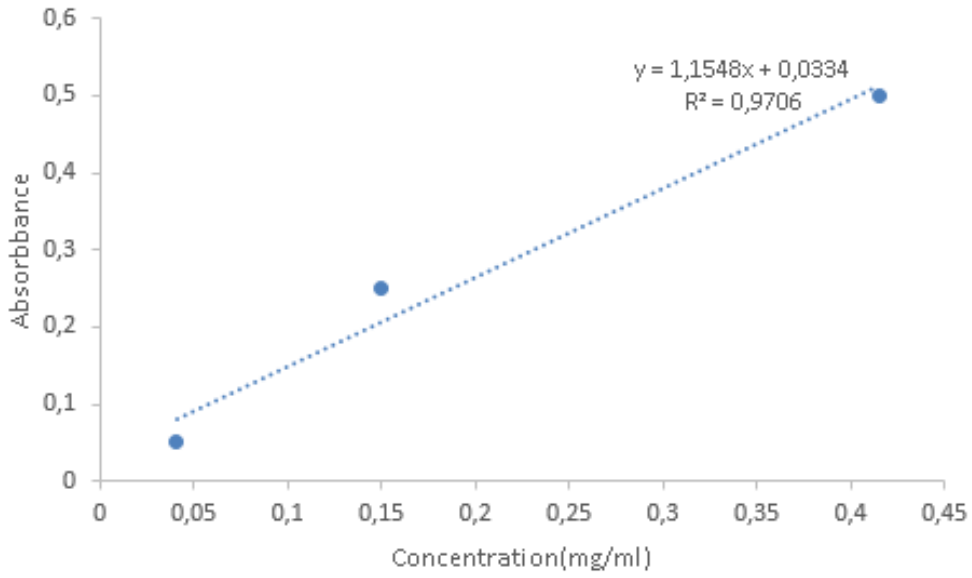

Figure 0.4. Calibration curve of BSA

F. Wavelength Scan of Lysozyme

Wavelength scan of lysozyme	0.25 mg/ml	0.5 mg/ml	1mg/ml
200	3,738	3,437	3,738
201	3,738	3,738	3,738
202	3,738	3,914	3,914
203	3,703	3,914	3,914
204	3,914	3,914	3,914
205	3,864	3,864	3,864
206	3,864	4,215	3,864
207	4,215	3,864	4,215
208	4,215	3,864	3,864
209	4,215	3,864	4,215
210	3,864	4,215	4,215
211	3,864	4,215	4,215
212	3,864	4,215	4,215
213	3,641	3,818	3,818
214	3,641	4,119	4,119
215	3,641	4,119	4,119
216	3,641	4,119	4,119
217	3,517	3,818	3,818
218	3,385	4,119	4,119
219	3,517	3,818	4,119
220	3,385	3,818	4,119
221	3,385	3,818	4,119
222	3,238	4,119	4,119
223	3,174	4,119	3,818
224	3,024	3,914	3,914
225	2,858	3,776	4,119
226	2,678	3,914	4,516
227	2,472	3,67	3,914
228	2,229	3,312	3,914
229	1,973	3,024	3,914
230	1,703	2,687	3,914
231	1,421	2,283	3,517
232	1,172	1,924	3,053
233	0,927	1,576	2,587
234	0,715	1,274	2,16

235	0,536	1,016	1,789
236	0,378	0,792	1,463
237	0,258	0,617	1,202
238	0,156	0,47	0,982
239	0,069	0,342	0,794
240	-0,004	0,236	0,638
241	-0,065	0,148	0,508
242	-0,119	0,069	0,391
243	-0,162	0,007	0,299
244	-0,199	-0,043	0,223
245	-0,228	-0,085	0,159
246	-0,25	-0,119	0,11
247	-0,267	-0,143	0,074
248	-0,279	-0,161	0,047
249	-0,288	-0,173	0,028
250	-0,293	-0,181	0,018
251	-0,294	-0,183	0,014
252	-0,293	-0,181	0,017
253	-0,288	-0,175	0,025
254	-0,283	-0,167	0,037
255	-0,275	-0,154	0,054
256	-0,265	-0,14	0,075
257	-0,253	-0,122	0,102
258	-0,241	-0,103	0,13
259	-0,226	-0,082	0,161
260	-0,212	-0,06	0,192
261	-0,198	-0,041	0,222
262	-0,181	-0,018	0,256
263	-0,164	0,006	0,291
264	-0,148	0,029	0,327
265	-0,131	0,055	0,363
266	-0,114	0,079	0,399
267	-0,098	0,102	0,433
268	-0,08	0,126	0,471
269	-0,065	0,15	0,505
270	-0,052	0,169	0,532
271	-0,04	0,186	0,558
272	-0,029	0,202	0,582
273	-0,019	0,217	0,602

274	-0,012	0,229	0,62
275	-0,007	0,237	0,631
276	-0,004	0,238	0,636
277	-0,002	0,241	0,637
278	0	0,246	0,645
279	0,007	0,254	0,658
280	0,013	0,263	0,671
281	0,016	0,269	0,676
282	0,015	0,266	0,674
283	0,009	0,258	0,663
284	-0,004	0,238	0,631
285	-0,028	0,202	0,58
286	-0,059	0,157	0,511
287	-0,09	0,111	0,445
288	-0,109	0,083	0,401
289	-0,115	0,073	0,392
290	-0,112	0,08	0,396
291	-0,116	0,073	0,387
292	-0,143	0,035	0,33
293	-0,193	-0,037	0,225
294	-0,253	-0,122	0,096
295	-0,304	-0,2	-0,018
296	-0,349	-0,266	-0,116
297	-0,388	-0,322	-0,2
298	-0,418	-0,365	-0,266
299	-0,443	-0,401	-0,316
300	-0,465	-0,431	-0,36
301	-0,481	-0,456	-0,396
302	-0,495	-0,477	-0,427
303	-0,506	-0,492	-0,451
304	-0,516	-0,506	-0,47
305	-0,523	-0,516	-0,487
306	-0,53	-0,526	-0,5
307	-0,533	-0,532	-0,507
308	-0,535	-0,536	-0,513
309	-0,538	-0,539	-0,519
310	-0,539	-0,541	-0,522
311	-0,54	-0,543	-0,525
312	-0,54	-0,544	-0,526

313	-0,542	-0,546	-0,527
314	-0,541	-0,546	-0,528
315	-0,542	-0,545	-0,528
316	-0,543	-0,546	-0,53
317	-0,543	-0,547	-0,531
318	-0,542	-0,547	-0,53
319	-0,543	-0,548	-0,531
320	-0,543	-0,547	-0,531
321	-0,542	-0,547	-0,531
322	-0,542	-0,547	-0,531
323	-0,543	-0,548	-0,531
324	-0,545	-0,547	-0,531
325	-0,545	-0,547	-0,532
326	-0,544	-0,548	-0,533
327	-0,543	-0,548	-0,532
328	-0,545	-0,548	-0,531
329	-0,543	-0,547	-0,531
330	-0,544	-0,548	-0,531
331	-0,544	-0,548	-0,532
332	-0,544	-0,548	-0,532
333	-0,544	-0,548	-0,533
334	-0,544	-0,548	-0,531
335	-0,544	-0,548	-0,532
336	-0,544	-0,548	-0,532
337	-0,544	-0,548	-0,533
338	-0,544	-0,548	-0,533
339	-0,545	-0,548	-0,534
340	-0,544	-0,548	-0,534
341	-0,544	-0,548	-0,534
342	-0,544	-0,549	-0,534
343	-0,545	-0,549	-0,534
344	-0,545	-0,55	-0,535
345	-0,544	-0,549	-0,534
346	-0,544	-0,549	-0,533
347	-0,544	-0,549	-0,536
348	-0,545	-0,549	-0,535
349	-0,544	-0,55	-0,534
350	-0,543	-0,548	-0,533
351	-0,544	-0,549	-0,534

352	-0,545	-0,55	-0,536
353	-0,545	-0,55	-0,535
354	-0,544	-0,549	-0,535
355	-0,544	-0,549	-0,535
356	-0,544	-0,549	-0,534
357	-0,543	-0,549	-0,535
358	-0,542	-0,549	-0,534
359	-0,544	-0,549	-0,535
360	-0,544	-0,551	-0,535
361	-0,544	-0,549	-0,536
362	-0,544	-0,55	-0,534
363	-0,544	-0,548	-0,534
364	-0,544	-0,548	-0,534
365	-0,543	-0,548	-0,535
366	-0,544	-0,548	-0,534
367	-0,544	-0,55	-0,536
368	-0,545	-0,551	-0,536
369	-0,544	-0,55	-0,537
370	-0,544	-0,549	-0,534
371	-0,544	-0,55	-0,535
372	-0,543	-0,55	-0,535
373	-0,543	-0,55	-0,536
374	-0,544	-0,551	-0,536
375	-0,544	-0,551	-0,536
376	-0,543	-0,551	-0,536
377	-0,544	-0,551	-0,536
378	-0,543	-0,55	-0,536
379	-0,544	-0,551	-0,536
380	-0,544	-0,551	-0,537
381	-0,544	-0,551	-0,536
382	-0,544	-0,55	-0,536
383	-0,544	-0,551	-0,536
384	-0,544	-0,551	-0,536
385	-0,544	-0,55	-0,536
386	-0,544	-0,551	-0,535
387	-0,544	-0,551	-0,536
388	-0,544	-0,551	-0,536
389	-0,543	-0,551	-0,536
390	-0,544	-0,55	-0,536

391	-0,544	-0,551	-0,536
392	-0,545	-0,552	-0,537
393	-0,544	-0,551	-0,537
394	-0,544	-0,551	-0,537
395	-0,544	-0,552	-0,538
396	-0,544	-0,551	-0,538
397	-0,544	-0,552	-0,537
398	-0,544	-0,551	-0,537
399	-0,544	-0,551	-0,537
400	-0,544	-0,552	-0,538
401	-0,544	-0,551	-0,537
402	-0,544	-0,551	-0,538
403	-0,544	-0,551	-0,538
404	-0,544	-0,552	-0,538
405	-0,545	-0,552	-0,539
406	-0,545	-0,552	-0,539
407	-0,545	-0,552	-0,539
408	-0,544	-0,551	-0,538
409	-0,544	-0,552	-0,539
410	-0,545	-0,551	-0,539
411	-0,544	-0,552	-0,539
412	-0,544	-0,552	-0,539
413	-0,545	-0,552	-0,539
414	-0,545	-0,552	-0,54
415	-0,544	-0,552	-0,539
416	-0,544	-0,552	-0,54
417	-0,544	-0,553	-0,54
418	-0,544	-0,552	-0,54
419	-0,544	-0,552	-0,539
420	-0,544	-0,552	-0,538
421	-0,545	-0,552	-0,539
422	-0,544	-0,552	-0,539
423	-0,545	-0,552	-0,538
424	-0,544	-0,552	-0,538
425	-0,544	-0,552	-0,538
426	-0,544	-0,552	-0,538
427	-0,544	-0,552	-0,537
428	-0,544	-0,552	-0,537
429	-0,544	-0,552	-0,538

430	-0,544	-0,552	-0,538
431	-0,544	-0,552	-0,537
432	-0,544	-0,552	-0,538
433	-0,544	-0,552	-0,538
434	-0,544	-0,552	-0,538
435	-0,544	-0,552	-0,538
436	-0,545	-0,553	-0,538
437	-0,545	-0,552	-0,538
438	-0,544	-0,552	-0,538
439	-0,544	-0,552	-0,538
440	-0,545	-0,552	-0,538
441	-0,545	-0,553	-0,538
442	-0,544	-0,553	-0,539
443	-0,545	-0,552	-0,539
444	-0,545	-0,553	-0,539
445	-0,545	-0,553	-0,539
446	-0,545	-0,553	-0,539
447	-0,545	-0,553	-0,539
448	-0,545	-0,552	-0,539
449	-0,545	-0,553	-0,539
450	-0,545	-0,553	-0,539
451	-0,545	-0,553	-0,539
452	-0,545	-0,553	-0,539
453	-0,545	-0,553	-0,539
454	-0,545	-0,553	-0,54
455	-0,545	-0,553	-0,539
456	-0,545	-0,553	-0,539
457	-0,545	-0,553	-0,539
458	-0,544	-0,553	-0,539
459	-0,545	-0,553	-0,539
460	-0,545	-0,554	-0,539
461	-0,545	-0,553	-0,539
462	-0,545	-0,553	-0,539
463	-0,545	-0,553	-0,539
464	-0,545	-0,553	-0,539
465	-0,545	-0,553	-0,539
466	-0,544	-0,552	-0,538
467	-0,544	-0,552	-0,538
468	-0,545	-0,552	-0,538

469	-0,544	-0,552	-0,538
470	-0,545	-0,552	-0,538
471	-0,545	-0,552	-0,539
472	-0,545	-0,552	-0,538
473	-0,545	-0,553	-0,539
474	-0,545	-0,552	-0,539
475	-0,545	-0,552	-0,539
476	-0,545	-0,553	-0,54
477	-0,545	-0,553	-0,54
478	-0,544	-0,553	-0,54
479	-0,545	-0,553	-0,54
480	-0,545	-0,553	-0,54
481	-0,545	-0,553	-0,54
482	-0,545	-0,553	-0,54
483	-0,545	-0,552	-0,54
484	-0,545	-0,553	-0,54
485	-0,546	-0,553	-0,541
486	-0,545	-0,553	-0,541
487	-0,545	-0,554	-0,541
488	-0,546	-0,554	-0,541
489	-0,545	-0,553	-0,541
490	-0,545	-0,553	-0,541
491	-0,545	-0,554	-0,541
492	-0,545	-0,553	-0,541
493	-0,545	-0,553	-0,541
494	-0,545	-0,553	-0,541
495	-0,545	-0,554	-0,541
496	-0,545	-0,553	-0,541
497	-0,545	-0,553	-0,541
498	-0,545	-0,554	-0,541
499	-0,544	-0,553	-0,54
500	-0,545	-0,553	-0,54
501	-0,545	-0,554	-0,54
502	-0,545	-0,554	-0,54
503	-0,545	-0,554	-0,541
504	-0,546	-0,553	-0,541
505	-0,545	-0,554	-0,54
506	-0,545	-0,554	-0,54
507	-0,545	-0,553	-0,54

508	-0,545	-0,553	-0,54
509	-0,546	-0,553	-0,541
510	-0,545	-0,553	-0,54
511	-0,545	-0,553	-0,54
512	-0,545	-0,553	-0,54
513	-0,545	-0,553	-0,54
514	-0,545	-0,553	-0,541
515	-0,545	-0,553	-0,541
516	-0,546	-0,553	-0,54
517	-0,545	-0,553	-0,54
518	-0,545	-0,553	-0,54
519	-0,545	-0,553	-0,54
520	-0,545	-0,553	-0,54
521	-0,545	-0,553	-0,54
522	-0,545	-0,553	-0,54
523	-0,545	-0,553	-0,54
524	-0,545	-0,553	-0,54
525	-0,545	-0,553	-0,54
526	-0,545	-0,553	-0,54
527	-0,546	-0,553	-0,541
528	-0,545	-0,554	-0,54
529	-0,545	-0,553	-0,54
530	-0,545	-0,553	-0,54
531	-0,545	-0,554	-0,541
532	-0,545	-0,554	-0,541
533	-0,545	-0,553	-0,541
534	-0,545	-0,553	-0,541
535	-0,545	-0,553	-0,541
536	-0,545	-0,553	-0,541
537	-0,545	-0,554	-0,541
538	-0,545	-0,554	-0,541
539	-0,545	-0,554	-0,541
540	-0,545	-0,554	-0,541
541	-0,545	-0,553	-0,541
542	-0,546	-0,554	-0,542
543	-0,545	-0,554	-0,542
544	-0,545	-0,553	-0,541
545	-0,545	-0,554	-0,541
546	-0,545	-0,553	-0,541

547	-0,545	-0,553	-0,541
548	-0,545	-0,554	-0,541
549	-0,545	-0,554	-0,541
550	-0,545	-0,553	-0,541
551	-0,545	-0,553	-0,541
552	-0,545	-0,553	-0,54
553	-0,545	-0,553	-0,541
554	-0,545	-0,553	-0,541
555	-0,545	-0,553	-0,54
556	-0,545	-0,553	-0,54
557	-0,545	-0,553	-0,54
558	-0,545	-0,553	-0,54
559	-0,546	-0,554	-0,541
560	-0,546	-0,553	-0,54
561	-0,545	-0,553	-0,54
562	-0,545	-0,553	-0,54
563	-0,545	-0,553	-0,54
564	-0,545	-0,553	-0,54
565	-0,545	-0,553	-0,54
566	-0,545	-0,552	-0,539
567	-0,545	-0,552	-0,54
568	-0,545	-0,553	-0,539
569	-0,545	-0,552	-0,539
570	-0,545	-0,553	-0,539
571	-0,545	-0,552	-0,539
572	-0,545	-0,552	-0,539
573	-0,545	-0,552	-0,539
574	-0,545	-0,552	-0,539
575	-0,545	-0,552	-0,539
576	-0,545	-0,552	-0,539
577	-0,545	-0,552	-0,539
578	-0,545	-0,552	-0,539
579	-0,545	-0,553	-0,539
580	-0,545	-0,552	-0,539
581	-0,545	-0,552	-0,539
582	-0,545	-0,552	-0,539
583	-0,545	-0,552	-0,539
584	-0,545	-0,552	-0,539
585	-0,545	-0,552	-0,539

586	-0,545	-0,552	-0,538
587	-0,545	-0,552	-0,538
588	-0,546	-0,551	-0,538
589	-0,545	-0,552	-0,538
590	-0,545	-0,552	-0,538
591	-0,545	-0,552	-0,538
592	-0,545	-0,552	-0,538
593	-0,545	-0,552	-0,538
594	-0,545	-0,552	-0,538
595	-0,545	-0,552	-0,537
596	-0,545	-0,552	-0,538
597	-0,545	-0,552	-0,538
598	-0,545	-0,552	-0,538
599	-0,545	-0,552	-0,538
600	-0,545	-0,551	-0,537
601	-0,545	-0,552	-0,538
602	-0,545	-0,552	-0,538
603	-0,545	-0,552	-0,538
604	-0,545	-0,552	-0,538
605	-0,545	-0,553	-0,538
606	-0,545	-0,552	-0,538
607	-0,545	-0,552	-0,538
608	-0,545	-0,552	-0,538
609	-0,545	-0,552	-0,538
610	-0,545	-0,552	-0,538
611	-0,545	-0,552	-0,538
612	-0,545	-0,552	-0,539
613	-0,545	-0,552	-0,538
614	-0,545	-0,552	-0,539
615	-0,545	-0,552	-0,539
616	-0,545	-0,552	-0,539
617	-0,545	-0,552	-0,539
618	-0,545	-0,551	-0,539
619	-0,545	-0,552	-0,539
620	-0,545	-0,552	-0,539
621	-0,545	-0,552	-0,539
622	-0,545	-0,552	-0,539
623	-0,545	-0,552	-0,54
624	-0,545	-0,552	-0,539

625	-0,545	-0,552	-0,54
626	-0,546	-0,552	-0,539
627	-0,545	-0,551	-0,539
628	-0,545	-0,552	-0,539
629	-0,545	-0,552	-0,539
630	-0,545	-0,552	-0,539
631	-0,545	-0,552	-0,54
632	-0,545	-0,552	-0,54
633	-0,545	-0,551	-0,539
634	-0,545	-0,552	-0,54
635	-0,545	-0,552	-0,539
636	-0,545	-0,552	-0,54
637	-0,545	-0,552	-0,539
638	-0,545	-0,551	-0,539
639	-0,545	-0,551	-0,539
640	-0,545	-0,551	-0,539
641	-0,545	-0,551	-0,539
642	-0,545	-0,551	-0,539
643	-0,545	-0,551	-0,539
644	-0,545	-0,551	-0,539
645	-0,545	-0,551	-0,539
646	-0,545	-0,551	-0,539
647	-0,545	-0,551	-0,539
648	-0,546	-0,551	-0,539
649	-0,545	-0,551	-0,539
650	-0,545	-0,551	-0,539
651	-0,544	-0,55	-0,539
652	-0,545	-0,551	-0,539
653	-0,545	-0,551	-0,539
654	-0,545	-0,551	-0,539
655	-0,545	-0,551	-0,538
656	-0,546	-0,551	-0,539
657	-0,545	-0,551	-0,539
658	-0,545	-0,551	-0,539
659	-0,545	-0,551	-0,538
660	-0,545	-0,551	-0,538
661	-0,545	-0,551	-0,538
662	-0,545	-0,551	-0,538
663	-0,545	-0,551	-0,538

664	-0,546	-0,551	-0,538
665	-0,545	-0,551	-0,538
666	-0,546	-0,551	-0,538
667	-0,545	-0,551	-0,537
668	-0,545	-0,551	-0,537
669	-0,545	-0,551	-0,538
670	-0,545	-0,55	-0,537
671	-0,545	-0,551	-0,537
672	-0,545	-0,551	-0,538
673	-0,545	-0,551	-0,537
674	-0,545	-0,551	-0,537
675	-0,546	-0,55	-0,537
676	-0,546	-0,551	-0,538
677	-0,546	-0,551	-0,538
678	-0,545	-0,551	-0,537
679	-0,545	-0,551	-0,537
680	-0,545	-0,551	-0,538
681	-0,546	-0,551	-0,537
682	-0,545	-0,551	-0,538
683	-0,545	-0,551	-0,538
684	-0,546	-0,551	-0,538
685	-0,545	-0,55	-0,537
686	-0,546	-0,551	-0,537
687	-0,545	-0,55	-0,538
688	-0,545	-0,55	-0,538
689	-0,545	-0,55	-0,539
690	-0,546	-0,55	-0,538
691	-0,546	-0,551	-0,538
692	-0,546	-0,551	-0,538
693	-0,546	-0,55	-0,538
694	-0,546	-0,55	-0,538
695	-0,546	-0,55	-0,538
696	-0,546	-0,55	-0,538
697	-0,546	-0,55	-0,538
698	-0,545	-0,55	-0,538
699	-0,545	-0,55	-0,538
700	-0,545	-0,55	-0,539
701	-0,545	-0,549	-0,538
702	-0,545	-0,55	-0,538

703	-0,545	-0,55	-0,539
704	-0,546	-0,55	-0,538
705	-0,546	-0,549	-0,538
706	-0,545	-0,549	-0,539
707	-0,545	-0,55	-0,538
708	-0,545	-0,549	-0,538
709	-0,545	-0,549	-0,538
710	-0,545	-0,549	-0,538
711	-0,545	-0,549	-0,538
712	-0,546	-0,55	-0,538
713	-0,545	-0,549	-0,538
714	-0,545	-0,549	-0,539
715	-0,545	-0,549	-0,539
716	-0,545	-0,55	-0,539
717	-0,545	-0,549	-0,538
718	-0,545	-0,549	-0,538
719	-0,546	-0,55	-0,538
720	-0,546	-0,55	-0,539
721	-0,545	-0,549	-0,538
722	-0,545	-0,549	-0,537
723	-0,545	-0,549	-0,539
724	-0,546	-0,549	-0,538
725	-0,545	-0,549	-0,539
726	-0,546	-0,55	-0,54
727	-0,545	-0,55	-0,539
728	-0,545	-0,549	-0,538
729	-0,545	-0,549	-0,539
730	-0,545	-0,549	-0,539
731	-0,545	-0,548	-0,539
732	-0,545	-0,549	-0,538
733	-0,544	-0,548	-0,538
734	-0,546	-0,549	-0,539
735	-0,545	-0,55	-0,539
736	-0,546	-0,549	-0,539
737	-0,545	-0,549	-0,539
738	-0,545	-0,549	-0,538
739	-0,545	-0,549	-0,539
740	-0,545	-0,55	-0,538
741	-0,545	-0,55	-0,538

742	-0,545	-0,549	-0,538
743	-0,545	-0,549	-0,539
744	-0,545	-0,549	-0,539
745	-0,546	-0,55	-0,539
746	-0,545	-0,55	-0,539
747	-0,545	-0,551	-0,539
748	-0,546	-0,55	-0,539
749	-0,545	-0,55	-0,539
750	-0,545	-0,55	-0,539

G. Embed 812 Kit Preparation Formula

	Soft(ml)	Medium(ml)	Hard(ml)
Embed 812	20	20	20
DDSA	22	16	9
NMA	5	8	12
DPM-30	0.7-0.94	0.66-0.88	0.62-0.82

H. Focused Ion Beam Instrument

Focused Ion Beam Instrument,Nova Nanolab 600i,Unam,Bilkent

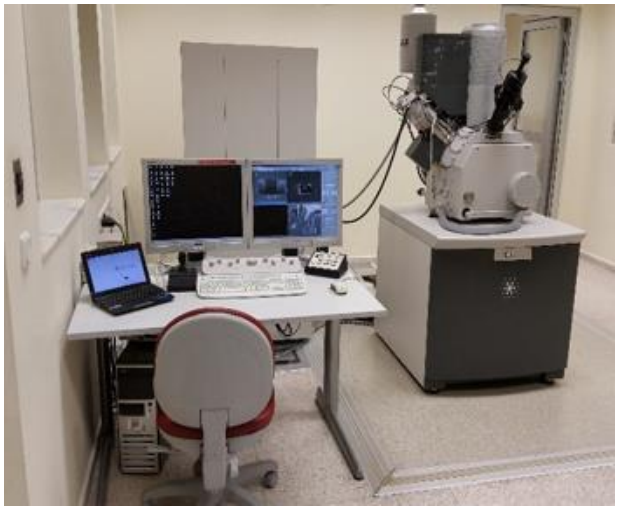

Focused Ion Beam Instrument,Tescan Gaia3 Triglav

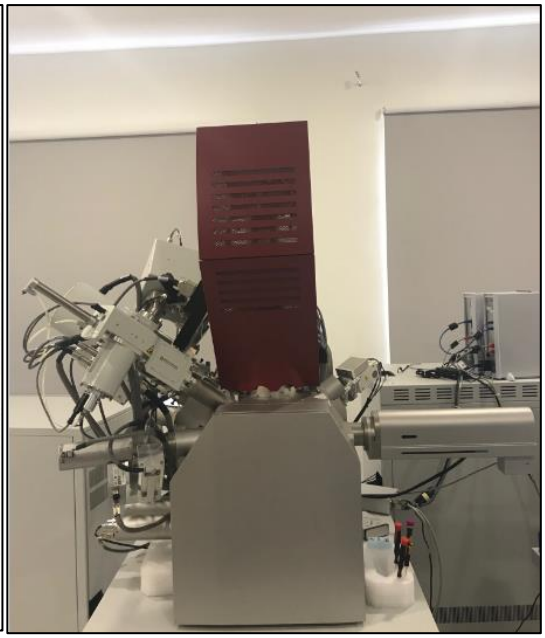

İ. Ultramicrotome Instrument

Leica Ulramicrotome Instrument

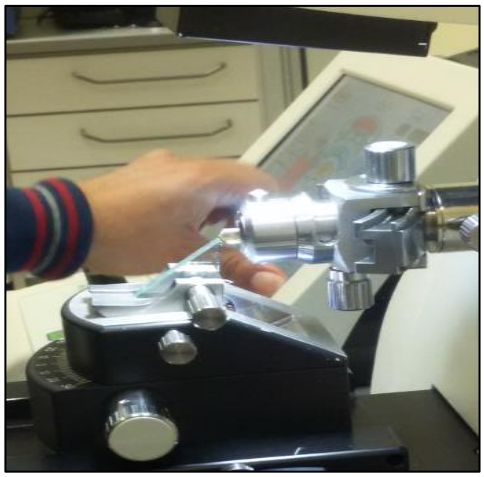

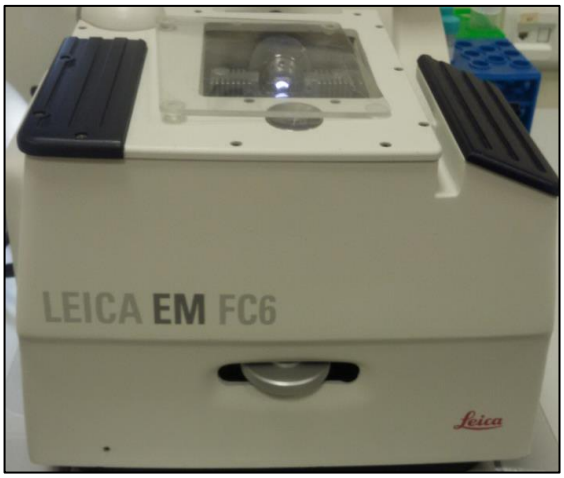

J. Au-Pd Coating Instrument

Conductive Coating Instrument,Gatan Model 682

Plasma Sputter Coater

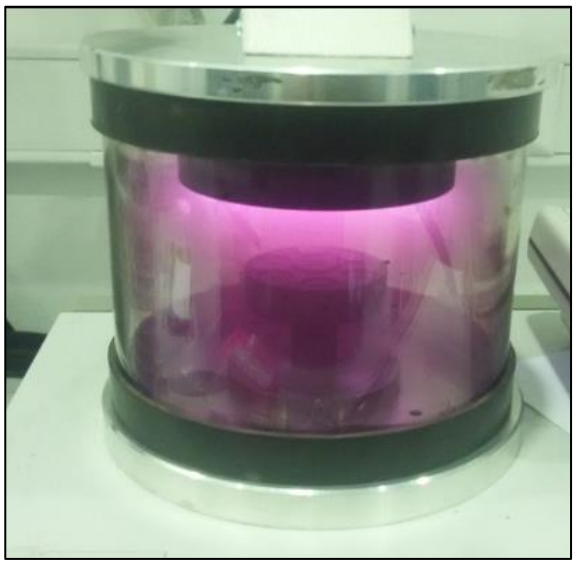

K. Leica Conductive Layer Coating Device

Au-Pd Coating Instrument, Leica EM ACE200

L. Immersion Lens Mode Working Paremeter

First Working Parameter

[MAIN]

AccFrames=1

Date=2019-07-12

Description=

Device=GAIA3 GMU (model 2016)

FullUserName=supervisor

ImageStripSize=90

Magnification=23.164e3

Note=.

PixelSizeX=11.670e-9

PixelSizeY=11.670e-9

SerialNumber=117-0302

Sign=

TagRevision=2

Time=16:45:59

UserName=supervisor

Version=4.2.27.0

[SEM]

3DBeamTiltX=0.0

3DBeamTiltY=0.0

BeamIntensityIndex=4.00

ChamberPressure=10.042e-3

Detector=In-Beam SE

DwellTime=100.000e-6

DynamicFocusAngle1=-35.0

DynamicFocusAngle2=-35.0

DynamicFocusBreakPos=1.00

EmissionCurrent=179.04e-6

Gun=Schottky

GunShiftX=0.0

GunShiftY=0.0

GunTiltX=4.5700

GunTiltY=-9.8700

HV=2.0000e3

IMLCenteringX=-21.660

IMLCenteringY=-15.590

ImageShiftX=-6.3949e-6

ImageShiftY=-52.720e-6

InBeamExtractor=200.00

InBeamScintillator=10.0000e3

LUTGamma=1.0000

LUTMaximum=255

LUTMinimum=0

MixingMode=0

OBJCenteringX=9.0344

OBJCenteringY=42.912

OBJPreCenteringX=2.8200

OBJPreCenteringY=11.190

PredictedBeamCurrent=30.0005098703e-12

PrimaryDetectorGain=60.805

PrimaryDetectorOffset=86.770

ScanMode=UH RESOLUTION

ScanRotation=0.0

ScanSpeed=7

SpecimenCurrent=16.8498168498e-12

SpotSize=4.25692211893e-9

StageRotation=0.0

StageTilt=55.000

StageX=2.3427e-3

StageY=3.8883e-3

StageZ=4.5899e-3

StigmatorX=1.4300

StigmatorY=-70.000e-3

SystemPressure=353.86e-6

TiltCorrection=-35.000

WD=4.9703e-3

Second Working Parameter

[MAIN]

AccFrames=1

Date=2019-07-12

Description=

Device=GAIA3 GMU (model 2016)

FullUserName=supervisor

ImageStripSize=90

Magnification=13.396e3

Note=.

PixelSizeX=20.179e-9

PixelSizeY=20.179e-9

SerialNumber=117-0302

Sign=

TagRevision=2

Time=16:59:57

UserName=supervisor

Version=4.2.27.0

[SEM]

3DBeamTiltX=0.0

3DBeamTiltY=0.0

BeamIntensityIndex=4.00

ChamberPressure=10.042e-3

Detector=In-Beam SE

DwellTime=32.000e-6

DynamicFocusAngle1=-35.0

DynamicFocusAngle2=-35.0

DynamicFocusBreakPos=1.00

EmissionCurrent=179.10e-6

Gun=Schottky

GunShiftX=0.0

GunShiftY=0.0

GunTiltX=4.5700

GunTiltY=-9.8700

HV=2.0000e3

IMLCenteringX=-21.660

IMLCenteringY=-15.590

ImageShiftX=-3.1055e-6

ImageShiftY=-5.0000e-6

InBeamExtractor=200.00

InBeamScintillator=10.0000e3

LUTGamma=1.0000

LUTMaximum=255

LUTMinimum=0

MixingMode=0

OBJCenteringX=-301.75e-3

OBJCenteringY=40.215

OBJPreCenteringX=2.8200

OBJPreCenteringY=11.190

PredictedBeamCurrent=30.0005098703e-12

PrimaryDetectorGain=60.965

PrimaryDetectorOffset=83.500

ScanMode=UH RESOLUTION

ScanRotation=0.0

ScanSpeed=6

SpecimenCurrent=12.4542124542e-12

SpotSize=4.28921865398e-9

StageRotation=0.0

StageTilt=55.000

StageX=2.2778e-3

StageY=3.6105e-3

StageZ=4.7276e-3

StigmatorX=1.4300

StigmatorY=-70.000e-3

SystemPressure=322.51e-6

TiltCorrection=-35.000

WD=5.0395e-3

M. TEM Analyses of HALO Particles

TEM Images of HALO Particles

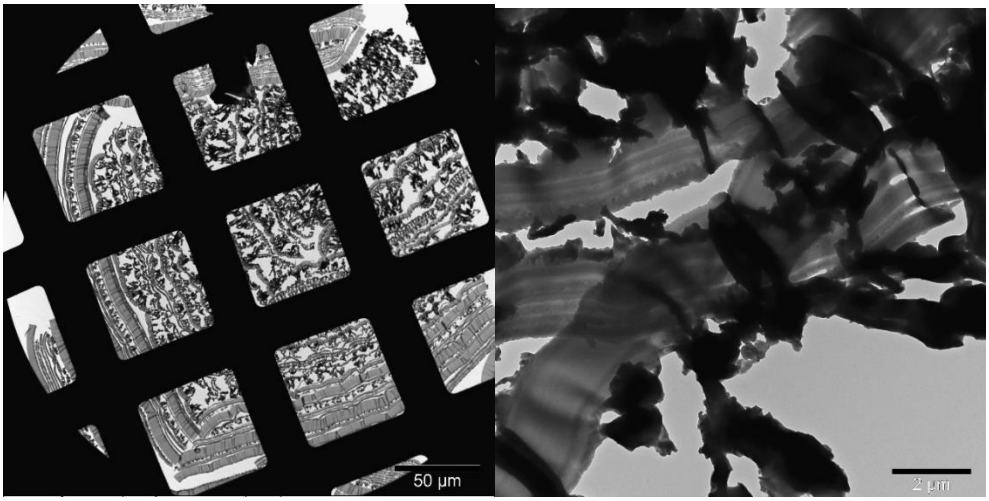

N. Calculation of Protein Concentration

To find the adsorbed amount of BSA, HALO volume (V_{ads}) should be known.

$V_{ads} = V_{solid} + V_{pore}$ (1)

The volume of solid material is shown as V_{solid}, the volume of the pore system is called as V_{pore} in equation 1

From these volumes stated in equation 1, porosities (ε) can be calculated as;

$$\varepsilon = \frac{V_{pore}}{V_{ads}} \quad (2)$$

Generally, for the adsorbents having spherical shape, void fraction(ε) is in the range of $0.26<\varepsilon<0.48$ (Seidel-Morgenstern, Schulte, and Epping 2013). Porosity can be taken as 0.4 (Seidel-Morgenstern, Schulte, and Epping 2013).

Mass of protein: 10mL*(5-3.9) mg/ml=11 mg (3)

Mass of particle: 30 mg=$3*10^{-5}$ kg

Density of HALO (Silica): 2.648 g/cm^3

Particle volume: $\frac{\textbf{mass of particles/density}}{(\mathbf{1-\varepsilon})}$=0.018 mL

Protein Concentration of BSA= (mass of protein/volume particle)= 611 mg/ml

Lastly, α-lactalbumin adsorption amount on the HALO particle was calculated by using the calibration curve of α-lactalbumin.

$C_{i,protein}$=7.93 mg/ml

$C_{f,protein}$=3.78 mg/ml

Mass of protein: 10 ml*(7.93-3.78) mg/ml= 41.5 mg

Mass of particle= 30 mg= $3*10^{-5}$ kg

Particle volume: $\frac{\textbf{mass of particles/density}}{(\mathbf{1-\varepsilon})}$=0.018 mL

Protein Concentration of α-lactalbumin = (mass of protein/volume particle)= 2306 mg/ml